

Magnetically Enhanced Microflow Cytometer for Bead-based Immunoaffinity Measurements in Whole Blood Samples



Scientific thesis for the attainment of the academic degree
Master of Science (M.Sc.)
of the Department of Electrical and Computer Engineering
at the Technical University of Munich.

Supervised by Dr.-Ing. Mathias Reisbeck
Prof. Dr. rer. nat. Oliver Hayden

Submitted by Johann Alexander Brenner
Weisbergerstraße 5a
85053 Ingolstadt
03662733

Submitted on March 30th, 2021 at Munich

Vorwort

Viele Menschen haben mich während meiner akademischen Karriere unterstützt und einen großen Teil zu meinem erfolgreichen Abschluss beigetragen. An dieser Stelle möchte mich bei allen Personen bedanken, die mich auf meinem Weg begleitet haben.

Zuerst möchte ich mich bei Prof. Oliver Hayden bedanken, der in mir - durch seine lebhafte und leidenschaftliche Art - die Faszination für transnationale Biomedizintechnik wecken konnte und an dessen Lehrstuhl ich für jegliche Aktivitäten immer willkommen war.

Mein spezieller Dank gilt meinem Betreuer, Dr. Mathias Reisbeck, der mich seit dem Beginn meines Studiums während Bachelor- und Masterarbeit, verschiedener Praktika und nicht zuletzt bei sämtlichen Nebenprojekten mit großem Engagement unterstützt hat. Danke für die hervorragende wissenschaftliche Betreuung meiner Arbeiten, die vielen Stunden an konstruktiven Diskussionen und eine sehr freundschaftliche Zusammenarbeit. Außerdem möchte ich mich herzlich bei Leopold Daum bedanken, der mir einen Großteil meines heutigen Chemie-Verständnisses beigebracht hat und dessen Sarkasmus-getriebene, gute Laune bei einem Feierabendbier oftmals die Stimmung eines gescheiterten Experiments gehoben hat.

Dem gesamten LBE möchte ich für die sehr angenehme Arbeitsatmosphäre danken: Alfred Michelfelder und Margarete Remm für Rat und Hilfe bei diversen Experimenten, Dr. Rune Barnkob für die ein oder andere Hilfestellung in theoretischer Physik und allen anderen Doktoranden, die stets mit einer helfenden Hand zur Seite standen.

Abschließend möchte ich mich bei meinen Eltern, Geschwistern, meinem Onkel und allen Großeltern von Herzen bedanken, die mir den Erfolg im Studium durch ihre bedingungslose Unterstützung ermöglicht haben und stets mit einem offenen Ohr oder einem guten Rat zur Seite standen.

Contents

List of Abbreviations	0
1 Introduction	1
2 Theory	3
2.1 Microfluidics.....	4
2.1.1 Incompressibility of Fluid Flows	4
2.1.2 Flow and Shear in Microchannels with Viscous Fluids	5
2.1.3 Force Equilibrium of Microbeads	7
2.1.4 Rolling Motion and Surface Interaction of Beads.....	14
2.2 Surface Chemistry	18
2.2.1 Surface Oxidation Methods.....	19
2.2.2 Silane Chemistry	21
2.2.3 Carbodiimide Crosslinker Chemistry	23
2.2.4 The Biotin-Avidin-System	25
2.3 Magneto-resistive Sensing	26
3 Materials and Methods	29
3.1 Magnetic Sensor Device	29
3.1.1 Assembly of Sensor	29
3.1.2 Design and Fabrication of Microfluidics	30
3.1.3 Peripheral Components and Optical Readout.....	33
3.2 Magnetic Beadometry	37
3.2.1 Optical Particle Tracking	37
3.2.2 Absolute Concentration Measurement.....	37
3.2.3 Whole Blood Bead Spiking	38
3.2.4 Bead Capture Assay	38
3.3 Surface Bio-Functionalization	39
3.3.1 Surface Activation.....	39
3.3.2 Chemical Surface Functionalization	41
3.3.3 Surface Bioconjugation	42
3.3.4 Particle Functionalization.....	43

4 Results and Discussion.....	47
4.1 Virtual Prototyping of Cell Signals	47
4.1.1 Numerical investigation of immunomagnetic label density and size on quantitative magneto-resistive sensing of single cells and cell aggregates	47
4.1.2 Single-Cell Signals	49
4.1.3 Cell Aggregates	52
4.2 The MRCyte Simulation Framework	54
4.2.1 Fluid Fields inside the Microchannel	54
4.2.2 Modeling the Force-Equilibrium of a Rolling Bead over a Biofunc- tionalized Surface	56
4.3 Reference Bead Surface Functionalization.....	58
4.3.1 Amine-Surface Biotinylation	58
4.3.2 Carboxylate-Surface Functionalization	60
4.4 Concentration Measurements in MRCyte.....	61
4.4.1 Measurement Error Sources and Calibration of Flow Field.....	63
4.4.2 Concentration Measurement in Diluted Whole Blood.....	66
4.4.3 Differential Counting Setup	67
4.4.4 Surface Magnetization of Biofunctionalized Beads	72
4.5 Surface Modification and Biofunctionalization of the Sensor Chip Substrate	74
4.5.1 Physisorption	74
4.5.2 Evaluation of the Covalent Biofunctionalization with Optical Methods	74
4.6 Affinity-based Concentration Measurements in the Magnetic Flow Cy- tometer.....	77
5 Conclusion	79
6 Outlook.....	83
7 Appendix	85
7.1 Mathematical Notation.....	85
7.1.1 Vectorial and Scalar Units.....	85
7.1.2 Differential Operators	85
7.1.3 Integration and Summation Operators.....	86
7.1.4 Equations and Inequalities.....	86
7.2 Additional Figures	87
List of Figures	102

List of Tables	103
Bibliography	104
Statement	115

List of Abbreviations

Symbols

χ - magnetic susceptibility
η - dynamic viscosity
ω - angular rotation frequency
τ - surface stress tensor
τ_{pressure} - pressure stress tensor
τ_{viscous} - viscous stress tensor
ε - shear stress tensor
Ω - rotation vector
ρ - density
$\sum_i \mathbf{F}_i$ - body forces

A

A - area
AcOH - acetic acid
adj. R^2 - adjusted coefficient of determination
Al_2O_3 - aluminum oxide
amine - $-\text{NH}_2$
APTES - 3-triethoxysilylpropan-1-amine

B

\mathbf{B} - magnetic flux density
--

C

carboxamide - $\text{R}_1-\text{CONH}-\text{R}_2$
carboxyl - $-\text{COOH}$
C_{const} - linear fit correction factor
C_{rr} - rolling resistance factor
CV - coefficient of variance
C_{velocity} - velocity correction factor

D

d_{GMR} - GMR bridge distance
--

diH₂O - deionized water
DMSO - dimethyl sulfoxide

E

EDC - 3-(Ethyliminomethyleneamino)-N,N-dimethylpropan-1-amine ..
EDTA - 2,2',2'',2'''-(ethane-1,2-diyl)dinitrilo)tetraacetic acid.....
ethoxy - —O—CH₂—CH₃.....
EtOH - ethanol

F

F_{buoyancy} - buoyancy ..
F_{drag} - Stoke's drag force ..
F_{el} - Coulomb's force ..
F_{grav} - gravity ..
F_{mag} - magnetic force ..
F_{magnus} - Magnus lift force ..
F_{protein} - protein-bond force ..
*f*_s - sampling frequency ..
F_{saffman} - Saffman lift force ..
F_{shear} - shear-induced lift force ..
FWHM - full width at half maximum ..

G

GMR - giant magneto-resistance ..

H

h - channel height ..
H₂O₂ - hydrogen peroxide ..
H₂SO₄ - sulfuric acid ..
H₂SO₅ - Caro's acid ..
HCl - hydrochloric acid ..
HF - hydrofluoric acid ..
hydroxyl - —OH ..

I

IPA - isopropanol ..

K

K_d - dissociation constant

L

l - channel length

M

M - magnetization

m - magnetic dipole moment

MACS - MACS running buffer

MeOH - methanol

MES - 2-(N-morpholino)ethanesulfonic acid

MEST - MES buffer with Tween 20

methylene - $-\text{CH}_2-$

MFI - median fluorescence intensity

MFLI - multi-frequency lock-in

MNP - magnetic nanoparticle

MR effect - magneto-resistive effect

N

\vec{n} - unit outward normal

N_2 - nitrogen gas

NHS - 1-Hydroxy-2,5-pyrrolidinedione

NSE - Navier-Stokes-Equation

O

O_2 - oxygen gas

P

PAA - poly(acrylic) acid

PBS - phosphate-buffered saline

PBST - PBS with Tween 20

PCB - printed circuit board

PDMS - poly(dimethylsiloxane)

PE - phycoerythrin

PEG - poly(oxyethylene)

p
piranha - a mixture from hydrogen peroxide with sulfuric acid in excess.....

Q

Q - flow rate.....

R

RBC - red blood cell.....

Re - Reynolds number

*Re*_{particle} - particle Reynolds number.....

S

SAM - self-assembled monolayer

SEM - standard error of the mean.....

Si₃N₄ - silicon nitride.....

silanol - Si—OH.....

siloxane - Si—O—Si.....

SNR - signal-to-noise ratio.....

sulfo-NHS - 1-hydroxy-2,5-dioxopyrrolidine-3-sulfonate.....

T

T_{crit} - critical tension.....

U

u - flow field.....

\bar{u} - mean fluid velocity.....

V

*v*_c - bead velocity

V_p - peak voltage.....

V_{pp} - peak-to-peak voltage.....

W

w - channel width.....

Z

z - approach

1. Introduction

Biosensors employ usually optical [1], electrochemical [2], or magnetic [3–5] transducers to detect biomarkers. Optical biosensors have proven high sensitivity.[6] In turn, one of the most sensitive optical biosensors surpassed a detection limit of 1 cfu mL^{-1} *E. coli* with a time to turnaround of 30 min by combining a flow cytometer and fluorescent magnetic nanoparticles (MNPs).[7] However, optical systems rely on the transparency and low optical background of the sample. The consequential pre-analytics require specialized laboratory and expert personnel.

Magnetic flow cytometry targets these shortcomings under the trade-off, that until now lower throughput and less measurable parameters are limiting factors.[3] Especially in optically dense samples, such as human body fluids and blood, magnetic flow cytometry can manifest its superior capabilities because of a negligible magnetic background in the biological samples.[8] On the one side, this enables cheap point-of-care tests since the giant magneto-resistance (GMR) sensor costs less than 20 € in comparison to optical spectrometers or cameras.[9–11] On the other side, the sharp sensitivity and electronic speed of these sensors allow for precise single-cell measurements.[4, 12, 13] When magnetically labeled cells are rolling over such a sensor, information about a cell's size, morphology, and biomarker density can be extracted from a single signal pattern.[14]

In this thesis, the existing magnetic flow cytometry platform has been extended and characterized for the use of affinity-based assays. With the help of a newly established model system for biomarker densities on cell surfaces, their functional interaction in a microchannel has been studied theoretically and experimentally.

First, the physical phenomena of rolling cells with a bio-functionalized surface under laminar flow conditions were simulated from a hydrodynamic and magnetic point of view. Here, the synergy of fluid dynamics, inertia, viscous, and body forces was illuminated in an analytical force equilibrium.(Secs. 2.1.3, 4.2.1, and 4.2.2) Additionally, a numeric magnetic field simulation of MNP-laden spheres was correlated to dipole signals in the magnetic flow cytometer.(Sec. 4.1)

Second, a reference system for the variation of surface receptor density was established and subsequently evaluated. With the developed methods, several proteins were

attached to the surface of microbeads covalently. In the next step, the protocols were adapted to preserve a reliable dose titration of biotin and antibodies for the coating density.(Sec. 4.3)

Third, absolute and differential concentration measurements were benchmarked for the magnetic flow cytometer. For absolute counting experiments, beads were diluted to exact concentrations with buffer or whole blood and quantified in the magnetic setup.(Sec. 4.4) As a result, empirical correction factors, to account for losses in syringe, connectors, and the parabolic flow profile, were determined.(Sec. 4.4.1) To overcome these limitations, a relative counting apparatus has been engineered from two serially connected magnetic sensors. However, the complexity and tentativeness of the differential system require further developments beyond this thesis.(Sec. 4.4.3) Furthermore, the sensitivity of the sensor to weakly magnetized cells was evaluated in a pretest by MNP-coating the previously functionalized microbeads.(Sec. 4.4.4)

Ultimately, an affinity-based concentration assay will be presented which reveals promising results for the magnetic measurement of biomarker concentrations, exosomes, or single-cell surface proteins in the future.(Sec. 4.6) For this purpose, beads were immobilized in a laminar flow according to their respective biomolecular bond strength. To mediate their bonding to the channel bed, the microchannel was modified by physisorption of neutravidin.(Sec. 4.5.1) Notwithstanding, the unspecific biofunctionalization dismantled swiftly. In turn, a covalent surface treatment strategy was researched, adapted to PDMS, Si₃N₄, and glass, and characterized by optical means.(Sec. 4.5.2) With this biologically augmented microchannel, magnetic measurements showed a clear separation from fully- to sparsely-coated beads. Thereover, a dependency on the biotinylation-degree of microbeads has been measured with strong statistical support. Further insights into these effects could lead to a new segment of point-of-care tests and clinical assays with high sensitivities and the potential to accelerate clinical decision times.

2. Theory

The microscopic rolling motion of a bead in the magnetic flow cytometer is a mixture of continuum and classical mechanics. Introducing a biofunctionalization to the microchannel adds further complexity to a conglomerate of inertia, viscous, and body forces. In order to identify the dominant actors and predict experiments qualitatively, an overview of all forces will be given in the theoretical background. The schematic directions of the respective contributors are shown in Fig. 1. For a subsequent equilibrium hypothesis, hydrodynamic phenomena such as the Saffman-, Magnus- or Fåraeus-Lindquist effects are explained. Moreover, buoyancy, and fluid drag as well as the resulting fluid-induced wall- and shear-lift forces are defined. Most importantly, however, are the electro-magnetic and biomolecular bond forces which are considered to be predominant in this system.(Sec. 2.1.3)

Further, to corroborate some developed protocols of this thesis, a bio-chemical background will be motivated and introduced for covalent surface modifications in Sec. 2.2. Special focus lies on wet-chemical surface oxidation, silanization and carbodiimide coupling chemistry. Thereover, the main measurement principle of the utilized magnetic flow cytometer has already been characterized exhaustively by Helou [15], Reisbeck [3], and others.[16, 17] Nevertheless, key components and the measurement readout will be discussed in Sec. 2.3.

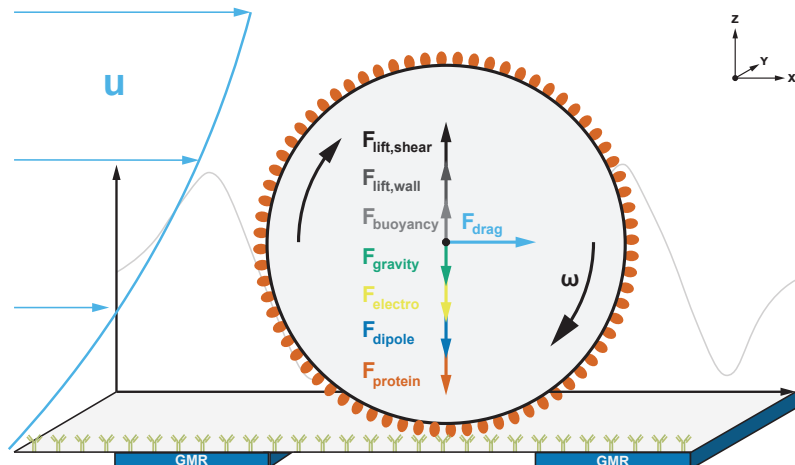


Figure 1: Schematic Force Balance on a Rolling Particle with Bio-Functionalization

The rolling motion of a microbead over the biofunctionalized surface of a microchannel is a mixture of continuum and classical mechanics. In order to identify the dominant actors and predict experiments qualitatively, an overview of all forces will be given in the theoretical background. The during the course of this thesis consistently used coordinate system was defined by e_x along the rolling direction. e_z indicates the height, whereas e_y specifies a width or depth.

2.1. Microfluidics

2.1.1. Incompressibility of Fluid Flows

The main experiments of this work were carried out in microfluidic environments, which exhibit favorable properties compared to common macrofluidic systems. The governing rules of fluid mechanics change with respect to scale. In a microfluidic system interfacial as well as electrokinetic phenomena are predominant and reduce the importance of pressure and gravity.[18] However, electrodynamics, chemistry, and fluid dynamics are inextricably intertwined. In effect, fluid flow can create electric fields (and vice versa), with a degree of coupling driven by the surface chemistry. Many of the resulting phenomena can be deduced from the conservation of mass described by the continuity equation (Eq. 1.1), the conservation of momentum described by the Cauchy-Momentum equation (Eq. 1.4), and the resulting Navier-Stokes equation (Eq. 1.7).¹

$$\frac{\partial}{\partial t} \iiint \rho \, dV = - \iint \rho \mathbf{u} \cdot \vec{n} \, dA \quad 1.1$$

$$\nabla \cdot \mathbf{u} = 0 \quad 1.2$$

$$\frac{\partial}{\partial t} \iiint \rho \mathbf{u} \, dV = - \iint \rho \mathbf{u} \mathbf{u} \cdot \vec{n} \, dA + \iint \boldsymbol{\tau} \cdot \vec{n} \, dA + \iiint \sum_i \mathbf{F}_i \, dV \quad 1.3$$

$$\rho \frac{\partial \mathbf{u}}{\partial t} + \rho \mathbf{u} \cdot \nabla \mathbf{u} = \nabla \cdot \boldsymbol{\tau} + \sum_i \mathbf{F}_i \quad 1.4$$

The foremost assumption in fluid dynamics is termed “incompressibility”. Here, density gradients are negligibly small to assume a uniformity thereof. This leads to a significant simplification of the conservation equations because any transfer from kinetic to internal energy can be ignored.² This continuity equation states that the mass of a control volume - in this case the volume integral over the density (ρ) - can only change by the mass flux over its unit outward normal (\vec{n}) transported by the flow field (\mathbf{u}). For constant ρ the mass does not change over time. This finding and the application of Gauss's theorem (Eq. 1.4) yield the conservation of mass in an incompressible fluid. (Eq. 1.2)

¹ The mathematical prerequisites and notation for all following derivations are explained in Sec. 7.1

² For sake of completeness, it should be mentioned that viscous forces can also transfer energy irreversibly to internal energy. However, they are inversely proportional to the system's size and hence omitted.

2.1.2. Flow and Shear in Microchannels with Viscous Fluids

The above equation and Gauss's theorem can now be applied to the conservation of momentum relation. (Eq. 1.3) Integration then yields the Cauchy momentum equation which states that any change in momentum inside a control volume ($\rho \frac{\partial \mathbf{u}}{\partial t}$) is caused by convective transport from or to the volume ($\rho \mathbf{u} \cdot \nabla \mathbf{u}$), surface stresses ($\nabla \cdot \boldsymbol{\tau}$), and the volumetric net body forces ($\sum_i \mathbf{F}_i$) such as gravity or electrostatics.

Hereby, the surface stress tensor ($\boldsymbol{\tau}$) can be further decomposed into the pressure stress tensor ($\boldsymbol{\tau}_{\text{pressure}}$) and viscous stress tensor ($\boldsymbol{\tau}_{\text{viscous}}$) as shown in Eq. 1.5. Characteristically, the pressure-related contributions act normal and independently from \mathbf{u} whereas viscous forces act normal and tangential, and are dependent on \mathbf{u} . The $\boldsymbol{\tau}_{\text{pressure}}$ can therefore be expressed by a scalar pressure acting in every spatial dimension, which is mathematically represented by the identity.

$$\boldsymbol{\tau} = \boldsymbol{\tau}_{\text{viscous}} + \boldsymbol{\tau}_{\text{pressure}} = 2\eta\boldsymbol{\epsilon} - p\mathbf{I}_{3 \times 3} \quad 1.5$$

$$\nabla \cdot \boldsymbol{\tau}_{\text{viscous}} = \nabla \cdot 2\eta\boldsymbol{\epsilon} = \nabla \cdot \eta \nabla \mathbf{u} \stackrel{\text{only if } \eta \text{ uniform}}{=} \eta \nabla^2 \mathbf{u} \quad 1.6$$

$$\underbrace{\rho \frac{\partial \mathbf{u}}{\partial t}}_{\text{Transient}} + \underbrace{\rho \mathbf{u} \cdot \nabla \mathbf{u}}_{\text{Convection}} = -\nabla p + \underbrace{\eta \nabla^2 \mathbf{u}}_{\text{Pressure}} + \underbrace{\sum_i \mathbf{F}_i}_{\text{Body Forces}} \quad 1.7$$

The viscous stresses however can not be described by a continuum equation, but only by a constitutive relation of atomistic processes. The fundamental model of Newton's mechanics assumes that the dynamic viscosity (η) is neither dependent on any velocity nor strain rate. Therefore, fluids that satisfy this condition are called *Newtonian* fluids. Omitting special *Non-Newtonian* cases such as shear-thinning, -thickening or complex colloidal fluids such as undilute blood, η is the scalar proportionality that relates the strain rate to surface stress.[18] This is captured in the equation $\boldsymbol{\tau}_{\text{viscous}} = 2\eta\boldsymbol{\epsilon}$. Thereby, the shear stress tensor ($\boldsymbol{\epsilon}$) is part of the decomposition of a unidirectional flow field. It resembles, on the one hand, any stretching or squeezing of fluid by *extensional strain* and on the other hand *shear strain* which is responsible for skewing.[18]

The divergence of $\boldsymbol{\tau}_{\text{viscous}}$, as used in the incompressible Cauchy momentum equation (Eq. 1.4), can be further simplified with Eq. 1.6 by taking advantage of the anti-transpose symmetry of the flow field.[18]

If η is also uniform and isotropic across the channel, the scalar viscosity can be extracted from the divergence. Applying all assumptions to the Cauchy momentum equation (Eq. 1.4) yields the Navier-Stokes-Equation (NSE) (Eq. 1.7) as final result.

However, the NSE has no analytic solution yet and can in consequence only be solved for defined boundary problems. The two most common boundary conditions herefore are the “no-penetration condition” ($\mathbf{u} \cdot \vec{n} = 0$) and the “no-slip condition” ($\mathbf{u}_t = \mathbf{u} - (\mathbf{u} \cdot \vec{n})\vec{n} = 0$), which state that the normal and tangential components of fluid velocity are per definition zero at motionless, impermeable walls.

Alongside these conditions, many problems arise due to turbulent flow and therefore transient effects. Mathematically, this can be avoided by simply neglecting the time-dependent term in the NSE. For viscosity-dominated flow it can be argued that fluid moves in isoplanar *lamina*³. In experimental observations, these laminar flows then proved to be steady to perturbations.

$$Re = \frac{\text{fluid density} \times \text{velocity} \times \text{size}}{\text{viscosity}} \quad 1.8$$

In a first-order approximation, the dimensionless Reynolds number (Re), which compares the inertia to viscous forces, allows a qualitative prognosis about the flow regime. (Eq. 1.8) A Re below a threshold of 2300 indicates laminar flow in Hagen-Poiseuille flows. This holds for the utilized microfluidic with the dimensions $15\,800\,\mu\text{m} \times 700\,\mu\text{m} \times 150\,\mu\text{m}$ (channel length (l) \times channel width (w) \times channel height (h)) and aqueous buffer solutions. Typically, where smallest length h or the hydraulic diameter is considered as *characteristic size*, whereas the characteristic velocity is usually employed by either the maximum of \mathbf{u} or mean fluid velocity (\bar{u}). With the smallest length and the mean flow, Re equals 2.1399 for a flow rate (Q) of $80\,\mu\text{L}\,\text{min}^{-1}$ ($h = 150\,\mu\text{m}$), whereas for a Q of $8\,\mu\text{L}\,\text{min}^{-1}$ ($h = 50\,\mu\text{m}$) the Reynolds number already drops to 0.214. Hence, several fluidic phenomena such as deterministic pathlines as well as simplifications of the NSE can be exploited in the present system.

In the model case of a flow inside a rectangular channel, no analytical solution of the NSE exists. A Fourier Series expansion - if the width is larger than the height of a channel - can solve the problem with sufficient precision as shown in Bruus [19]. Equation Eq. 1.9 determines the magnitude of the flow field parallel to the pressure gradient about

³ Latin: lamina = plate, sheet, foil

its horizontal coordinate y and vertical coordinate z with respect to w and h . Integration over the flow field in the channel cross-section yields the Q . (Eq. 1.10)⁴

$$\mathbf{u}_x(y, z) = \frac{4h^2\Delta p}{\pi^3\eta l} \sum_{n,\text{odd}}^{\infty} \frac{1}{n^3} \left(1 - \frac{\cosh(n\pi \frac{y}{h})}{\cosh(n\pi \frac{w}{2h})} \right) \sin(n\pi \frac{z}{h}) \quad 1.9$$

$$Q = \int_{-\frac{1}{2}w}^{\frac{1}{2}w} \int_0^h u_x(y, z) \, dz \, dy \approx \frac{h^3 w \Delta p}{12\eta l} \left(1 - \frac{h}{w} \right), \text{ for } h < w \quad 1.10$$

2.1.3. Force Equilibrium of Microbeads

Although microfluidic systems mostly operate in a low inertia regime as specified by low Re , the force equilibrium $\sum_i \mathbf{F} = 0$, and subsequently the velocity of any particle in the fluid stream is influenced as it moves closer to the boundaries. Several models have already been implemented with a part of the mentioned forces. Lee and Balachandar [20] compared the importance of translation, rotation, and shear forces. Dong and Lei [21] evaluated cell rolling characteristics, and Wu and Voldman [22] proposed a model for bead-based immunoassays in microfluidics. Therefore, an overview over all (inter-)acting forces shall be given here.

$$Re_{\text{particle}} = \frac{r^2}{\frac{2wh}{w+h}} Re \quad 1.11$$

Additionally to the channel Reynolds number Re , describing the ratio between inertial force and viscous force of fluid in a flow, Di Carlo et al. [23] proposed a particle Reynolds number (Re_{particle}) considering the size ratio of particle to channel. At $Re_{\text{particle}} \ll 1$, particles are subjected to the dominant viscous drag to follow fluid streamlines. In the contradictory case, inertia becomes prominent. On increasing Re_{particle} to the order of 1, inertial lift forces become dominant and lateral migration of particles across the streamlines become visible. For a micrometer-sized bead and a channel as referred to in Sec. 2.1.2, the pre-factor is in the range of 1×10^{-5} to 1×10^{-7} hence viscous drag overweighs the inertial lift of a particle.

⁴ The equation Eq. 1.9 shows that height deviations can have a prominent influence on a channel velocity simulation as it is proportional to h^2 . Further, the flow rate depends even on h^3 .

Stoke's Drag Force

The foremost force to actuate particles inside a microfluidic channel is Stoke's drag force (\mathbf{F}_{drag}). (Eq. 1.13) It originates from additional flow resistance caused by a particle in the channel cross-section. The fluid therefore displaces its elements in orthogonal to the movement direction.[24] In the interfacial perspective, viscous fluid is moving past the sphere surface with an axial velocity difference. On the boundaries, a slip condition has to be applied. This is illustrated by a particle with the surrounding streamlines for the bulk case in Fig. 2a, and adjacent walls in Figs. 2b and 2c. In the bulk, due to the no-slip boundary as first-order approximation, drag can be not only expressed by the viscous fluid force $\mathbf{u} \times \eta$ on a circular surface boundary ($2r\pi$) but has to be scaled in low Re regimes by Eq. 1.14 to account for skin friction and form drag.

In the proximity of a channel wall, however, where on one side no fluid can be displaced further, another correction factor was deduced by Happel and Brenner [25], based on works of Faxsén and Oseen, that increases the drag in parallel direction non-linearly.(Eq. 1.15) A phenomenological approximation of the correction factor yields equation Eq. 1.18, when viscosity dominates the difference with an error as shown below.[26, 27]

$$\text{Error} \approx \mathcal{O}\left(\left(\frac{r}{r+z}\right)^7\right) \quad 1.12$$

) Additionally, the viscous drag force causes an induced secondary flow which leads to a perpendicular lift force (Eq. 1.19).[25, 28] This leads to a great influence in pure inertia-dominated or multi-phase flows.[29] Adopted to an example, a spherical air-bubble inside a water flow feels only 67.4 % of the drag by surrounding fluid. The considerations of Stoke's drag force above were limited for linear translation cases. Nevertheless, fluid drag also imposes a non-negligibly torque on particles if a particle moves nearer than 10 diameters to the wall. Happel and Brenner [25] mention an experimentally determined formula in Eq. 1.20 to calculate a drag-related angular rotation frequency (ω). Counter-intuitively, the direction of rotation in the bulk fluid (Fig. 3a) is opposite from the rotation direction near or touching the wall (Fig. 3b). This can be explained by a complex superposition of tangential components from later mentioned forces and will not be explained to any more extent here.[20, 25]

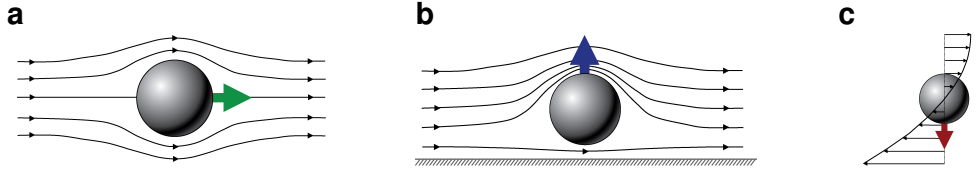


Figure 2: Particle Drag and Lift Behavior

(a) Bulk Drag: Force acts on a particle caused by the displacement of fluid stream lines. (b) Wall-lift Drag Force: In a special case of drag, where streamlines cannot be displaced further, a pressure gradient forms in front of the sphere. This forces a motion directed perpendicularly from the wall. (c) Shear-induced force: The curvature of the flow profile exhibits a translation and rotation due to inhomogeneously distributed shear on the surface.[30]

$$\mathbf{F}_{\text{drag,wall}} = -6\pi\eta r \bar{\mathbf{u}} C \quad 1.13$$

$$C_{\text{drag}} = \frac{24}{Re} (1 + 0.15 Re^{0.687}) \quad 1.14$$

$$C_{\text{drag,exact}} = \frac{4}{3} \sinh \alpha \sum_{n=0}^{\infty} \left(\frac{n(n+1)}{(2n-1)(2n+3)} \cdot A \right) \quad 1.15$$

$$\alpha = \cosh^{-1} \frac{z}{r}, \quad 1.16$$

$$A = \frac{2 \sinh((2n+1)\alpha) + (2n+1) \sinh 2\alpha}{(2 \sinh((n+0.5)\alpha))^2 - ((2n+1) \sinh \alpha)^2} - 1 \quad 1.17$$

$$C_{\text{drag,wall}} = \frac{1}{1 - \frac{9}{16} \frac{r}{r+z} + \frac{1}{8} \left(\frac{r}{r+z} \right)^3 - \frac{45}{256} \left(\frac{r}{r+z} \right)^4 - \frac{1}{16} \left(\frac{r}{r+z} \right)^5} \quad 1.18$$

$$\mathbf{F}_{\text{drag,wall},\perp} = \frac{6\pi\eta r \bar{\mathbf{u}}}{1 - \frac{9}{8} \frac{r}{r+z} + \frac{1}{2} \left(\frac{r}{r+z} \right)^3} \quad 1.19$$

$$\omega = \frac{3\mathbf{u}}{32r} \left(\frac{r}{r+z} \right)^4 \left(1 - \frac{3}{8} \frac{r}{r+z} \right), \text{ for } \left(\frac{r}{r+z} \right)^2 \ll 1 \quad 1.20$$

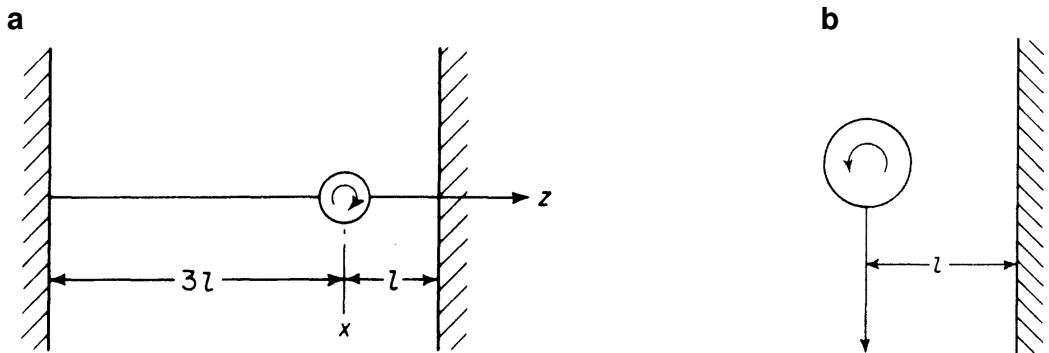


Figure 3: Particle Rotation Behavior

(a) Direction of rotation of a sphere settling in eccentric position between parallel walls. (b) Direction of rotation of a sphere settling in the presence of a single plane wall far from the other side.[23]

Gravity and Buoyancy

On every mass in our environment acts gravity (\mathbf{F}_{grav}) to pull it along its gradient. In a medium, notwithstanding, it is balanced by the displacement of the same in the counter-direction called buoyancy ($\mathbf{F}_{\text{buoyancy}}$). As a microparticle made from a co-polymer - especially when it carries magnetic momentum - has a significantly higher density than water, \mathbf{F}_{grav} (Eq. 1.22) outperforms $\mathbf{F}_{\text{buoyancy}}$ (Eq. 1.21), which in term causes a particle to sink to the channel floor.

$$\mathbf{F}_{\text{buoyancy}} = -\frac{4}{3}\pi r^3 \rho_{\text{fluid}} g \quad 1.21$$

$$\mathbf{F}_{\text{gravity}} = +\frac{4}{3}\pi r^3 \rho_{\text{particle}} g \quad 1.22$$

Magnetic Force

The - during the course of this thesis - strongest acting force is exhibited by the magnetic flux density (\mathbf{B}), which acts on paramagnetic particles with a magnetic dipole moment (\mathbf{m}).[31] When an external magnetic field is non-uniform, there will be a magnetic force (\mathbf{F}_{mag}), proportional to the magnetic field gradient, acting on the \mathbf{m} .(Eq. 1.23) For particles that carry magnetite or similar ferrimagnetic material in their polymer shell, the magnetic momentum can be inferred by the integration of magnetization (\mathbf{M}): $\mathbf{m} = \int \int \int \mathbf{M} dV$. However, the more unified approach is a comparison of magnetic susceptibilities (χ) as described in Eq. 1.23 which involves also diamagnetism and negative magnetophoresis. Consequently, if the particle susceptibility is greater than the fluid's, a microbead will move towards the field maximum. Calculated for an $8 \mu\text{m}$ bead with $1.12 \times 10^{-12} \text{ A m}^2$ saturation magnetization, \mathbf{F}_{mag} results in $\sim 45 \text{ pN}$ for a typical field gradient of 5 T m^{-1} .

$$\mathbf{F}_{\text{mag}} = \frac{V_p (\chi_p - \chi_f)}{\mu_0} (\mathbf{B} \cdot \nabla) \mathbf{B} \quad 1.23$$

$$\mathbf{F}_{\text{dipole}} = (\mathbf{m} \cdot \nabla) \mathbf{B} = -\nabla \mathbf{E}_{\text{dipole}} \quad 1.24$$

$$\mathbf{E}_{\text{dipole}} = \sum_{i=1}^n \frac{\mu_0}{4\pi r_i^3} \left(\mathbf{m}_i \cdot \mathbf{m}_{\text{ref}} - \frac{3}{|\mathbf{r}_i|^2} (\mathbf{r}_i \cdot \mathbf{m}_i) (\mathbf{r}_i \cdot \mathbf{m}_{\text{ref}}) \right) \quad 1.25$$

From a microscopic perspective, magnetic beads interact with each other according to the dipolar interaction. In that case, a reference bead with magnetic momentum \mathbf{m}_{ref} at distance \mathbf{r}_{ref} feels the force of all surrounding particles.(Eq. 1.25) Bringing every dipole in a control volume in superposition leads to the overall magnetic dipole field and can operate as another pathway towards the \mathbf{F}_{mag} calculation.

Electrostatic Interaction

The microchannel - as well as a particle in it - carries an electrical double layer on the surface due to present surface charges. The net charge acquired by the particles can be computed by integrating the particles' surface charge densities over their surfaces as described by Gauss's Law. However, as Coulomb's force (\mathbf{F}_{el}) on charge q_1 is square dependent on the distance from the secondary charge q_2 at the respective locations \mathbf{r}_1 , \mathbf{r}_2 . (Eq. 1.26) This, and the fact that the surface net charge in a buffer solution is insignificant, lead to the assumption that \mathbf{F}_{el} plays a minor role in this force equilibrium.

$$\mathbf{F}_{el} = \frac{q_1 q_2}{4\pi\epsilon_0} \frac{\mathbf{r}_1 - \mathbf{r}_2}{|\mathbf{r}_1 - \mathbf{r}_2|^3} \quad 1.26$$

Saffman Lift Force

When the rotation speed of a particle in the shear rate direction is much greater, $\Omega > 12\nabla\mathbf{u}$, for a freely rotating particle Saffman lift force ($\mathbf{F}_{saffman}$) will begin to act. Depending on the interaction of slip velocity and shear, it will counteract any movement to the planar surface. Hence, at high gradients, the center of rotation causes a shift to the maximum shear.

Scaling with ω , it will generally be at least one order of magnitude larger than Magnus lift force (\mathbf{F}_{magnus}). Especially for electrically or magnetically actuated particles, shear-induced lift force (\mathbf{F}_{shear}) is more relevant in the case of non-neutrally buoyant spheres.[32]

$$\mathbf{F}_{saffman} = \frac{81.2}{4} (\mathbf{u} - u_p) r^2 \sqrt{\frac{\rho_{fluid}}{\eta} \nabla \mathbf{u}} \quad 1.27$$

Shear-induced Lift Force

This force is caused through a curvature in the flow profile and hence an inhomogeneously distributed shear over the sphere cross-section. Following the flow profile, \mathbf{F}_{shear} causes particles to migrate toward walls until the wall lift force repels and balances it. In contrast, if the curvature of \mathbf{u} is zero, it collapses to a simple shear flow. Then, the pressure will increase off-axis and start pushing particles to the centerline. As shown in Fig. 2c the magnitude of \mathbf{u} is much higher on the wall-distant side, due to the parabolic nature of the flow profile.

Similar to $\mathbf{F}_{\text{saffman}}$, the dissymmetry of relative velocity causes a lower pressure on the wall side, generating a shear gradient lift force which is opposite to the Saffman force.[32]

$$\mathbf{F}_{\text{shear}} = K \rho_{\text{fluid}} (\nabla \mathbf{u})^2 r^4, \text{ with } K \text{ from Eq. 1.18} \quad 1.28$$

Magnus Lift Force

The $\mathbf{F}_{\text{magnus}}$ is a rotation-induced variable as a result of the pressure difference induced by streamline asymmetry.[32] For a spinning particle in a fluid as shown in Fig. 4, the streamline density and therefore the pressure on the one side of the particle is lower relative to the other side. The main driver of this effect is again the no-slip boundary, where fluid on the front side of the particle is dragged down whereas the fluid on the bottom side is slowed down. As a result, this leads to a lift force perpendicular to the flow direction.

$$\mathbf{F}_{\text{magnus}} = \frac{1}{8} \pi r^3 \rho_{\text{fluid}} (\mathbf{u} \times \boldsymbol{\Omega}) \quad 1.29$$

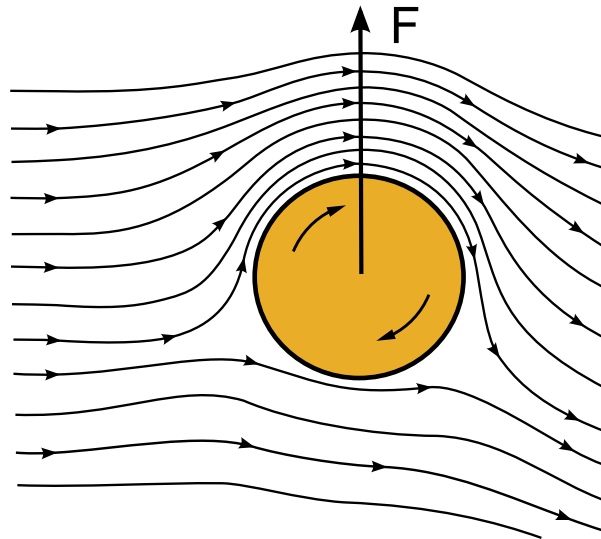


Figure 4: Magnus Effect on a Particle in Laminar Flow

The intrinsic rotation of a particle inside a laminar flow field causes a pressure gradient to the side whose tangential rotation vector is parallel to the stream lines.

Deformability-Induced Lift Force

Although rigidity can be assumed in the first-order to study the hydrodynamic behavior of particles in a microchannel, cells and vesicles are deformable in real experiments. The deformability will induce an additional lift force on the particles which is perpendicular to the main streamline and is subjected to nonlinearities caused by the matching of velocities and stresses at the deformable particle interface.

$$\mathbf{F}_{\text{deformation}} = \mu \mathbf{u} r \left(\frac{r}{h} \right)^2 \frac{r+z}{h} f(\lambda) \quad 1.30$$

$$f(\lambda) = \frac{16\pi}{(\lambda+1)^3} \left[\frac{11\lambda+10}{140} (3\lambda^3 - \lambda + 8) + \frac{3}{14} \frac{19\lambda+16}{3\lambda+2} (2\lambda^2 - \lambda - 1) \right] \quad 1.31$$

For example, deformability-induced lift force has been used already to separate and enrich malaria-infected red blood cell (RBC) from normal healthy RBCs for the diagnosis of malaria. The parasite releases proteins that trigger the cross-linking of the spectrin network of the membrane thus increases the rigidity of the infected cells.[33] Mach and Di Carlo [29] reported a parallelized microfluidic device that passively separates pathogenic bacteria from the diluted blood by the use of unique differential transit times due to channel height differences which in turn cause size-dependent inertial lift forces to obtain cell separation.

Fåræus and Fåræus-Lindquist Effect

Often confused, the Fåræus and Fåræus-Lindquist effect constitute two different hemodynamic properties relevant for microfluidics with blood samples. Whereas the Fåræus effect states that RBCs are depleted in the wall regions of capillaries (due to the lift forces mentioned before), the Fåræus-Lindqvist effect describes the behavior of blood to decrease its viscosity in narrow channels.[34, 35] Thereby, the latter effect is not solely driven by the first, but also the Segré-Silberberg effect, which ascertains that an equilibrium point at exact $0.6r$ from the tubing center forms for neutrally buoyant particles .[36] To model this effect, Chebbi [37] developed a cell-free marginal layer model.

2.1.4. Rolling Motion and Surface Interaction of Beads

Despite the fluid effects on a particle, the contact surface has also a significant influence on the movement of a particle. A fragile force equilibrium is necessary in order to achieve a stable rolling motion.[38] Especially in geology, transient particle transport has been discussed intensely. There, two main termini are conventional: *Contact load*, which identifies particles that move in contact with the bed by sliding or rolling over it, and *saltation load*, which designates the movement as a series of “hops” along the bed, each hop following a ballistic trajectory. To elaborate this further, if a particle remains immobile to the flow and the velocity gradient is large enough so that the lift force exceeds the particle’s adhesive forces, it will jump in a steep trajectory from the channel bottom. Once off, the pressure difference from top to bottom of the particle is lost. Subsequently, it is carried downstream as it falls back to the bed following a ballistic trajectory of saltation.

Contact Area of a Sphere and Flat Surface

Once the acting forces brought the bead in contact with a wall or the channel bottom, it starts to move forward in a rolling motion. In a simple model, rolling on a plane without slipping is constrained by a sphere’s translation (F_{\parallel} , F_{\perp}), rotation (ω), and shear. Nevertheless, due to the rigid nature of the sphere, any shear will be omitted in further models.[39] The no-slip boundary condition has to be applied also here by the requirement that the points of the sphere momentarily in contact with the plane are at rest. However, rolling contact problems are dynamic because the contacting bodies are continuously moving relatively to each other. The contact patch in a sliding problem continuously consists of the same particles. In contrast, particles enter and leave the contact area during rolling. Moreover, in a sliding problem, the surface particles in the contact patch are all subjected to the same tangential shift everywhere, whereas in a rolling problem the surface particles are stressed in different ways. During rolling, they are free of stress when entering the contact, then stick to a particle of the opposing surface, and are strained by the overall motion difference between the two bodies, until the local traction bound is exceeded and local slip sets in.[40]

In reality, pressing two bodies with rough surfaces against each other limits the contact between the two bodies to a value, which is much smaller than the nominal contact area. Additionally, on natural and engineering surfaces Lennard-Jones potential, wetting, and molecular interactions start to play a role on the spectated microscale.[41]

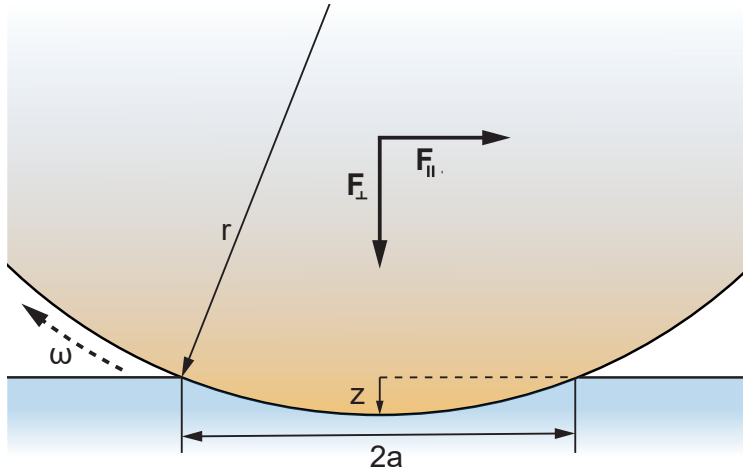


Figure 5: Rolling Mechanics of a Sphere

Penetration model of a sphere with radius r adapted from Azad and Featherstone [41] and Waters and Guduru [42]. The top body moves into the elastic bottom body for an approach (z) and a contact area πa^2 .

In reality, with elastic effects taken into consideration, a different situation occurs. If an elastic sphere is pressed onto an elastic plane (ideally of the same material), both bodies deform and a Hertzian pressure distribution arises. The center of the sphere is moved down by an approach (z) as shown in Fig. 5 that can also be described as “maximum penetration distance”. It can now be calculated that the normal contact area between the bodies follows $A_{contact} = \pi a^2 = \pi (2rz - z^2) = 2\pi rz (1 - \frac{z}{2r})$. Assuming that $z \ll 2r$ and considering that $A_{contact}$ must be zero for all $z < 0$, the following equation for the contact area arises. (Eq. 1.32) The spherical contact surface can be calculated analogous Eq. 1.33.[41]

$$A_{contact} = 2\pi rz, \text{ for } z \geq 0 \quad 1.32$$

$$S_{contact} = \pi r(2z + a^2) = \pi z(4r - z), \text{ for } z \geq 0 \quad 1.33$$

For an 8 μm microbead and a penetration depth z of 100 nm this yields for example interaction with 6.84 % of the total sphere and a total area of 13.753 μm^2 . Several methods and experiments have already been developed in the literature to measure the resulting friction and penetration parameters. A general model of a sphere in contact with a wall was optimized by Krishnan and Leighton [43]. Experimentally, Waters and Guduru [42] developed a micro-tribometer in poly(dimethylsiloxane) (PDMS) to evaluate adhesion properties and validate their model’s predictions.

Protein interaction during Rolling

In the attempt to mimic rolling adhesion on vascular surfaces which is the first step in recruiting circulating leukocytes and other cells into the tissue, protein-protein-interactions as a driver for microbead motions have been studied extensively in this thesis. Statistically, a cell flowing near the vessel wall can attach if its adhesion receptors contact ligands on the wall. A bond formation, anyhow, involves distinct steps: transport, which brings two molecules into proximity, and reaction, during which the molecules dock. Faster cell velocity produces more collisions but also limits the interaction time between molecules. Thus, the relative timescales for transport and docking affect the efficiency of tethering a flowing cell to the surface.[44, 45]

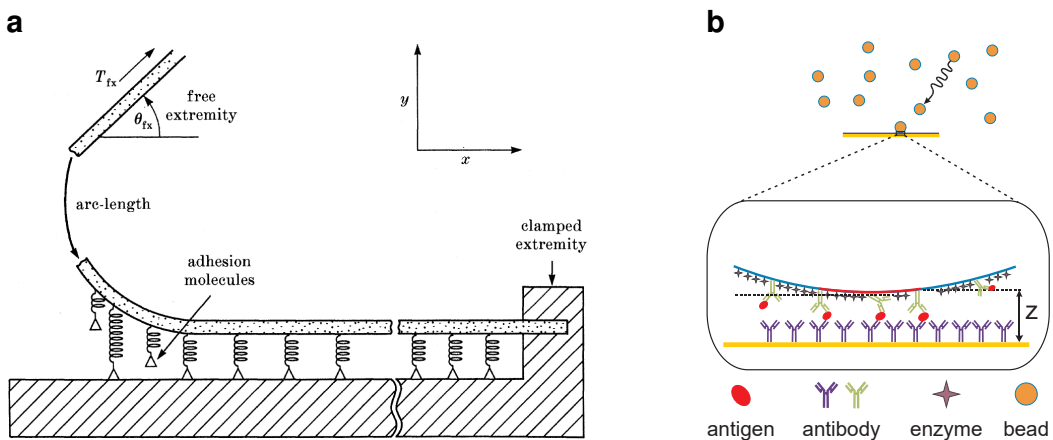


Figure 6: Membrane Adhesion and Detachment Models

(a) Adhesion Model after Dembo et al. [46]: Every interaction is viewed as spring-damper-model in superposition. (b) Surface Coverage Assay Model: In a stochastic approach, analyte molecules and their interactions are modeled between a planar and a spherical surface. Adapted from Wu and Voldman [22]

For these properties, Dembo et al. [46] developed a detailed physical description of membrane adhesion and detachment kinetics. Wu and Voldman [22] then proposed an integrated model for bead-based rolling mechanisms under the influence of protein actions. The key for interaction thereby is the specific *affinity* respectively *avidity* of the protein and its ligand. In general, high-affinity ligand binding stems from greater attractive ligand-receptor-forces and results in a higher tenancy of the receptor. However, the lifetime of a formed complex does not correlate. The net ligand affinities are utilized by the dissociation constant (K_d), which relates the reverse reaction rate ("the dissociation of the bond") to the forward reaction rate ("the formation of the bond"). Therefore, high-affinity results in low K_d .

On a bead and microchannel surface, however, not only one but multiple protein-ligand complexes are formed and dissociated simultaneously. This is described by *avidity*. Though single binding events elevate the likelihood of other interactions, avidity is not relating the sum of its ingredient affinities but can rather be seen as the combined effect of all affinities participating in the biomolecular interaction.[47]

The main factor for the method in this thesis is now the critical tension (T_{crit}). A particle - cell or bead - flowing in a low-Reynolds number environment, experiences a $\mathbf{F}_{\text{shear}}$ and a torque rotation vector (Ω), which both reach their respective maximum when the particle stops. For this, the two forces must be counteracted by a tensile force on the adhesive bonds and a compressive force at the bottom of the particle. Moreover, these forces affect the forward and reverse reaction rates of the bonds. Any rolling motion stops when the adhesion can withstand the force required to counteract the maximal other forces. After the break-up of these bonds, the particle begins to accelerate downstream until a newly formed bond develops sufficient strength. Consequently, the intrinsic mechanics of these bonds and how their respective off-rates act under force critically determines whether and how a bead rolls in a flow field.[44]

There exist two distinct bond types that take effect during the above processes: *Slip bonds* are linkages whose lifetime is shortened to some extent by external force whereas *catch bonds* lock more tightly upon deformation stress.

In biological systems, for example selectines, another effect arises. Upon increasing external stress, bond lifetimes with the ligand are first prolonged until a threshold where bonds are starting to untether. In contrast, if an antibody is the corresponding ligand only slip bonds are formed in response to force.[48, 49] By studying the exact forces acting on a particle-protein interaction system, affinity-based sorting and ultrasensitive assays can be established.[31]

2.2. Surface Chemistry

Introducing biological samples, such as peripheral whole blood and -plasma, into microsystems needs careful consideration of surface modification compared to buffered samples of adjusted pH containing cells or polymeric beads. Blood-material contact most often initiates surface-mediated reactions that lead to cell activation, blood clotting, or biofilm formation.[50, 51] In order to minimize unspecific interactions on surfaces, most contact faces are passivated with chemically and biologically inert materials or even composed entirely from them. In any use case, where a surface has to be functionalized with biomolecules, the intrinsic inertness then requires specialized methods for permanent and reproducible adhesion.[52, 53]

Molecules can be immobilized through various mechanisms on surfaces to achieve a biological or chemical functionality. The most simple is physisorption. Here, a biomolecule is bonded only by weak electrostatic, van-der-Waals, or dipole-dipole interaction with an adsorption enthalpy below 50 kJ mol^{-1} .[53] In contrast, this yields fast reaction rates, because no activation energy has to be overcome. Although a large number of molecules can be captured with this method, several drawbacks have been identified.[54–57]

Therefore, most functionalization approaches rely on chemisorption where molecules are covalently bound to a surface. Due to the higher activation energy barrier this bonding mechanism works slower in comparison to physisorption, though higher temperatures or catalysts can promote an equilibrium. One of the most well-known strategies to bring reproducible thin films on surfaces is the formation of self-assembled monolayers (SAMs) where a dense layer of single molecules with high internal order forms upon dipping into a surface-active substance.[58]

2.2.1. Surface Oxidation Methods

Modifying a surface with functional silanes, requires oxidized sites, for example, $-\text{OH}$ (hydroxyl) resp. $\text{Si}-\text{OH}$ (silanol) groups. In favor of increasing the presence of those reactive groups on substrates, various activation methods such as a mixture from hydrogen peroxide with sulfuric acid in excess (piranha) and sulfuric acid (H_2SO_4), oxygen gas (O_2) - plasma treatment or an hydrofluoric acid (HF) dip can be chosen.[59]

Critical for any surface engineering is the internal structure and in consequence the binding energies of the surficial groups. The three mainly used substrates in this work, glass, PDMS, and silicon nitride (Si_3N_4), contain highly conserved, homogeneous surfaces and are mostly well characterized.[60–62] The surface of glass exhibits already silanol groups intrinsically and consequentially demands only removal of impurities. PDMS and Si_3N_4 , however, have different compositions as shown in Fig. 7c and Fig. 8b hence requiring strong oxidation agents to completely exchange its interface to hydroxyl.[63–65]

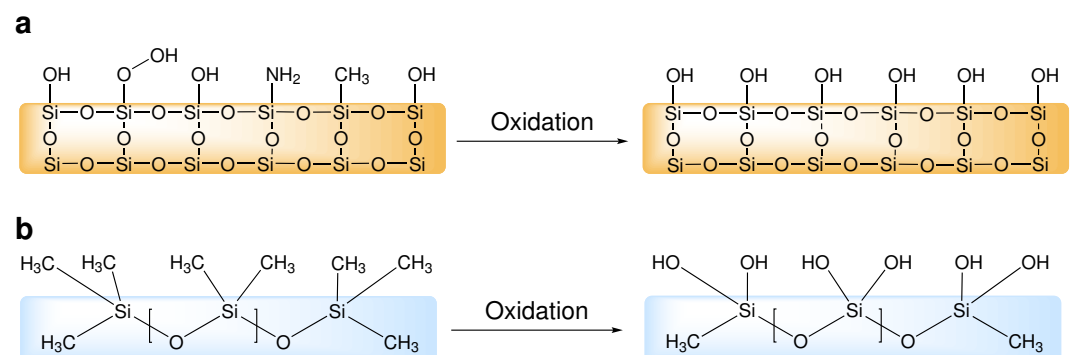
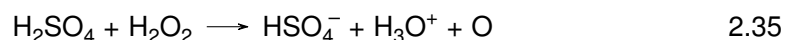
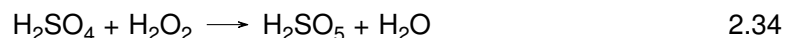


Figure 7: Different Substrate Surfaces: Glass and PDMS

Surface groups and internal structure of quartz glass (a) and PDMS (b). After an oxidation step, surface impurities and the methyl groups are converted to hydroxyl.

Piranha Solution

Piranha is an oxidizer composed of hydrogen peroxide (H_2O_2) and H_2SO_4 , typically in volume ratios between 1:3 and 1:7. The effectiveness of piranha in removing organic residues and creating hydroxyl groups is induced by two distinct processes.



First, hydrogen and oxygen are removed as units of water by the concentrated H₂SO₄ in a comparably fast process.(Eq. 2.34) This occurs due to the thermodynamically favorable reaction with an enthalpy of -880 kJ mol^{-1} and produces Caro's acid (H₂SO₅), one of the strongest oxidants known.[66] Second, the sulfuric acid boosts hydrogen peroxide from a mild oxidizer into the more aggressive atomic oxygen by the dehydration of H₂O₂.(Eq. 2.35) These two dehydrating processes result on the one hand in a highly corrosive nature against organic materials, particularly against the difficult to remove carbon. On the other hand, it is strongly acidic and oxidizing.

Hydrofluoric Acid

One of the substrates used in this work, Si₃N₄, acts as a passivation layer above magnetic sensors as has a significantly better diffusion barrier against water or sodium ions, and is chemically inert.[67] However, due to its complex crystal structure it is also difficult to modify by common chemicals and the exact surface composition still subject to scientific discussion.[68] Apart from cleaning the surface with piranha, few other modification methods have been reported, but only one suitable for the direct generation of hydroxyl groups.[58, 68–70]

As depicted in Fig. 7, the reaction Si—OH + HF \leftrightarrow Si—F + H₂O takes place reversibly due to the coincidence that Si—O and O—H, as well as Si—F and H—F bonds, have similar binding energies. Hence, the forward and reverse reactions require a low activation energy. After Le Chatelier's principle, a depletion of HF in the bulk leads then to an increase in surficial hydroxyl groups.[71] It was revealed that oxidation with a similar protocol based on aqueous HF yields a variable Si—O—Si (siloxane) coverage with $37 \pm 17\%$ of a monolayer, which can be used for stable, covalent attachment of silanes. Nominally, the same surface coverages of silicon oxide and nitride surfaces could be achieved by ethoxy- and chloro-silanization.[72] As shown by Gustavsson et al. [73], the subsequent surfaces exhibit beneficial biological properties and can be modified by further standard procedures.

Oxygen Plasma

Apart from wet chemistry methods, the exposure of a surface to oxygen plasma yields hydroxyl groups as well. In a plasma chamber, low-pressure gas is irradiated by kHz to MHz waves to excite and ionize its atoms. In consequence, the UV radiation emitted by the gas can photolyze typical organic bonds and remove surface contaminations. Additionally, reactive oxygen species such as O_2^+ , O_2^- , O_3 or O oxidize the surface or bind dissociated components with low vapor pressure. During an evacuation in the process, these molecules are removed from the chamber intrinsically.[74]

2.2.2. Silane Chemistry

By the use of silane chemistry, a surface is rendered organofunctional with alkoxy silane molecules. Since glass, silicon, alumina, titania, and quartz surfaces, as well as other metal-oxide interfaces, are rich in hydroxyl groups, silanes are particularly useful for modifying these materials.[75]

The general formula for a silane coupling agent (Fig. 8a) typically shows the two classes of functionality. X is a hydrolyzable group typically alkoxy, acyloxy, halogen, or amine. Following hydrolysis, a reactive silanol group is formed, which can condense with other silanol groups to form siloxane linkages. (Fig. 8) Stable condensation products are also formed with other oxides such as those of aluminum, zirconium, tin, titanium, and nickel. Less stable bonds are formed with oxides of boron, iron, and carbon, whereas alkali metal oxides and carbonates do not form stable bonds with siloxanes at all. The R group (Fig. 8a) is a nonhydrolyzable organic radical that may possess a functionality that imparts desired characteristics. One of the more common silanes is 3-triethoxysilyl-propan-1-amine (APTES), where the X group consists of an $-O-CH_2-CH_3$ (ethoxy) group, the organic rest R is substituted by an $-NH_2$ (amine) and the 3 $-CH_2-$ (methylene) groups alter n to 3.[76]

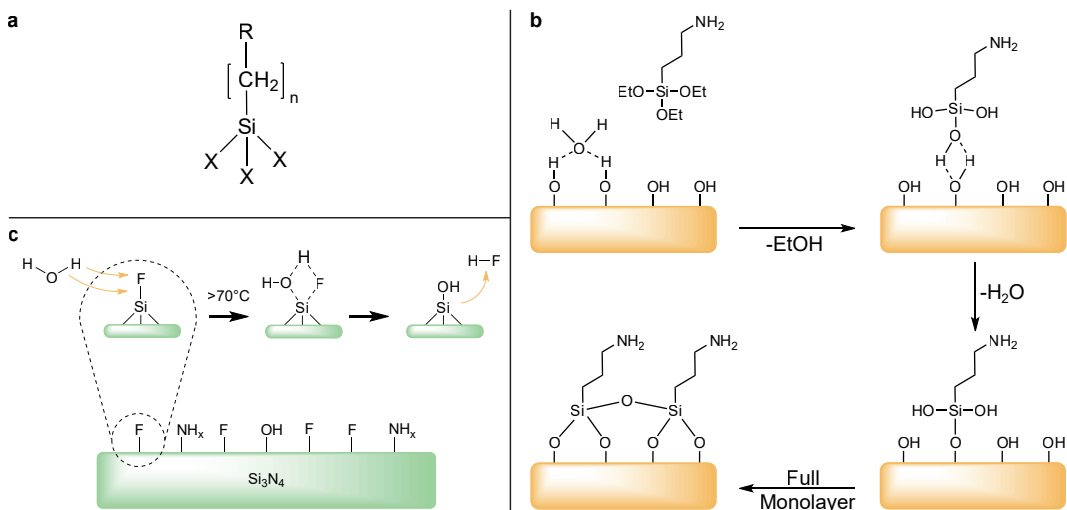


Figure 8: Surface Oxidation and Modification by APTES

(a) Structure of a typical trialkoxysilane, X: hydrolyzable group, R: non-hydrolyzable organic radical, n: methylene chain-length. (b) Before a condensation reaction, the oxidized surface has formed hydrogen bonds with water molecules while the silane molecules are in the bulk solution. The hydrolyzed silanol group adsorbs onto the surface and forms hydrogen bridges with the silicon-bound oxygen atom. In a condensation reaction, under the loss of water, a covalent bond to the surface forms. After the SAM assembly, the surface is saturated with a covalent-bound, crosslinked silane film.[77] (c) Proposed oxidation of Si_3N_4 with HF: Due to similar activation energies water can competitively displace HF above an effective temperature of 70°C .

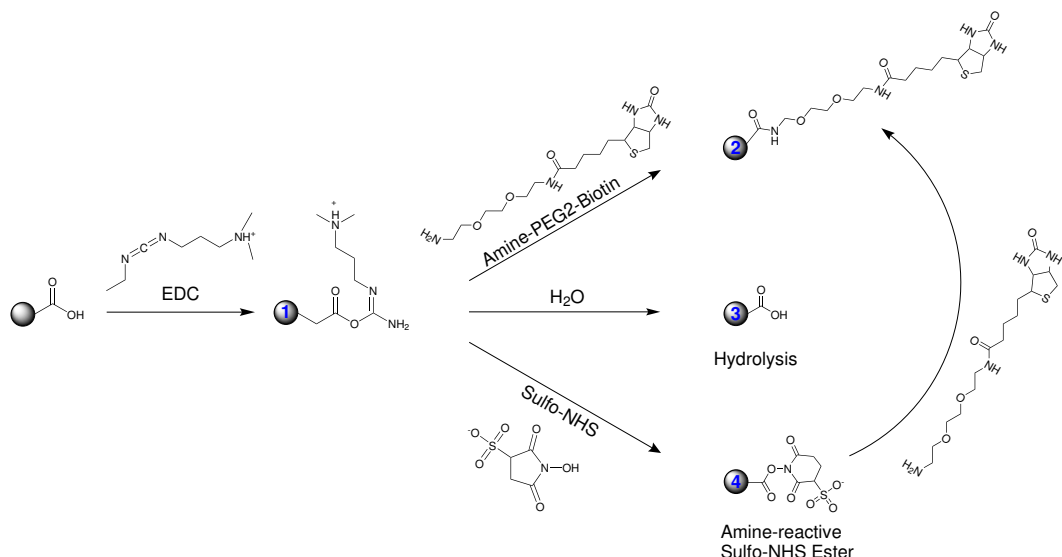


Figure 9: Carboxyl bead modification with EDC/NHS

The carboxyl groups on the bead bead are activated with 3-(Ethyleniminoethyleneamino)-N,N-dimethylpropan-1-amine (EDC) to an active O-acylisourea intermediate. This can then either be nucleophilic attacked by a primary amine of the amine-PEG₂-biotin reactant or - due to its instability - hydrolyzed back to a regenerated carboxyl surface. A present NHS-ester can also displace the O-acylisourea to form a considerably more stable intermediate which then itself reacts with any primary amine.

The applications of organosilane modifications range from altering the adhesion characteristics and catalyzing chemical transformation at the heterogeneous interface towards ordering the interfacial region, and modifying its partition characteristics.[52, 78, 79] Significantly, it includes the ability to effect a covalent bond between organic and inorganic materials. Especially in optical or biological sensors, silane modifications open a broad range of applications.[58, 79, 80]

However, the silanization reactions bear a few drawbacks which are often neglected. For instance, silane chemistry is strongly temperature and pH-dependent.[81, 82] Further, in a process to build SAMs from APTES, the reaction must be catalyzed by water. But already small changes in the water content cause dramatic deviations in layer thickness.[61] Additionally, silanes can crosslink to themselves through side reactions. (Fig. 8b) [83]

2.2.3. Carbodiimide Crosslinker Chemistry

By APTES amine-terminated films form the basis of many reactions and open the possibility to various applications, such as the direct attachment of biofunctional molecules by carbodiimide crosslinking chemistry.[1] Here, $-COOH$ (carboxyl) groups are modified by EDC, and 1-Hydroxy-2,5-pyrrolidinedione (NHS) to form a stable secondary $R_1-CONH-R_2$ (carboxamide) bond with any primary amine.

The general reaction mechanism is depicted in Fig. 9 for the example of a particle surface, but it can equivalently be applied to any other modified surface or molecule. The initial carboxyl group is esterified by EDC to an active o-acylisourea intermediate and leaves rapidly upon nucleophilic attack of an amine with the release of an iso-urea byproduct. A zero-length amide linkage is formed. (Fig. 9, 1->2) Sulfhydryl and hydroxyl groups also will react with such active esters, but the products of such reactions, thioesters and esters, are relatively unstable compared to an carboxamide bond. (Fig. 9, 1)[1]

However, this reactive complex is slow to react with amines and can hydrolyze in aqueous solutions. If the target amine does not find the active carboxyl before it hydrolyzes (Fig. 9, 3), the desired coupling cannot occur. This is especially a problem when the target molecule is in low concentration compared to water, as in the case of protein molecules. Notwithstanding, forming an NHS ester intermediate from the reaction of the hydroxyl group on NHS with the EDC active-ester complex increases the resultant amide bond formation remarkably. (Fig. 9, 4->2) [84]

Another critical point in carbodiimide chemistry is the solubility of the compounds. EDC, NHS and 1-hydroxy-2,5-dioxopyrrolidine-3-sulfonate (sulfo-NHS) are soluble in aqueous and organic solvents. Nevertheless, activation with non-sulfonate NHS decreases water-solubility of the modified carboxylate molecule, while activation with sulfo-NHS preserves or increases its water-solubility supported by the charged sulfonate group.[85]

2.2.4. The Biotin-Avidin-System

Until now, the interaction of the homotetrameric protein avidin and its ligand biotin forms one of the strongest known non-covalent bonds in biological systems characterized by a K_d in the range of 10^{-15} M.[86] First isolated from chicken egg white, it became a standard to use in biotechnology when researchers found a similar bacteria protein - streptavidin - in *Streptomyces* strains.[87] However, the charged glycoprotein avidin exhibits unspecific binding in some assays in comparison to streptavidin. Therefor, several companies developed deglycosylated forms of avidin with a neutral isoelectric point to minimize unspecificity. (NeutrAvidin, Extravidin, NeutraLite) In recent studies, a mutant streptavidin called "Traptavidin" exhibited an even 10 times dissociation rate.[88] As discovered in the early 1990s, biotin is bound inside a highly stable β -barrel structure and stabilized by hydrogen bonds as well as van der Waals forces.[89] In a unique mechanism, a side group of biotin (valerate) binds to a neighboring monomer of streptavidin and therefor stabilizes the dimer complex intrinsically.[90, 91] From a thermodynamical point-of-view, the interaction of the vitamin and protein is described by a total free binding energy of 300 kJ mol^{-1} to 330 kJ mol^{-1} for a tetrameric protein.[91] All these aspects lead to a significant rupture force for the biotin-release of $200 \pm 50 \text{ pN}$.[92]

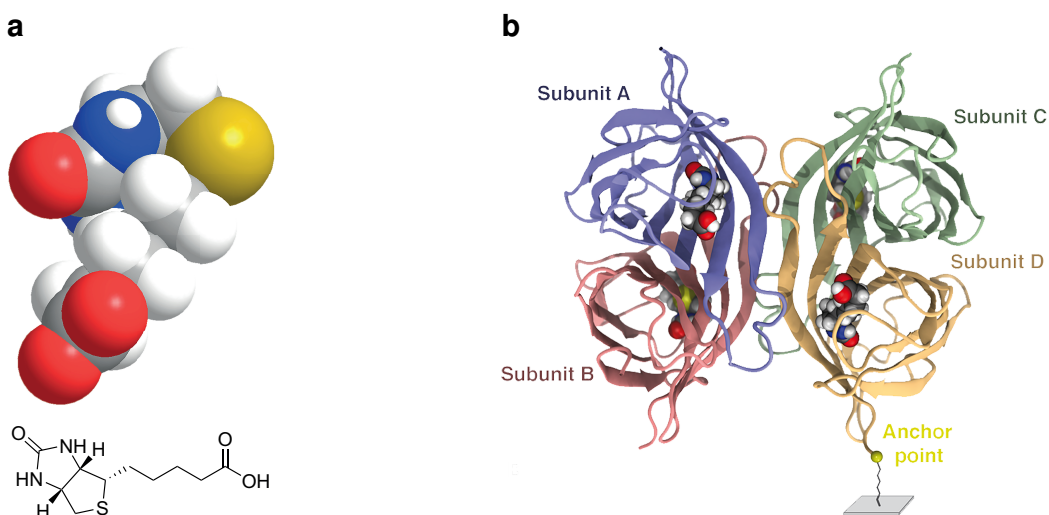


Figure 10: Functional Structures of Biotin and Streptavidin

(a) Two- and three-dimensional chemical structure of the biotin molecule. (b) Homotetrameric streptavidin with four subunits and four bound biotin-ligands. The molecule is attached with the anchor point at one terminus to a surface.[93]

2.3. Magneto-resistive Sensing

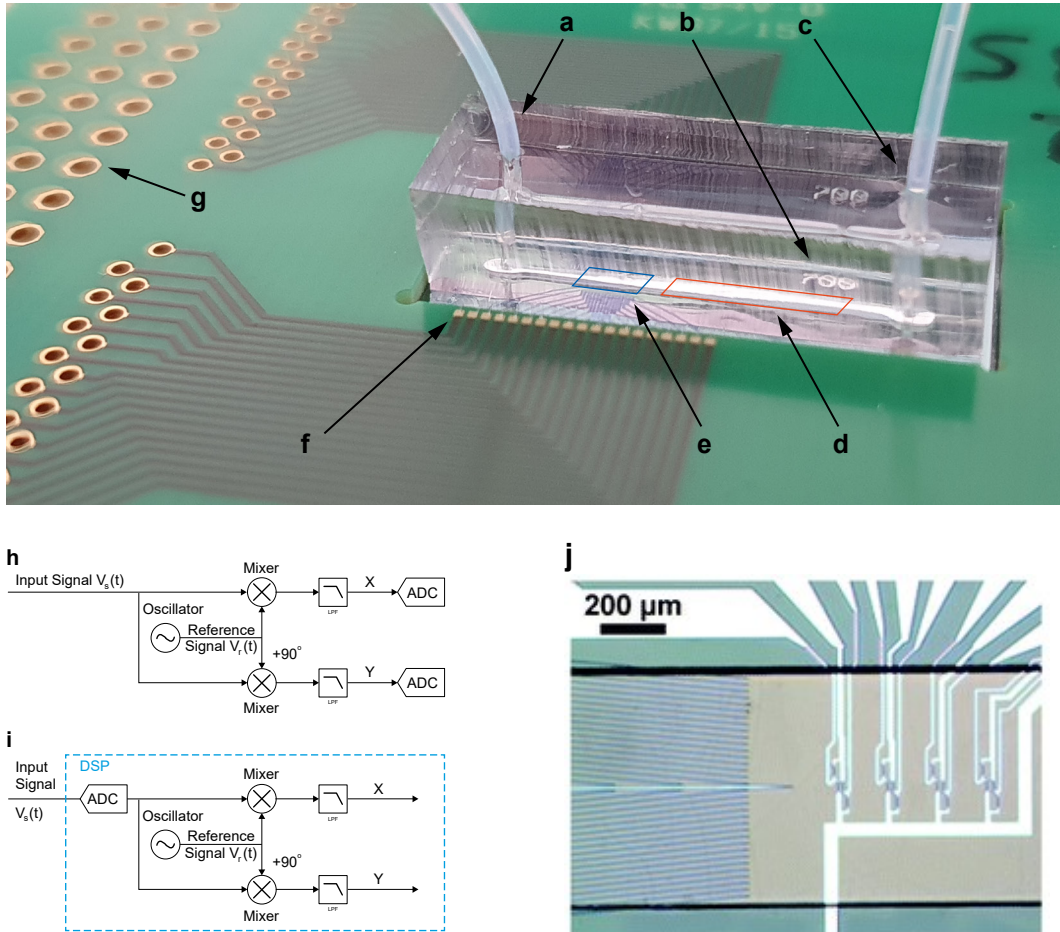
The measurement system's main component is a GMR-sensor stack with a measured magneto-resistive effect (MR effect) of ~8 %. GMR is a quantum mechanical MR effect observed in multilayers composed of alternating magnetic and non-magnetic conductive layers. The driving factor for this resistance is the mean free path of electrons in the interfacial regions of the soft ferromagnetic layer which is dependent on the relative spin orientation. Two magnetic layers with a thin conducting, non-magnetic spacer in the center build the base of the GMR stack.[94] One ferromagnetic layer is hard magnetic⁵, which is insensitive to outer magnetic fields. The so-called *free layer* is soft magnetic. Hence, it modulates its orientation in dependence on small coercive forces and is the main sensing component. [95]

In the case, if both layers are aligned parallel, applying a current to the sensor allows electrons to pass through the layers with less impact into spins on either side. Accordingly, the overall resistance is low compared to another extremum in the antiparallel alignment. The magnetization direction can be controlled, for example, by applying an external magnetic field.[96, 97]

In the present system, GMR stacks were used in a Wheatstone configuration, where two resistors act as a reference for bridge balancing. Upstream to the sensor, nickel-iron-based chevron patterns act as integrated focusing based on magnetophoresis for magnetic particles. These structures are driven by an external permanent magnet hence imposing a high flux density gradient on particles. Above these patterns, previously mentioned Si₃N₄ passivation has been deposited in thicknesses ranging from 50 nm to 500 nm to achieve inertness to biological samples. Nevertheless, a minimal passivation thickness is desired to measure the r^3 -decaying magnetic field sensitively and to reduce the magnetic diameter. On top of the sensor chip, a straight microfluidic channel is mounted to execute flow cytometry experiments.[13, 98]

Towards a sensitive measurement of the resistance-change, the lock-in principle is used. Here, an amplifier extracts signals in a defined frequency band around a reference frequency. This efficiently filters all other frequency components. Thereby a lock-in amplifier performs a multiplication of its input $V_s(t)$ with a reference signal $V_r(t)$ and low-pass filters the result $Z(t)$.

⁵ thus requires a high coercive field to become polarized magnetically



In most integrated cases, the reference signal is generated additionally by the lock-in amplifier itself. Using a pure sine wave as a reference enables the selective measurement at its fundamental frequency or any of its harmonics.[99]

At a measurement, $V_s(t)$ is split and separately multiplied with the reference signal and a 90° phase-shifted copy of it. After demodulation, the result is constituted from signal components at the sum and the difference of signal and the reference frequency, ω_s and ω_r , respectively.(Eqs. 3.36 to 3.38) In the resulting signal, the trigonometric functions are Euler transformed, and the magnitude $R = \sqrt{X(t)^2 + Y(t)^2}$ acts as measurand. The high frequency compounds are then filtered digitally by a low-pass filter of varying order n to increase the signal-to-noise ratio (SNR). As described in Eq. 3.40, a low-pass in the frequency domain can be described by a power series of first-order filters.

$$V_s(t) = \sqrt{2}R \cdot \cos(\omega_s t + \Theta) \quad 3.36$$

$$V_r(t) = \sqrt{2}e^{-i\omega_r t} = \sqrt{2} \cos(\omega_r t) - i\sqrt{2} \sin(\omega_r t) \quad 3.37$$

$$Z(t) = X(t) + iY(t) = V_s(t) \cdot V_r(t) \quad 3.38$$

$$= R \left[e^{i((\omega_s - \omega_r)t + \theta)} + e^{-i[(\omega_s + \omega_r)t + \theta]} \right] \quad 3.39$$

$$H_n(\omega) = H_1(\omega)^n = \left(\frac{1}{1 + i\omega\tau} \right)^n \quad 3.40$$

However, with this measurement principle, the SNR can not increase infinitely. If the signal strength cannot be increased, the noise has to be reduced or avoided as much as possible. Nevertheless, noise is always caused by different sources in analog signals, for example thermal, shot, and flicker noise. Other sources are of technical origin, as for example ground loops, crosstalk, 50 Hz noise, or electromagnetic pick-up. Predominantly, field aberrations or misalignment of the permanent magnet cause magnetic noise which dominates here.[99]

Now, to characterize a GMR with the lock-in, the free magnetization layer has to be confined in parallel and antiparallel configuration to the reference layer. For this, Helmholtz coils impose a magnetic field in $\pm 90^\circ$ of the free magnetization in order to measure the respective resistance. The lock-in captures a hysteresis during the sweep from parallel to an anti-parallel alignment of the layers at a specific bridge circuit. The steepness in the zero-field hereby indicates the sensitivity of a sensor element in the units V T^{-1} .

3. Materials and Methods

3.1. Magnetic Sensor Device

3.1.1. Assembly of Sensor

The fabrication of a microfluidic device on various substrates and layouts consists of two parallelizable workflows. First, the GMR-sensor chip (Sensitec GmbH, Germany) is assembled into a custom-designed PCB (PIU-PRINTEX GmbH, Austria) by double-sided adhesive tape and a square glass slide (25 mmx25 mm, Thermo Fisher Scientific, USA) at the bottom. The device is electrically contacted via wedge wire bonding (HB10, TPT Wire Bonder GmbH & Co KG, Germany) with an aluminium wire (\varnothing 25 μm). The optimal parameters are listed in table 1. However, crucial for successful wire bonding is

Parameters	Bond 1	Bond 2
Ultrasonic Power	250	300
Time / ms	200	200
Force / mN	250	300

Table 1: Wirebonding Parameters

the optimal hole shape in the welding tool. Therefore, it was cleaned when bonds failed for no obvious reason by removing the gold wire and dipping the tip of the wedge into isopropanol (IPA). Then, *Test USG* was alternated for several seconds in multiple iterations. Afterward, the wedge was blown dry from all sides with pressurized air and the wire was loaded back into the tool. After wire bonding, the manufactured sensors were placed in a wafer shipper box and stored in a dust-free environment for later use.

3.1.2. Design and Fabrication of Microfluidics

In the second workflow, a microfluidic channel was manufactured via photo- and soft-lithography and bonded to the magnetic sensors from 3.1.1.

Development of Layout

Layouts for the microfluidic channels were designed after common practices via AutoCAD (2020, Autodesk Inc., USA). The design was joined to single, closed polylines after the design finish. The files were also scanned for double lines or arcs as these cause failures in the downstream processing. The design was then exported to a compatibility *.dxf version with a single layer of polylines.

Patterning of Photoresist

3" (100) silicon wafers (Si-Mat - Silicon Materials e.K., Germany) were dehumidified in a drying oven (UN30, Memmert GmbH + Co.KG, Germany) for 2 h at 150 °C to 180 °C. Then, immediately after they reached room temperature, they were placed centered inside a wafer spinner (WS-650-23B, Laurell Technologies Corp., USA). For the desired layer thicknesses 2 mL to 3 mL SU8-30XX (Kayaku Advanced Materials Inc., USA) were poured carefully onto the center of the wafer and the following program was carried out:

1. 500 rpm for 10 s at 100 rpm s⁻¹
2. 3000 rpm for 30 s at 300 rpm s⁻¹
3. Ramp down at 300 rpm s⁻¹

Upon finish, the wafer was gripped outermost with wafer tweezers and soft-baked on a hot plate (Supernova+, Thermo Fisher Scientific, USA) for 5 min at 65 °C and at least 10 min at 90 °C. The optimal duration was determined if the gently touched resist did not stick to the tweezers. To prevent cracks in the resist caused by a fast temperature change, the wafer was cooled on the hotplate to room temperature. Such processed wafers were stored for a maximum of 4 weeks in a light-tight storage box.

To pattern the resist, the i-Line of a laser lithograph (Dilase 250, Kloé SA, France) was used. In preparation for the writing, a layout *.dxf-file was imported to the program “Kloe Design” (Kloé SA, France), converted to contours, and subsequently to polygons. For the filling, a spot-size equivalent to the minimal structure resolution (as measured in Hicsanmaz [100]) and an overlap of at least 50 % was chosen.

Departure and End Stabilization were chosen to 0.5 mm in a horizontal infill pattern. Also, flags for *auto-reverse mode*, *apply multiple trigger*, and *detect partial/full overlap* have been set. The writing trajectories were displayed in the last control step before the export to ensure only all contours had been closed properly. Last, the contour and filling were exported into separate files.

Both files were loaded in this order into the program “Dilase 250” (Kloé SA, France). The preprocessed wafer has been placed inside the laser writer and attached to the vacuumed stage. With the integrated camera, the global zero was set to the wafer center by finding the horizontal or vertical edges and adding/subtracting the radius of the wafer ($1.5'' \approx \varnothing 38.1$ mm). The focus point was set to the top of the resist and subsequently moved 0.07 mm relative down for thick layers. Then the program was initiated with 100 % laser modulation and 20 mm s^{-1} to 40 mm s^{-1} writing velocity.

Soft Lithography

The fabricated wafer has been placed at the center of a 90 cm petri dish. A PDMS mold was created by vigorous mixing of the pre-polymer base with its curing agent (Sylgard 184, Dow Silicones Corp., USA) in a ratio of 10:1 (w/w). For 3" wafers, thin channels were cast from 15 g, channels with standard thickness from 20 g PDMS in the petri dish. Gas bubbles were removed from the mixture in a desiccator for 20 min at 2 hPa, and the PDMS was cured in an oven (UN30, Memmert GmbH + Co.KG, Germany) for 1 h at 60 °C. After curing, the PDMS mold was released from the petri dish carefully, taken off the wafer, and stored in a clean petri dish upon further processing.

Bonding of Microfluidics

Under a laminar flow hood, crosslinked molds were cut into the single fluidics with a razor blade. Holes for in- and outlet were added with a biopsy puncher ($\varnothing 0.5$ mm, Welltech Labs, Taiwan). The substrates and channels were sonicated in acetone and deionized water (diH₂O) for 5 min and dried with filtered nitrogen gas (N₂) completely. For the bonding of PDMS to various substrates different protocols have been established:

PDMS Glueing

Here, a micron-height layer of uncured PDMS was used as an adhesive layer between the channel and the underlying substrate. Approx. 3 mL were poured onto a 3" wafer and spun down for 5 min at 6000 min^{-1} . The microchannel was placed on the substrate by visual control of a stereo microscope (SMZ800, Nikon GmbH, Germany) with 8-fold magnification. Subsequently, the bonding process could be finished by a 1 h bake at 60 °C or overnight at room temperature.

Plasma Bonding

The respective parts were activated by exposure to a controlled O₂-plasma. Bringing the activated surfaces in contact immediately triggers the formation of covalent bonds. First, the acetone-wiped substrates and the microchannels were centered inside the plasma cleaner (Zepto, Diener electronic GmbH & Co KG, Germany). Second, a vacuum was applied to a final pressure <0.2 hPa. Third, the chamber was flushed with pure O₂ until the chamber pressure was stabilized between 0.6 hPa to 0.8 hPa. Fourth, the plasma process was executed with 30 W (Power-Potentiometer: 100) for 45 s to 60 s (Time-Potentiometer: 15-20). Upon finish, the chamber was flushed for 5 s and ventilated. Immediately after, the corresponding workpieces were brought into contact and pressed together gently. To ensure a durable bond, the assembled structures were baked for 1 h at 60 °C.

Reversible Bonding

To bond the microfluidic to a substrate reversibly and without residues, the channel was brought into contact with the bottom part without any adhesion agent. For low-pressure as well as vacuum-driven flows, this method is preferable due to its time and work efficacy.

3.1.3. Peripheral Components and Optical Readout

Each sensor chip was characterized by the hysteresis steepness (equivalent to the sensitivity) and the zero-crossing at half-maximum in a customized setup. Therefore, the underlying 32 x 27 x 5 mm NeFeB magnet (NE3227, IBS Magnet e.K., Germany) was adjusted on micromanipulator tables (PT, Thorlabs GmbH, Germany) in three axes to optimize both parameters. Afterward, teflon-tubing (ID 0.5 mm, RCT Reichelt Chemietechnik GmbH + Co., Germany) was connected on the in- and outlet of the microfluidic. A dispensing tip (OD \varnothing 0.42 mm, Nordson Deutschland GmbH, Germany) was connected to the inlet tubing. Initially, a 1 mL syringe (ID 4.72 mm, Terumo GmbH, Germany) was connected with dH_2O or phosphate-buffered saline (PBS) and flushed with $100 \mu\text{L min}^{-1}$ to $200 \mu\text{L min}^{-1}$ by a syringe pump (Fusion 4000, Chemyx Inc., USA).

Hysteresis Alignment

Prior to the cell counting experiments, the GMR sensors were characterized. Adjustment of the position of the permanent magnet relative to the sensors was performed via hysteresis measurement.(Fig. 12) Therefore, an in-plane field was applied to the sensor was imposed by two Helmholtz coils ($L_s = 167 \text{ mH}$, $d = 150 \text{ mm}$, Dr. Brockhaus Messtechnik GmbH & Co. KG, Germany) generating 7.8 mT A^{-1} orthogonal to the easy axis of the GMR which were driven by a voltage-controlled current source (BOP 50-8M, Kepco Inc., USA) with $\pm 2 \text{ A}$ at a peak-to-peak voltage (V_{pp}) of 20 V. The control voltage was supplied by LabView (2018, 32-bit, National Instruments Corp., USA) supplied by a digital I/O card (USB-6351, National Instruments Corp., USA) in the range of -10 V to 10 V . The resulting sensor signal was fed into the current input of a lock-in amplifier (multi-frequency lock-in (MFLI), 5 MHz, Zurich Instruments AG, Switzerland) with a filter constant of 1 ms. Re-digitization and processing were carried out by the same digital I/O card and LabView program as for the input control. In effect, the sensitivity was computed from the hysteresis' steepness in the magnetic zero-field. Hereby, the very first hysteresis loop was omitted for further calculations because it contains the initial magnetization curve.(Fig. 12a) By differentiating the hysteresis (Fig. 12b), the maximum MR effect per unit magnetic field could be computed from the numeric maximum in $x = 0$. During the course of the thesis, it resulted typically in $1.2 \pm 0.2 \% \text{ mT}^{-1}$.¹

¹ It should be noted that this value depends on the normalization method. Typically, the sensitivity is measured from the hysteresis which is corrected for their minimum value per definitonem of the GMR effect. In a real measurement, an external actuation displaces the free layer from the magnetic zero-field. Therefore, a measurement would have to be corrected by the zero-field value. However, this causes a relatively small error which is solely relevant for quantitative calculations.

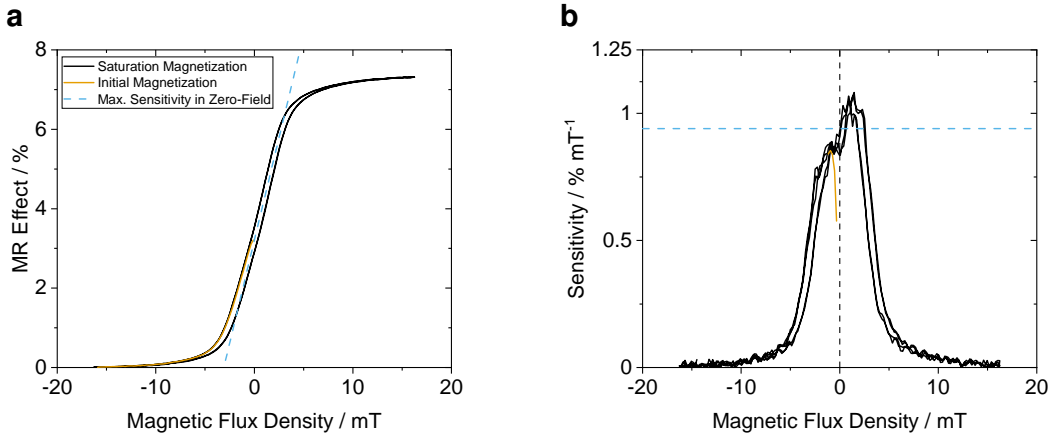


Figure 12: Hysteresis Calibration of the GMR-Sensor

Sensitivity Optimization of the GMR sensor via alternating hysteresis measurements and permanent magnet adjustment. (a) Optimal sensitivity is reached when the zero-crossing is centered around the zero-field and the linear section has the maximum steepness. (—) Upon dislocating the free layer in one direction, the magnetic field strength increases linearly towards saturation. (—) Afterward, the magnetization moves on the hysteresis loop. The total MR effect is calculated from the vertical distance between the saturation points. (—) (—) (b) In order to determine the steepness in the linear section, the hysteresis from the left side is differentiated. Actual sensitivity (—) is measured by the mean of all curves in the zero field. The initial magnetization curve is omitted from this measurement. (—)

From this, the bridge sensitivity could be also expressed in unit of $\Omega \text{ mT}^{-1}$. With a typical GMR resistance of $300 \pm 50 \Omega$ and a supply of $V_{pp} = 200 \text{ mV}$, the typical voltage drop results in $840 \pm 130 \mu\text{V mT}^{-1}$.²

Single GMR

The change in resistivity over one whole Wheatstone bridge was measured with the MFLI under a supply peak voltage (V_p) of 100 mV to 800 mV. The reference frequency was chosen randomly in a range of $100 \pm 25 \text{ kHz}$ such that any harmonics were avoided. The measured differential bridge balance was then demodulated and filtered with a time constant of $299.7 \mu\text{s}$ by a third-order low-pass filter and amplified by the factor 10 000. Subsequently, the processed signal was sampled at 53.2 kS s^{-1} from the MFLI and subsequently from a 16-bit analog-to-digital converter (USB-6351, National Instruments Corp., USA) with an input range of $\pm 10 \text{ V}$ and 10 kS s^{-1} .

During sensor operation, a 20x microscope image (DM2500M, Leica Microsystems GmbH, Germany) was captured by a CCD camera (Grasshopper3, FLIR Systems Inc., USA) and displayed in real-time to control the experiment.

² Output Voltage of one bridge branch: $V_{out} = \frac{R_{sig}}{R_{const} + R_{sig}} \cdot \frac{V_{pp}}{2\sqrt{2}}$

Dual GMR

For the measurement of two GMR-sensors simultaneously, the setup from 3.1.3 was duplicated in two different manners. However, the exact settings in the device control software were crucial for successful measurements. In a first approach, the supply cable of one MFLI was split and fed into both sensors, while the bridge balance was evaluated by the same and an additional lock-in, both with the same settings. Consequently, the ground pin of the one sensor was the reference also for the other sensor, and one ground pin was therefore left floating. This method posed the least cable length and therefore noise, but was also prone to crosstalk between the used BNC-cables respectively -connectors.

Second, two MFLI's were driven in a master-slave clock synchronization by the Multi-Device Sync function. Therefore, the *trigger out* and *clock out* ports on the backside of the master were connected to the slave's *trigger in* and *clock in* ports. Additionally, the *trigger out* was split by a T-connector piece in order to feed it also back into the master's *trigger in* port.

In both cases, the output of both lock-ins was directed to their respective *AUX 1* ports and connected to another LabView program by the previously mentioned DAQ-card.

Differential Sensor Setup

In some experiments, two PCBs were stacked with nylon spacers (D01482, DURATOOL Corp, Taiwan) with various lengths 3 mm, 5 mm and 8 mm between their edges above the permanent magnet. Before the stacking, the outlet tubing of the upper chip was connected to the inlet of the lower chip with the least dead volume possible.

Then, immediately before assembly, the channels were flushed with buffer and were inspected to confirm the absence of gas bubbles. After the final assembly, the hysteresis was adjusted for both sensors on various bridges consecutively. Measurements were performed as described in 3.1.3 with two completely independent lock-in amplifiers.

GMR Data Analysis

Subsequent data analysis of the acquired streams from both two and one sensor measurements were modified by a custom LabView VI to cut the first sample of the stream which was mandatory for the next step. Next, the characteristic signal patterns were detected in the continuous stream by the *GMR_Tool_227* by a rolling-mean thresholding method. The resulting **.ana.csv* files were then processed by a custom Matlab script, which in turn computed averages and simple parameters of a single detected signal or whole measured, p.e. the total volume or the signal count therein. The Matlab script saved any analyzed data also in the **.csv* format.

3.2. Magnetic Beadometry

Magnetic beads were measured in various manners. First, beads were pumped over substrates under microscope control (DM6, Leica Microsystems GmbH, Germany) with simultaneous image acquisition for count (LAS X, Leica Microsystems GmbH, Germany) and trajectory analyses (ImageJ Fiji, [101]). Second, beads were measured in buffer or diluted whole blood samples to determine their concentration in the magnetic flow cytometer. The previous measurements were then adapted to functionalized surfaces in order to detect a difference in concentration. In all experiments, teflon tubing (ID 0.5 mm, RCT Reichelt Chemietechnik GmbH + Co., Germany), dispensing tips (OD 0.42 mm, Nordson GmbH, Germany), 1 mL syringes (ID 4.78 mm, Terumo GmbH, Germany), a syringe pump (Fusion 4000, Chemyx Inc., USA) and a microfluidic channel with dimension 700 μm x 150 μm (width x height) were used.

3.2.1. Optical Particle Tracking

In order to track particles in microscopy images pictures were processed in Fiji (ImageJ, [101]). Subsequently, they were either counted manually in a measured volume or tracked by the TrackMate Plugin [102].

Initially, the microscope pictures were imported with the *BioFormats Importer* as tiff-stacks. The region of interest was selected with a polygon and cropped. Then, the stack was converted to 8-bit and thresholded by the *Yen dark* algorithm. After inverting the images, a slice with no visible beads was subtracted from the stack. The result was used for manual counting.

For the tracking, the *LoG-Detector* with a *blob diameter* of 8 μm has been used with a threshold of 2.0. Additional flags were set for *use median filter*, *subpixel localization*, and *hyperstack*. The resulting particle detections were visualized by their respective SNR. Subsequently, the *linear motion LAP tracker* was initialized with a motion radius of 60 μm and a search radius of 60 μm through the maximum frame number.

3.2.2. Absolute Concentration Measurement

Before every measurement, the initial bead concentration was determined meticulously in a Neubauer Improved counting chamber or by flow cytometry and adjusted between 1 μL^{-1} to 10 μL^{-1} in PBS with Tween 20 (PBST).

Then, after the sensor was calibrated accordingly in the single or dual GMR-setup (Sec. 3.1.3), beads were pumped at a fixed flow rate of $80 \mu\text{L min}^{-1}$ and $30 \mu\text{L min}^{-1}$ through a channel with $150 \mu\text{m}$ or $50 \mu\text{m}$ height, accordingly. Either the previously mentioned plastic syringe or a 1 mL glass syringe (1001 TLL, Hamilton Bonaduz AG, Switzerland) was utilized in a syringe system for these experiments. The duration to attain statistical significance was specified by a minimal volume of $300 \mu\text{L}$ or detection of at least 300 particles. Between samples, the whole system was flushed with PBST at flow rates greater than $150 \mu\text{L min}^{-1}$ or $60 \mu\text{L min}^{-1}$, respectively to $150 \mu\text{m}/50 \mu\text{m}$ channel heights. Afterward, signal streams were analyzed according to the procedure in Sec. 3.1.3.

3.2.3. Whole Blood Bead Spiking

For measurements in whole blood samples, 6 mL blood were drawn from test subjects in 7.5 mL , $2,2',2'',2'''$ -(ethane-1,2-diyl)dinitrilo)tetraacetic acid (EDTA)-containing vials (S-Monovette Hämatologie, Sarstedt AG & Co. KG, Germany). Beads with precise concentrations were prepared according to Sec. 3.2.2 in PBS. Then, several dilutions of whole blood were created from the particle solutions and mixed carefully with a 1 mL micro-pipette or by inversion. The samples were subsequently measured at a fixed flow rate of $40 \mu\text{L min}^{-1}$ in a $150 \mu\text{m}$ channel. In between samples, the channel has been flushed with MACS running buffer (MACS) buffer at high flow rates as in Sec. 3.2.2. The best measurements arose from S48 chips with broad, 200 nm -high nickel-iron structures.

3.2.4. Bead Capture Assay

As prerequisite for the bead capture assay, the different self-biotinylated particles - from Sec. 3.3.4 - were diluted as for the concentration measurement in Sec. 3.2.2. Further, a GMR sensor was fabricated, loaded unspecifically with 1 mg mL^{-1} neutravidin, hysteresis aligned and connected in the single GMR setup (see 3.1.3). As first step, the bead adhesion was determined by finding the minimal flow rate at which non-biotinylated beads were still rolling freely and at second, by finding the maximal flow rate at which biotinylated beads were still notably captured, both by microscope observation and sensor signal analysis. The average flow rate of these two was consequently held constant over all experiments. Subsequently, beads with different surface coverages of biotin were pumped alternatingly through the channel and over the sensor. The generated data was analyzed after the standard protocol in 3.1.3.

3.3. Surface Bio-Functionalization

3.3.1. Surface Activation

To functionalize any silicon-containing surface with Si—OH groups which the utilized silane could interact with, multiple surface activation pathways were explored. First, substrates were cleaned in hydrochloric acid (HCl):methanol (MeOH) and H₂SO₄ before they were immersed in boiling water. Second, surface silanol groups were achieved by piranha immersion. Third, a HF dip and, fourth, an O₂-plasma treatment was tested. For all methods, the following reagents were used: diH₂O (0.054 µS, Merck MilliQ), acetone (>99.9 %, VWR International LLC, Germany), ethanol (EtOH) (absolute, VWR International LLC, Germany), MeOH (99.8 %, VWR International LLC, Germany), acetic acid (AcOH) (glacial, VWR International LLC, Germany), HCl (37 %, Merck KGaA, Germany), H₂SO₄ (95 % to 98 %, Merck KGaA, Germany), H₂O₂ (30 % (w/w), Merck KGaA, Germany), HF (10 %, VWR International LLC, Germany), MACS (MACSQuant Running Buffer, Miltenyi Biotech, Germany), 2-(N-morpholino)ethanesulfonic acid (MES) (145224-94-8, Merck KGaA, Germany), EDC (25952-53-8, Merck KGaA, Germany), NHS (6066-82-6, Merck KGaA, Germany), APTES (919-30-2, Merck KGaA, Germany), poly(acrylic) acid (PAA) (9003-01-4, Merck KGaA, Germany), neutravidin (31050, Thermo Fisher Scientific, USA)

Work Safety Remarks

Before the work with one of the acid solutions was carried out, several safety measures were implemented. As any reacting acid solution becomes very hot immediately due to the exothermic reaction, every container should be placed inside cooled water or ice bath. Additionally, the beaker, as well as concentrated acid flasks, should be gripped firmly by a laboratory stand to avoid a tip over. As the reactivity of chemicals is highly temperature-dependent, the solutions were processed further when they had been cooled to ≤ 80 °C. It should be also noted that - as in every chemical reaction, but especially ones with H₂SO₄ and HF - the acid was always poured into the other reactant to avoid splashing and boiling.

Plasma Activation

For the plasma activation, process parameters similar to the PDMS bonding technique in Sec. 3.1.2 were chosen. After initial cleaning via sonication in AcOH and diH₂O for 5 min each, the substrates were dried in N₂-gas and placed inside the plasma chamber.

The chamber was evacuated to a final pressure <0.2 hPa and then flushed with pure O₂ until a chamber pressure between 0.6 hPa to 0.8 hPa had been stabilized. Fourth, the plasma process was executed with 100 W (Power-Potentiometer: 300) for 300 s (Time-Potentiometer: 190). Upon finish, the chamber was flushed for 5 s and ventilated.

Hydrochloric-Sulfuric Acid Activation

In order to degrease any glass or Si₃N₄ surface, a protocol according to Dressick et al. [78] was used. There, the surfaces were first sonicated in acetone and diH₂O for 5 min. Afterward, these were immersed in a 1:1 (v/v) solution of HCl:MeOH for >30 min, rinsed with diH₂O copiously, and soaked in H₂SO₄ for >30 min as well. Then, the samples were rinsed again in deionized water. To form silanol groups on the activated surface, the surfaces were finally immersed in >90 °C heated (SuperNuova+, Thermo Fisher Scientific, USA) diH₂O for at least 2 h.

Piranha Activation

In this method, activation was carried out in a 1:7 (v/v) piranha solution at 70 °C for 1 min to 30 min. After treatment, the samples were rinsed carefully with diH₂O three times.

Hydrofluoric Acid Activation

For HF activation of Si₃N₄, a protocol after Liu et al. [72] was reproduced. Acetone cleaned samples were immersed in 1 % aqueous HF for 2 min and rinsed with diH₂O extensively afterward without letting the surface dry at any time.

3.3.2. Chemical Surface Functionalization

Chemically activated surfaces were now coupled with APTES covalently. Therefore an aqueous silane solution was prepared from EtOH with volume fractions of 5 % diH₂O, 0.5 % aqueous AcOH (pH 4.5) and 1 % APTES in this order. The samples were soaked immediately after their activation in the silane solution. The reaction was carried out for 2 h to 4 h at >40 °C or for 1 h at 70 °C. Upon finish, all specimens were rinsed with EtOH or sonicated for 5 min in absolute EtOH.

Then, the amine-terminated surface modification was enhanced by a carbodiimide conjugation with PAA after Andree et al. [80]. As above, a reaction consisting of 1 mM MES buffer (pH 6) with 1 mg mL⁻¹ PAA, 6 mM EDC, and 3 mM NHS was activated for 15 min on a magnetic stirrer. Subsequently, the prepared samples were immersed in the solution for 1 h on a rotation shaker. As final cleaning, the slides were rinsed or sonicated for 5 min in diH₂O and stored in fresh diH₂O at 4 °C up to 14 d upon further use.

Tensiometry

All the above methods were characterized by a custom-built tensiometer and the ImageJ Fiji plugin DropSnake. [101, 103] In an experiment, a substrate was dried by N₂ and placed in the camera focus. Subsequently, a sessile drop of 1 µL was placed in the focus with a micro-pipette without touching the surface. The focus of the camera was adjusted meticulously to gain maximum contrast at the droplet contour and a homogeneously black droplet. Images were then acquired by an USB microscope (toolcraft AG, Germany) pointing at an acute angle onto a drop on the surveyed substrate, while background illumination was provided by a fiber optical illuminator (KL1500, Schott AG, Germany). The images were then cropped, rotated such that the droplet edges were aligned horizontal and converted to 8-bit grayscale. After preprocessing, the top half contour was outlined by at least 8 points inside the DropSnake plugin, and the resulting contact angles were exported.

3.3.3. Surface Bioconjugation

A functionalized surface from 3.3.2, was now bonded to a 150 µm microfluidic channel as in 3.1.2 and incubated for at least 5 h, but mostly overnight at 7 °C. Upon finish, microfluidic Teflon-tubing (ID Ø 0.5 mm, RCT Reichelt Chemietechnik GmbH + Co., Germany) was connected to the inlet and outlet with precision tweezers. Then, the channel was equilibrated with 100 µL to 300 µL MES buffer in a syringe (1 mL, Terumo GmbH, Germany) with a syringe pump (Fusion 100, Chemyx Inc., USA) with 100 µL min⁻¹. Then, 50 mM, 100 mM, and 300 mM of EDC and NHS were flushed into the channel with the same flow rate after a dissociation time of 10 min. The channel bottom was incubated for 30 min and then washed again with 100 µL MES buffer.

Subsequently, the desired protein was loaded in high concentration (Neutravidin: 1 mg mL⁻¹, Antibody: 20 µg mL⁻¹), via the tip of a 1 mL syringe or flushed into the channel by vacuum from a microcentrifuge tube. The functionalized channels were now incubated overnight in an ice box. Before use, the channel was washed with 100 µL PBS with 0.02 % nonionic surfactant (Tween 20, Merck KGaA, Germany) (PBST) for 2 min. Any unreacted binding sites were blocked by a solution of 500 mM ethanolamine hydrochloride (E6133, Merck KGaA, Germany) in diH₂O for 30 min. After another washing step, the functionalized channels were further used for either microscope or magnetic bead-capture experiments.

However, in some experiments focus lay on physisorption rather than on chemisorption. Therefore, after the bonding of a microfluidic channel to a non-functionalized substrate, the channel was equilibrated as mentioned before with MES buffer (cave: without surfactant). Then it was incubated with a solution containing protein in highest concentration, p.e. 1 mg mL⁻¹ neutravidin, at 7 °C over night, while infusing and withdrawing a small volume fraction (approx. 50 µL) continuously by a syringe pump. Upon finish, the tubing was exchanged with a drop of water at the connection and channel was flushed with PBS carefully at 50 µL min⁻¹ to avoid any gas bubbles inside the fluidic. It was stored up to 10 d without any notable decrease in functionality.

3.3.4. Particle Functionalization

Micro- and nanobeads from different suppliers were used in functionalization experiments but modified after the same procedure according to their surface charge. A positive partial charge from an amine-terminated bead and a negative partial charge from a carboxyl-terminated bead was used to promote different electrostatic interactions with a microchannel's surface. A list of all used particles and their respective parameters are depicted in table 2.

Supplier	Brand Name	d (μm)	Functionaliza-tion	Surface Charge ($\mu\text{mol g}^{-1}$)	Magnetic Particle Momentum (A m^2)
micromod	micromer	8	amine	2.0	0
micromod	micromer-M	8	amine	1.0	$>1.12 \times 10^{-12}$
micromod	micromer	8	carboxyl	2.0	0
micromod	micromer-M	8	carboxyl	1.0	$>1.12 \times 10^{-12}$
invitrogen	Dynabead M280	2.8	streptavidin	0.65-0.90	N.A.
invitrogen	Dynabeads MyOne C1	1.05	streptavidin	>2.5	N.A.
Ocean Nanotec	SV0050	0.05	streptavidin	N.A.	N.A.
micromod	BNF-Dextran-redF	0.1	streptavidin	0.2	$>1.27 \times 10^{-16}$
micromod	nanomag-D-spio	0.1	streptavidin	0.02-0.04	$>5.5 \times 10^{-17}$

Table 2: Properties of the used microbeads and MNPs.

Amine-terminated Beads

For amine beads, NHS-Biotin (203118, Merck KGaA, Germany) was used for a covalent attachment after the previously mentioned carbodiimide chemistry. Initially, the biotin was dissolved to a concentration of (50 mg mL^{-1}) in water-free dimethyl sulfoxide (DMSO) (67-68-5, Merck KGaA, Germany) and stored upon further use at -25°C . The attachment to microbeads was titrated by the molar weight ratio of both reagents and ranged from 10-fold molar excess to a 10 000-fold deficit of biotin over the amine.

In most cases, $20 \mu\text{L}$ of micromer beads were aliquoted in several microcentrifuge tubes (1.5 mL , Protein LoBind, Eppendorf AG, Germany) to generate a standard curve of functionalization density later on. NHS-Biotin was diluted to a concentration of 0.5 mg mL^{-1} with PBST and vortexed. Then, beads and biotinylation reagent were mixed in the desired ratio thoroughly and incubated for 1.75 h at 8°C in a shaker at 1400 min^{-1} .

Carboxyl-terminated Beads

The surface of carboxyl-terminated beads was esterified by EDC-NHS chemistry and covalently bound to amine-PEG₂-biotin (EZ Link, Thermo Fisher Scientific Inc., USA). First, the bead buffer was exchanged to MES buffer with Tween 20 (MEST) with one washing step by centrifugation (as in 3.3.4) to a final bead concentration of 5 mg mL^{-1} . 100 mM EDC in diH₂O and 50 mM NHS in DMSO were prepared and added to the bead solution to a final concentration of 25 mM and 12.5 mM each. The suspension was reacted for 30 min on a shaker at 1400 min^{-1} and washed once with MEST buffer. Then, amine-PEG₂-biotin was added from 10-fold molar excess to a 10 000-fold deficit of biotin over the amine and volume adjusted. The samples were incubated on a shaker for 1.75 h at 8°C in a shaker at 1400 min^{-1} .

Post-Processing and Characterization of Beads

After the incubation, the beads were washed either magnetically or via pelleting. Magnetic washing was carried out in a magnet stand, where the beads were separated for 2 min and then washed 3 times with 500 μ L to 1000 μ L PBST. Pellet washing was conducted three times in a centrifuge (Fresco 17, Thermo Scientific) at 800 \times g to 1200 \times g for 10 min. The supernatant was discarded and the pellet was dissolved in 500 μ L to 1000 μ L PBST. After both washing procedures, the beads were resuspended in 100 μ L MACS or PBST and stored at 4 °C.

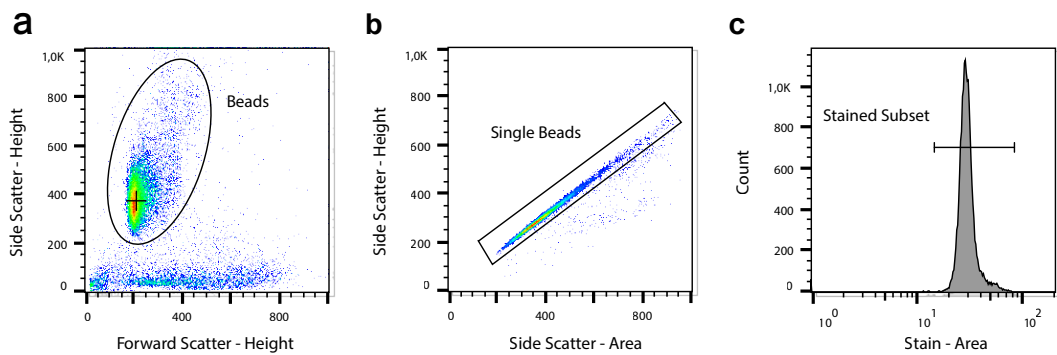


Figure 13: Gating Strategy for Biotinylated Beads

(a), In the forward-side-scatter plot, the general bead population with high side scatter was selected from the background. (b), Single beads were differentiated by their sphericity; their ratio of height:area in the side scatter. Points on the line through the origin are spherical. (c), The stained subset in the respective color was now selected and the median fluorescence intensity (MFI), as well as the coefficient of variance (CV), were computed.

Characterization of any surface modification was done via fluorescence-flow cytometry or -microscopy. 30 000 beads to 60 000 beads were diluted to 20 μ L and incubated with 100 ng streptavidin-atto488 (49937, Merck KGaA, Germany) or Anti-Biotin-PE (REA746-PE, REAfinity, Miltenyi Biotec B.V. & Co. KG, Germany) for 30 min at 8 °C in a shaker. The beads were then diluted to a final volume of 100 μ L, transferred to a 96-well plate and measured in the autosampler of a flow cytometer (MACSQuant Analyzer 10, Miltenyi Biotec B.V. & Co. KG, Germany). Data analysis was performed by FlowJo (10.6.2, Becton Dickinson GmbH, Germany) after a gating strategy which is depicted in Fig. 13.

Following parameters were held constant over all measurements: *Flow Rate*: High, *Mix Sample*: Strong, *Mode*: Standard, *Uptake/Sample Volume*: 100 µL. The photomultiplier voltages of forward and side scatter were lowered in most experiments by 10 V and 120 V respectively due to the homogeneous and reflective nature of the particles.

For fluorescence microscopy, the beads were stained with streptavidin-atto488 after the same procedure and imaged statically on a covered microscope slide at an exposure time of >100 000 µs and a gain >15. Images were then processed in Fiji.

Coating of Biofunctionalized Non-Magnetic Beads with Magnetic Nanoparticles

The biotinylated, non-magnetic microbeads (Table 2) were coated covalently with different MNPs in order to establish a bead-side titration of binding sites. Therefore, 5 mg mL⁻¹ biotinylated beads in PBST were equilibrated for 10 min and mixed with 7.5 µg BNF-dextran-redF-streptavidin / nanomag-D-spio, 6 µg of SV0050 or 10 µg Dynabeads C1 over night on a shaker. Afterward, the supernatants were exchanged twice by careful centrifugation to avoid sedimentation of the nanoparticles.

4. Results and Discussion

4.1. Virtual Prototyping of Cell Signals

During the course of this thesis, numerical simulations for the microchannel have been carried out in MATLAB. First, a simulation about the shape of a GMR-sensor signal of cells was performed, where the magnetic moment was conveyed through MNPs bound to their surface. Second, cell aggregates have been looked at in the same manner with different angles respective to the sensor. Third, both simulations were correlated to a reference dipole, with the equivalent magnetic moment located in the center of mass. Additionally, the flow and shear field inside the channel was simulated numerically for the channel cross-section as well as for a particle near the walls. A force equilibrium simulation was also established in a basic manner.

All simulations have been captured inside the MATLAB class “MRCyte”, which contains material parameters, constants, and the necessary functions for all simulations above.

4.1.1. Numerical investigation of immunomagnetic label density and size on quantitative magneto-resistive sensing of single cells and cell aggregates

In order to mimic an immunomagnetically labeled cell flowing over the sensor half-bridge, the planar integral of the respective magnetic flux density (\mathbf{B}) was solved analytically. Here, \mathbf{r}_i specifies the distance vector of a single MNP from the sensor plane. The magnetic flux density was converted to a resistive change \mathbf{R}_{sig} by scaling it with the GMR-sensitivity S and subsequently into a signal voltage \mathbf{V}_{sig} inside the bridge branch.(Eqs. 1.1 to 1.3)

$$\mathbf{B}(t) = \sum_{i=1}^N \frac{1}{A_{\text{Sensor}}} \int_{-\frac{l}{2}}^{\frac{l}{2}} \int_{-\frac{w}{2}}^{\frac{w}{2}} \frac{\mu_0}{4\pi} \left(\frac{3\mathbf{r}_i(t) (\mathbf{r}_i(t) \cdot \mathbf{m}_i)}{|\mathbf{r}_i(t)|^5} - \frac{\mathbf{m}_i}{|\mathbf{r}_i(t)|^3} \right) dx dy \quad 1.1$$

$$\mathbf{R}_{\text{sig}}(t) = -\mathbf{B}(t) \times \frac{S}{100} \times R + R \quad 1.2$$

$$\mathbf{V}_{\text{sig}}(t) = \frac{\mathbf{R}_{\text{sig}}(t)}{R + \mathbf{R}_{\text{sig}}(t)} \times V_p - \frac{V_p}{2} \quad 1.3$$

First, MNPs were randomly sampled on a sphere surface with a diameter of $4\text{ }\mu\text{m}$ or $8\text{ }\mu\text{m}$. Then, the signal was computed from the superposition of every MNP during each timestep. Additionally, the MNP distribution was rotated in every iteration to resemble a rolling motion. The computed signals were then cross-correlated to the signal of a reference flux density \mathbf{B}_{ref} caused by a point-like magnetic moment located in the geometric center of the same sphere. By its formula, cross-correlation $R_{xy}(\tau)$ yields a displacement dependent signal through its convolution of the complex conjugated reference signal $\mathbf{V}_{\text{ref}}^*(t)$ with the sample signal $\mathbf{V}_{\text{sig}}(t + \tau)$. (Eq. 1.4) Therefor, only the maximal correlation of this function was considered in further analyses.

$$\max\{R_{xy}(\tau)\} = \max \left\{ \int \mathbf{V}_{\text{ref}}^*(t) \mathbf{V}_{\text{sig}}(t + \tau) dt \right\} \quad 1.4$$

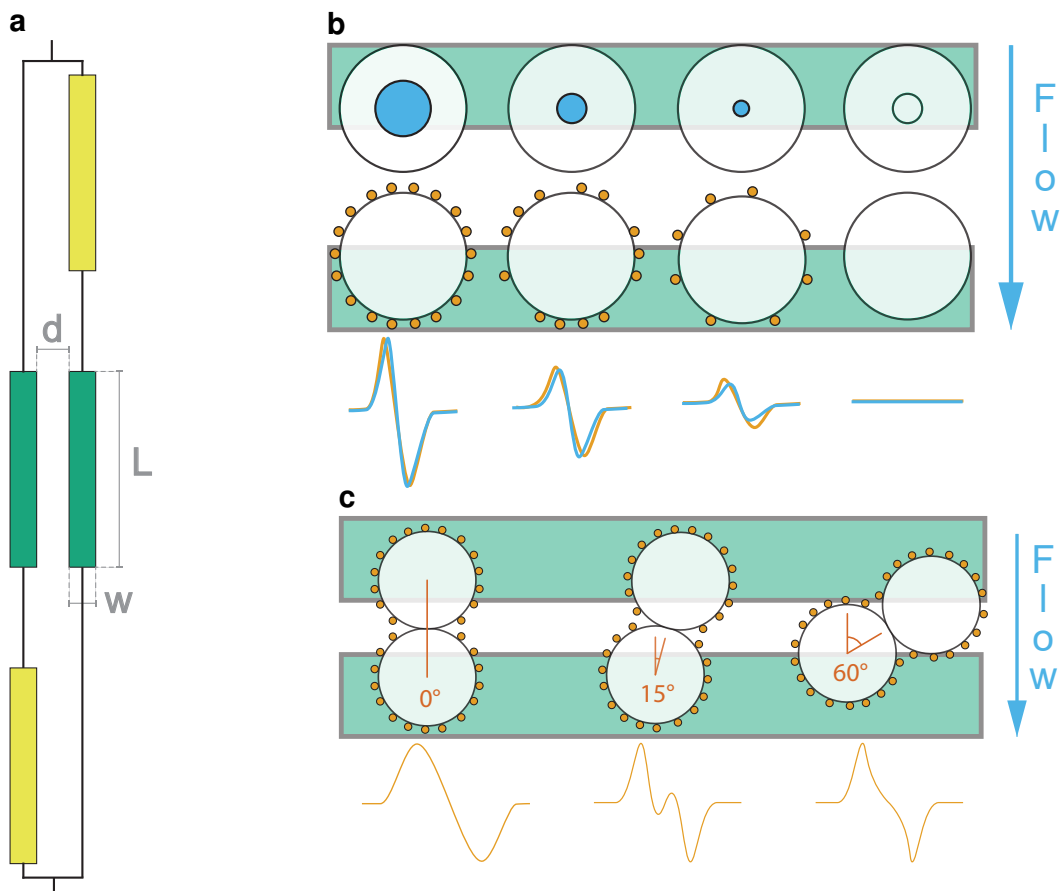


Figure 14: Particle Coverage Simulation

(a) Dimensions of the GMR Wheatstone bridge sensor: Distance d between both variable bridges (green), width w of a GMR-sensor, length L of a sensor. (b) Scheme of single-cell simulation: The ideal magnetic dipole in the geometric center of a sphere (●) causes a signal deviation from the real cell signal with magnetic moment distributed on the cell surface. (●) (c) Signal shapes of different angles of two-particle aggregates lead to differing signal shapes.

4.1.2. Single-Cell Signals

The aim of these simulations is to find a measure of how magnetic labeling of a cell affects its signal shape and subsequent analysis. A single cell with a surface coverage of 5 % to 99 % of a densely packed sphere was loaded randomly with MNPs of different sizes. Then, the previously explained rolling motion over the sensor bridge was simulated with the parameters specified in Table 3. After correlating of the resulting signal voltage to the reference dipole (Fig. 14b,), each with three equal, randomly distributed MNP coverages, the dependency on the coat was evaluated. As shown in the schematic Fig. 14b, an increase in signal peak amplitude but also in full width at half maximum (FWHM) at growing coverage was expected.

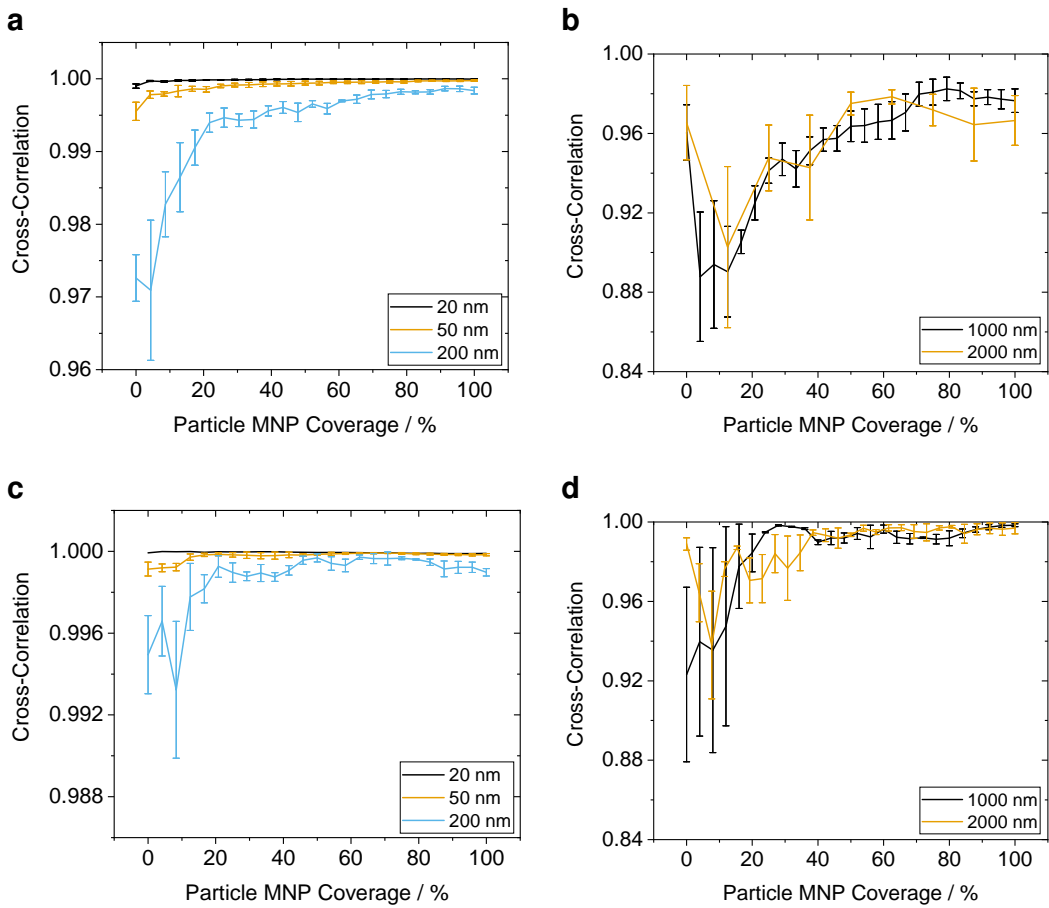


Figure 15: Coverage Dependent Signal Correlation

MNP coverage of a sphere with 4 μm (**a, b**) and 8 μm diameter (**c, d**) covered by magnetic particles ranging from 20 nm to 2000 nm. A cross-correlation increase which is inversely proportional to the MNP size can be observed.

The expected behavior matches the data analysis (Fig. 15). Each two analyzed sphere diameters 4 μm and 8 μm with MNP sizes ranging from 20 nm to 2 μm , show a great standard error of the mean (SEM) at low coverage. This very probably is subjected to the momenta of single particles which play a greater individual role and hence influence the signal shape significantly because the overall dipole moment in the sensor loses homogeneity.

Another observable effect is related to the MNP size. Absolute correlation differs from 20 nm to the ten and hundred-fold diameter significantly. This can be related to the magnetic moment per MNP as it is dependent on the volume - thus r^3 .

However, for bigger magnetic particles this does not completely hold because the composition changes from pure magnetite to a polymer shell with embedded oxide core at around 150 nm. Nevertheless, larger particles carry also greater magnetic moment which brings the aforementioned influence of single MNPs into consideration.

Further, the densely packed sphere surface can carry substantially more smaller than larger MNPs. This ranges from 641 600 MNP of 20 nm to 81 of 2 μm for a sphere radius of 4 μm and thus limits the maximum achievable moment.

In reality, a maximum immunomagnetic label density depends not on the densely packed sphere but rather on the present antigens, and association or dissociation constants. Therefore, a complete saturation coverage is not achievable under physiological conditions. When using smaller particle sizes, it has to be taken into consideration that a cumulative magnetic moment is limited by the number of antigens and the detection limit of the sensing setup.

$$\text{Relative Correlation Difference} = 1 - \frac{\max\{\text{Cross-Correlation}(d = 4 \mu\text{m})\}}{\max\{\text{Cross-Correlation}(d = 8 \mu\text{m})\}} \quad 1.5$$

$$\text{Relative Correlation Difference} = -0.385\,32 d_{\text{MNP}}^2 + 3.345\,74 d_{\text{MNP}} - 8.496\,29 \quad 1.6$$

Also, it can be seen that the correlation approaches a maximum obtainable value for every MNP size. Referenced for both simulated sphere diameters in Fig. 17a, an inverse proportionality between correlation and MNP diameter is visible. The trend in respective maxima can be attributed to variations in the magnetic moment, and coverage inhomogeneity.

Inter-sphere compared, maximum correlation shows also a significant deterioration for higher MNP sizes as the particle diameter itself increases. The relative error between both sizes - as computed in Eq. 1.5 - is depicted in Fig. 17b. Assuming a dependency on the available particle surface and subsequently the fraction which can be occupied by MNPs, a quadratic fit seems appropriate.(Eq. 1.6) The fit indicates probably that a cell covered with small MNPs resembles a magnetic dipole located in the center of the cell while the correlation error becomes nearly constant at great MNPs.

Parameter	Unit	Value	Explanation
w	m	2.0×10^{-6}	GMR width
l	m	30.0×10^{-6}	GMR length
d	m	14.0×10^{-6}	Distance between two sensors
R	Ω	250	GMR Resistance
V_p	mV	100	Supply voltage
$t_{\text{free layer}}$	m	7.0×10^{-9}	Thickness of free layer
M	A m^{-1}	2.0×10^4	Volume Magnetization
$V_{\text{noise,rms}}$	V	2.5×10^{-6}	Artificial noise
Sim. Space	m	$[-25 \times 10^{-6}, 25 \times 10^{-6}]$	Interval around sensor center

Table 3: Magnetic Simulation Parameters

Constants used inside the framework for the simulation of the magnetic field inside the GMR Wheatstone half-bridge. The volume magnetization was adapted according to the simulated particle size.

4.1.3. Cell Aggregates

In another simulation, two 200 nm-MNP-covered spheres were attached in different angles and simulated flowing over the sensor. Signal similarity to a magnetic dipole in the center of a single reference sphere was computed by cross-correlation. As can be observed in Fig. 16, correlation is identical to a single sphere at low coverage, above a threshold magnetization. Here, the randomly distributed particles span an inhomogeneous magnetic field of a larger sphere which cannot be subdivided into the two singular parts.

With growing coverage, each cell starts to form an independent dipole. At occupancies greater than 50 %, the two attached cells are in such superposition. Now, the sensor detects not a single particle as for less coverage but two spatially close particles. Consequentially, the signal is an interference pattern of the two singular events and thus carries small peaks in the center. This is shown schematically in Fig. 14c. In term, this causes a high signal deviation from the reference and a low degree of correlation effectively.

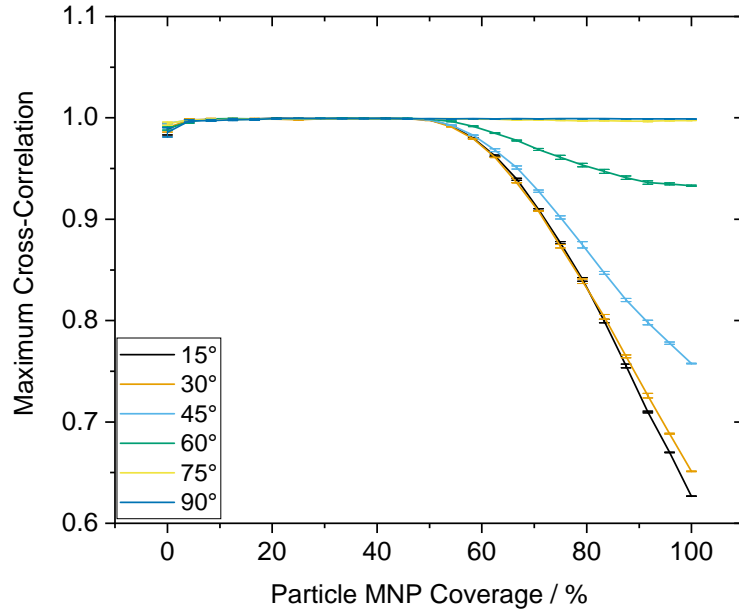


Figure 16: Signal Correlation between Two-Cell Aggregates At Shifting Angles

Two-Sphere aggregates are covered with 200 nm MNPs and simulated flowing over the sensor at differing respective angles. The SEM indicates a difference in the cross-correlation of three truly random MNP distributions. For low yaw angles and high coverages, the aggregate's signal reflects rather two single dipoles in superposition than one quite homogeneous dipole. This causes a high signal deviation from the reference and thus a low degree of correlation.

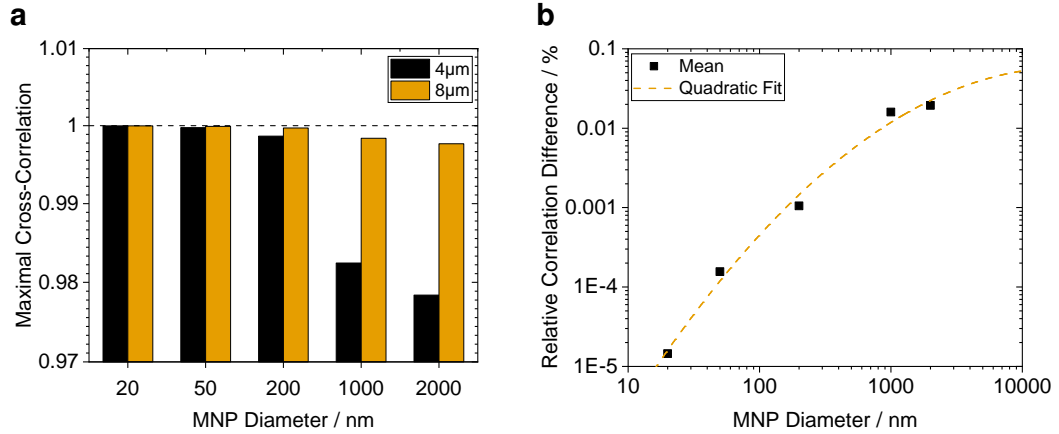


Figure 17: Maximal Cross-Correlation Differences

- (a) Mean coverage at 99 % for 4 μm and 8 μm spheres. A negative dependency on the MNP size can be explained by the ratio of magnetic moment per unit surface and its homogeneous distribution across the whole surface.
- (b) Relative correlation error between 4 μm and 8 μm spheres with a quadratic fit. The quadratic behavior could be related to the relative surface area which can be occupied by magnetic moment. (Adj. $R^2 = 0.992\,09$)

4.2. The MRCyte Simulation Framework

In this work, also an analytical simulation framework that is capable of simulating the synergy of multiple microfluidic effects was developed. The comprehensive framework features magnetic, fluid dynamic, and biochemical processes inside the utilized microfluidic channel which act on a particle. Foremost, material parameters were stored inside the “MRCyte” class, which ranged from channel and particle properties to binding and friction constants. Basic velocity, shear, and magnetic field computations build the core of the presented program. Additionally, several dimensionless parameters such as the Stokes or Re or particle properties can be computed.

With that, simulations of the fluid dynamics that influence a single microbead as well as force-equilibrium computations for the same bead were carried out.

4.2.1. Fluid Fields inside the Microchannel

The simulation framework provided a quantitative generation of the Hagen-Poiseuille flow profile inside the microchannel with the numerical solution of Eq. 1.10. The simulated channel had dimensions ($w \times h \times l$) $700\text{ }\mu\text{m} \times 150\text{ }\mu\text{m} \times 15\,800\text{ }\mu\text{m}$. The flow rate was adopted to $80\text{ }\mu\text{L min}^{-1}$.¹ Tubing as well as time-dependent effects were neglected. The simulated \mathbf{u} for the whole channel cross-section can be observed in Fig. 18a. Due to the no-slip boundary condition, \mathbf{u} is zero on the margin while the maximum of is reached in the geometric center. \bar{u} in the channel ensues $12\,670.84\text{ }\mu\text{m s}^{-1}$.

Conjointly, computation of the flow gradient in a vertical direction and scaling with η yield the shear stress field.(Fig. 18c) As the curvature of \mathbf{u} is zero in the channel center and maximal at the edges, the shear stress reaches its largest values symmetrically at the horizontal edges of the channel.² Resulting, the net viscous shear $\tau_{\text{viscous}} = \frac{\partial u}{\partial z}$ cancels out over the whole channel cross-section.

Additionally, \mathbf{u} and τ_{viscous} acting on an $8\text{ }\mu\text{m}$ diameter bead on the channel bottom were analyzed.(Figs. 18b and 18d) In the proximity of a wall and due to the applied boundary conditions, τ_{viscous} enclosed by the bead surface is non-linear. Thus, the mean fluid velocity exposed to the bead amounts in $\bar{u}_p = 2241.59\text{ }\mu\text{m s}^{-1}$, whereas $\bar{\tau}_{\text{viscous}, p}$ strains with 4.93 dyn cm^{-2} .

¹ in accordance with the experimentally determined value

² Because the horizontal components of the gradients were neglected graceless

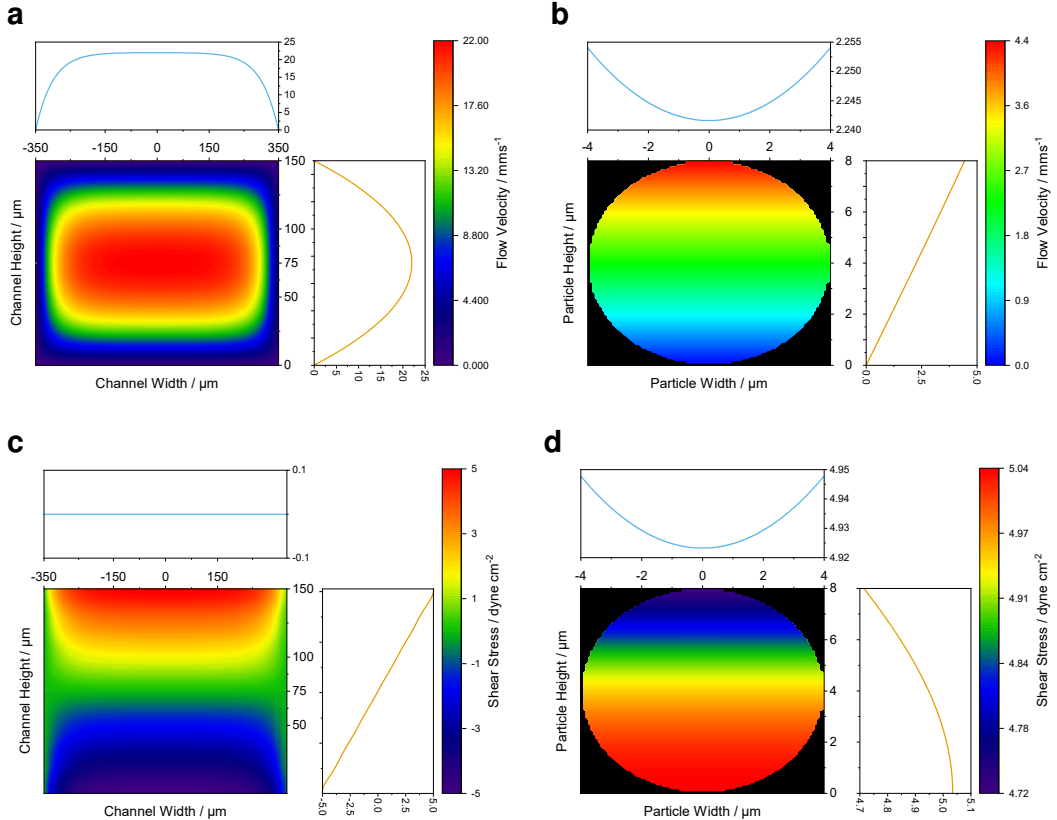


Figure 18: Flow Field and Shear Stress Simulation of the utilized Microchannel

Flow (a) and vertical shear (c) field inside the microchannel with dimensions ($w \times h \times l$) $700\text{ }\mu\text{m} \times 150\text{ }\mu\text{m} \times 15\text{ }800\text{ }\mu\text{m}$ for a flow rate of $80\text{ }\mu\text{L min}^{-1}$ and with neglected tubing effects. The subplots on the right and top sides show the mean horizontal and vertical profile in $0\text{ }\mu\text{m}$ width and $75\text{ }\mu\text{m}$ height, respectively. (vertical: —, horizontal: —)

) Due to the no-slip condition, the velocity at the walls equals zero and the shear is maximal. The maximum of the Hagen-Poiseuille profile is located in the channel center. Over the cross-section the mean flow velocity \bar{u} equals $12\text{670.83 }\mu\text{m s}^{-1}$. Resultingly, the net horizontal viscous shear $\tau_{viscous} = \frac{\partial u}{\partial z}$ cancels out over the whole channel cross-section.

Flow (d) and vertical shear (d) field acting on an $8\text{ }\mu\text{m}$ diameter bead on the channel bottom. The mean fluid velocity trapped by the bead profile results in $\bar{u}_p = 22\text{41.59 }\mu\text{m s}^{-1}$, whereas the viscous shear strains with $\tau_{viscous} = 4.93\text{ dyn cm}^{-2}$

4.2.2. Modeling the Force-Equilibrium of a Rolling Bead over a Biofunctionalized Surface

With the supplier's parameters of an 8 μm micromer-M bead (micromod Partikeltechnologie GmbH, Rostock) the corrected drag force on a bead on the bottom of the standard utilized microchannel results in 463.65 pN for 80 $\mu\text{L min}^{-1}$. This is computed from Eq. 1.13 and the correction factor in Eq. 1.18, where the simulated flow field integrated over the particle surface was plugged into.

If the bead was functionalized with biotin under the negligence of the corresponding differential equations for association constants, the number of interacting groups would result in the present surface charges. Surface charge density results in 1 $\mu\text{mol g}^{-1}$ of carboxyl and amine beads as of the supplier's data sheet. Hence, a fully saturated bead is covered with 177 500 biotin molecules.

The streptavidin coverage of the channel floor was modeled in excess over the biotin ligands and penetration depth was estimated by the size of several monolayers of protein. As described by Wu and Voldman [22], an approach of 30 nm is a reasonable quantity. In turn, the surfaces were in contact with 1.51 μm^2 which constitutes 0.75 % of the 8 μm bead surface. This reveals that 1329 biotin molecules can interact with the floor. A summation of the protein-bond force ($\mathbf{F}_{\text{protein}}$) at 5 pN to 150 pN per streptavidin-biotin bond yields the resulting adhesion force with a magnitude of 6.7 nN to 199 nN.[92]

The binding force is in the same range as the perpendicular magnetophoretic force caused by the permanent magnet under the sensor chip ($\nabla\mathbf{B} = 10 \text{ T m}^{-1}$) as well as by the nickel-iron chevron structures on the chip ($\nabla\mathbf{B} \approx 5 \text{ kT m}^{-1}$). Clearly, in the near-field approximation, the nickel-iron structures dominate \mathbf{F}_{mag} (Eq. 1.23). With the manufacturer declared saturation moment of one particle (1.12 pA m^2), the magnetic attraction force eventuates in 5.6 nN in the magnetophoresis section of the channel.

$$\mathbf{F}_{\parallel} = \mathbf{F}_{\text{drag}} - C_{\text{rr}} \cdot (\mathbf{F}_{\text{mag}} + \mathbf{F}_{\text{protein}} + \mathbf{F}_{\text{grav}} - \mathbf{F}_{\text{shear}}) \quad 2.7$$

$$C_{\text{rr}} = \sqrt{\frac{z}{d}} = \sqrt{\frac{30 \text{ nm}}{8 \mu\text{m}}} = 0.0612 \quad 2.8$$

In order to merge this analytic force balance, all remaining forces have to be projected into the direction of Stoke's drag force (F_{drag}). (Eq. 2.7) This is achieved by the introduction of a rolling resistance factor (C_{rr}) for a perfectly elastic surface. (Eq. 2.8) In a first-order approximation, the factor depends only on the approach (z) and the bead diameter (d). However, scientific literature about the rolling resistance of microbeads on microfluidic or protein-covered surfaces does not exist yet to confirm this macroscopic factor for the microscale.

Scaling all orthogonal forces to the Stoke's drag force with C_{rr} yields a net positive result (154.08 pN) for an unfunctionalized surface ($F_{\text{protein}} \stackrel{!}{=} 0$) which indicates a rolling motion in the flow direction. Notwithstanding, above a critical interaction number of 503 to 16 biotin-streptavidin bonds - for the respective release forces of 5 pN to 150 pN per linkage - the particle resists Stoke's drag force and adheres to the surface.

This behavior will be exploited in further measurements for "bead loss experiments" in order to measure a concentration difference with different degrees of biotinylated beads.

4.3. Reference Bead Surface Functionalization

After simulation of their respective coverages, biotin was titrated on 8 μm reference beads with two different surface terminations in order to selectively bind MNPs with the counter-agent streptavidin to the surface. First, amine-microbeads were modified by sulfo-NHS-biotin. Second, carboxyl beads were coated by amine-PEG₂-biotin via EDC-NHS-activation. On the same beads, Anti-IgG1-PE antibodies were titrated after the same coupling chemistry.

Subsequently, biotin-coated beads were analyzed in the flow cytometer in the by a stain with Atto-488 (Ex: 500 nm, Em: 520 nm) coupled streptavidin. The antibody was modified with phycoerythrin (PE) and measured at 488 nm excitation and 585 nm emission wavelength. The gating was standardized by the strategy found in Sec. 3.3.4, Fig. 13. Subsequently, the MFI was computed and fitted with a sigmoidal Hill-function.(Eq. 1.5) The Stability of carboxylated and aminated beads and subsequently their respective modification protocols were evaluated for 12 days.

4.3.1. Amine-Surface Biotinylation

As a first approach, polystyrene copolymer microbeads with 8 μm diameter were functionalized by (sulfo-)NHS-biotin after a standard protocol from Thermo Fisher Scientific and micromod. A titration of the biotin reactant yielded a varying surface coverage as shown in Fig. 20a. During this one-pot-reaction, the water-soluble sulfo-NHS-biotin forms an amide linkage with the primary amine and 1-hydroxy-2,5-dioxopyrrolidine-3-sulfonate splits off as a byproduct.

As can be seen from the SEM error bars from plot 20a, which were obtained from three true biological replicates, this process is highly reproducible. Therefore, surface coverage in different grades of biotinylation could be incurred accurately with an adjusted coefficient of determination (adj. R^2) of 0.981 for the resulting Hill fit.

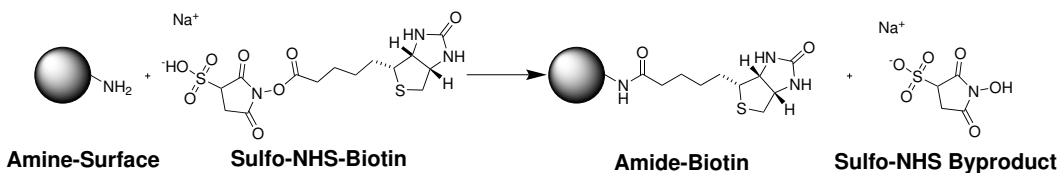


Figure 19: Amine Bead Modification with Sulfo-NHS-Biotin

An amine-terminated bead is brought into reaction with sulfo-NHS-biotin. Both form an amide linkage and bind biotin covalently to the surface. As a byproduct the sulfo-NHS-ester splits off.

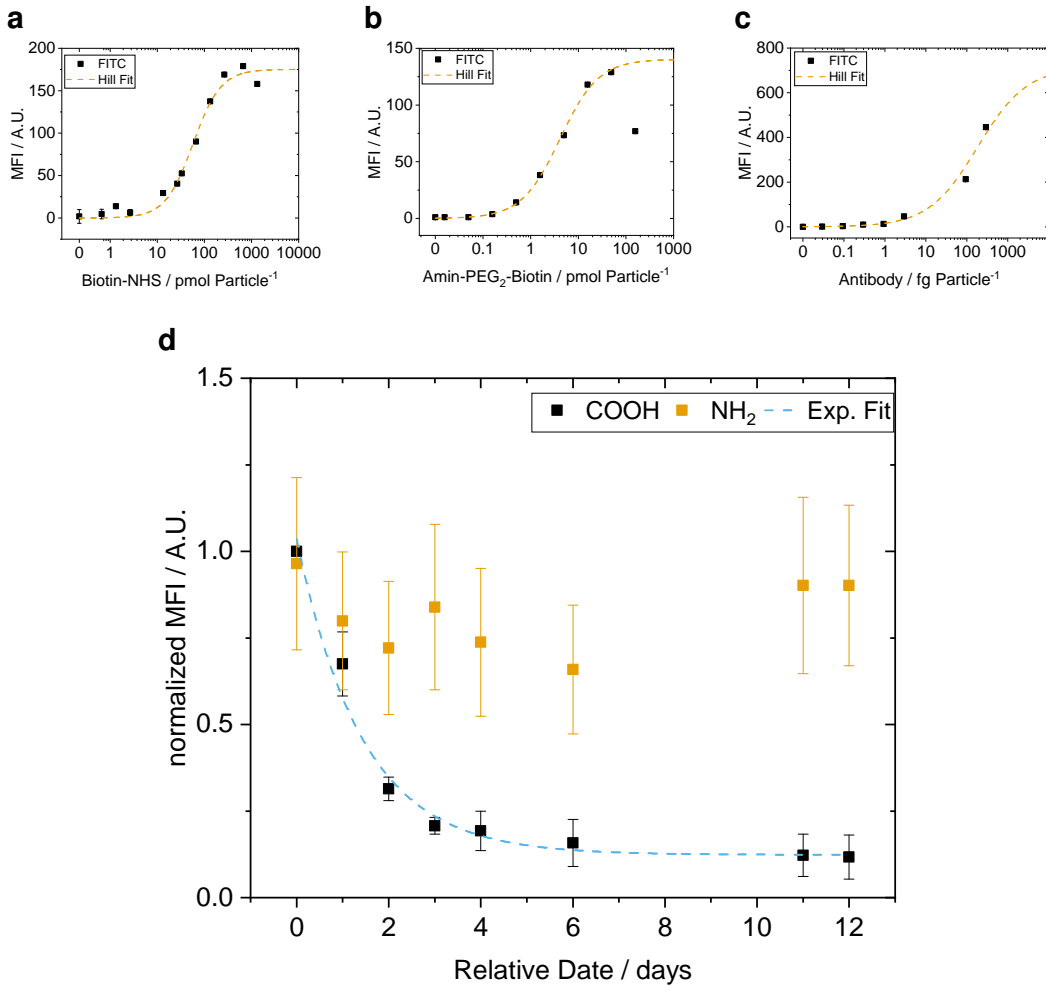


Figure 20: Titration of Biofunctional Molecules on 8 μm Particles

Titration curves of NHS-biotin (a), Amin-PEG₂-Biotin (b), and Anti-IgG1 (c) with their respective Hill fits. The corresponding fit parameters, as well as the goodness factor, are shown in Table 4a. (d) Stability analysis of functionalized carboxyl and amine beads over 12 days. The carboxylate particles show an exponential decrease with a half-life of 1.43 days as determined by the exponential fit. The respective parameters are shown in Table 4b.

a				b	
Param.	Hill 20a	Hill 20b	Hill 20c	Param.	Exp. 20d
V_{\max}	175.216 19	140.391 53	713.836 43	A	0.912 63
k	57.367 13	4.126 61	182.830 11	τ_{decay}	1.425 57
n	1.474 88	1.074 93	0.724 58	y_0	0.123 69
Adj. R^2	0.981 21	0.997 22	0.992 26	Adj. R^2	0.966 55

Table 4: Fit Parameters of Biotinylation

(a) Coefficients for the Hill fits in Figs. 20a to 20c (b) Exponential fit coefficients for the stability analysis in Fig. 20d

4.3.2. Carboxylate-Surface Functionalization

In a second approach, particles with opposite partial surface charge, mediated through carboxyl groups, have been functionalized. In turn, particles were pre-activated in EDC and NHS in MES/MEST buffer. There are two distinct reasons for the usage of MES-based buffers rather than PBS or MACS. First, EDC has its reactive maximum at pH 5 to 6. Second, buffers containing primary amines (TRIS / glycine) or carboxyls (acetate / citrate) will quench the reaction and therefore limit the efficacy.

Afterward, the beads were washed carefully and incubated with amine-PEG₂-biotin. Here, poly(oxyethylene) (PEG) indicates a hydrophilic spacer arm between both functional groups and in this case has a length of two units. The full functionalization procedure is explained in more detail in Fig. 9.

As shown in Fig. 20b, particles were functionalized equally compared to carboxamide surfaces. However, the stability of carboxyl particles yields a half-life of 1.43 days in a continuous measurement over 12 days with a subsequent exponential fit. Additionally, both procedures show an outlier at high concentrations which could not be explained during the course of this thesis.

Third, carboxylated particles have been also functionalized with the Anti-IgG1-PE antibody. Again, a Hill-shaped titration curve was achieved, but due to the costly reagent, a saturated surface coverage was not reached. (Fig. 20c)

Therefor, the fit curve has to be interpreted cautiously. Although it converged and represents the data with an adj. R^2 of 99.2 %, the goodness of fit determined by the reduced χ^2 statistic results in a value of 278.1 which indicates an underestimation of the error variance.

4.4. Concentration Measurements in MRCyte

The driving factor for the development of an absolute concentration measurement of immunomagnetically labeled cells in diluted or whole blood is that this procedure is currently not possible in today's optics-based devices due to the excess of RBCs.[104] Therefore, with the in Sec. 2.3 described deterministic approach of cell focusing for subsequent magnetic detection, absolute concentrations of magnetic reference beads were attempted to measure.

Beads with acrylate surface were pumped through a microfluidic channel with a permanent magnet underneath. The magnet drew every magnetic particle to the ground, where they were focused on the sensor bridge and subsequently measured there. From the received signal several parameters such as peak amplitudes, locations, zero-crossings, and relative distances between each other were computed.(Fig. 21) Especially for the concentration measurement a correct detection of bead signals from the noisy stream or a superposition of multiple, simultaneously measured particles was critical. The related error sources and countermeasures will be elaborated in Sec. 4.4.1.

By measuring the absolute concentration with a commercially available flow cytometer (MacsQuant 10, Miltenyi), a reference bead count was established. In a pre-test, beads were taken directly from the microcentrifuge tube, after pumping through a syringe, and after pumping through a syringe with 10 cm of connected through tubing (ID 0.5 mm, RS Chemicals). Afterward, they were counted in the flow cytometer in equal volumes. Additionally, two different buffers - MACS and PBS - and two different surface terminations were used. Both buffers are based on phosphate-buffered saline (PBS). Notwithstanding MACS contains EDTA as a chelator for divalent ions, Tween 20³, and an azide-based stabilizer. Hence, the wetting of surfaces and the electrostatic interactions of these buffers differ. The same properties were varied on the bead surface by choosing acrylate- and biotin-terminated beads.

In Fig. 22, a trend (without statistical confidence) can be observed that shows a decrease in particle counts after every additional surface with which beads could potentially interact. In term, a correct count in absolute numbers seems out of range. However, a calibration of the system with the flow profile inside the channel to compensate for losses subjected to connectors and magnetic enrichment structures was carried out successfully.

³ a non-ionic surfactant

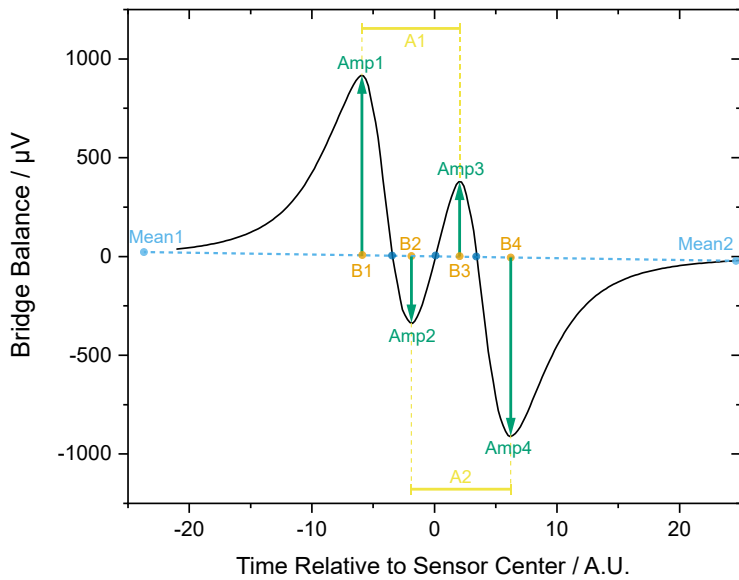


Figure 21: Example Signal of Magnetic Measurement

Signals generated from the Wheatstone bridge sensor setup feature a certain shape which allows for several measures. In case the overall signal stream carries a constant or linear offset, it is scaled to the means before and after the detected peak pattern. (Mean1, Mean2) The x- and y-positions of each peak are denominated by B1-4 and Amp1-4, respectively. The crossings of the signal through the linear connection of both means are denominated by n1-3 (in the figure by ●). Further, the difference between the equally oriented peaks B3-B1 and B4-B2 gives a measure for the homogeneous movement of the measured object and are called A1 and A2 each. From these values, the overall velocity v can be approximated because the GMR bridge distance (d_{GMR}) and sampling frequency (f_s) are fixed precisely. Analogously, the magnetic diameter of a dipole is computed by the mean of the differences B2-B1 and B4-B3.

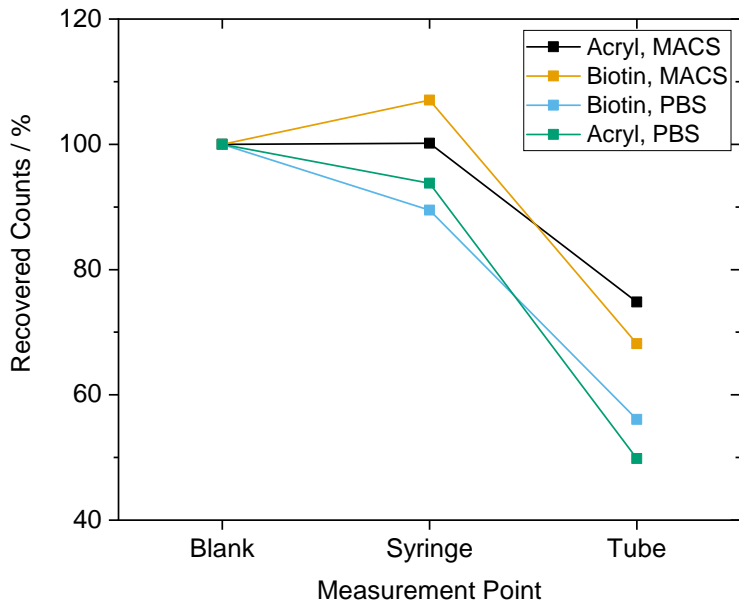


Figure 22: Bead Loss Evaluation in Connectors

Bead concentrations measured in equal volumes in the flow cytometer after being pumped through a syringe or a syringe with connected tubing. The blank sample was measured directly from the stock solution. Additionally, electrostatic and surface-tension related effects were resolved by the usage of different buffers and bead surfaces.

4.4.1. Measurement Error Sources and Calibration of Flow Field

In order to account for the bead losses due to the tubing connectors, the Hagen-Poiseuille flow profile, and magnetophoretic enrichment structures, the measured bead concentration was corrected in two different approaches.(Eq. 4.9) On the one hand, the typical assay correction to the ground truth by a constant linear fit correction factor (C_{const}) computed from the blank population was established. On the other hand, a velocity correction factor (C_{velocity}) compared the mean fluid velocity (\bar{u}) to the bead velocity (v_c).

$$c_{\text{beads, expected}} = c_{\text{beads, measured}} \cdot C \quad 4.9$$

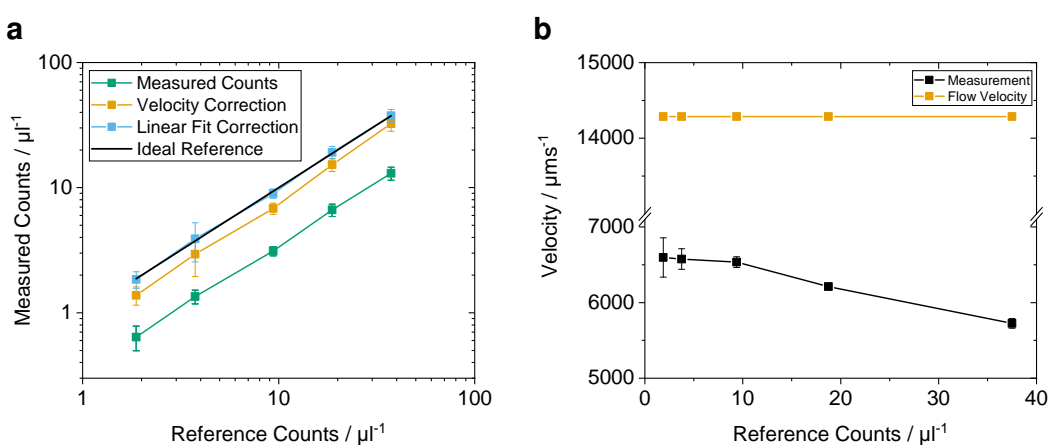
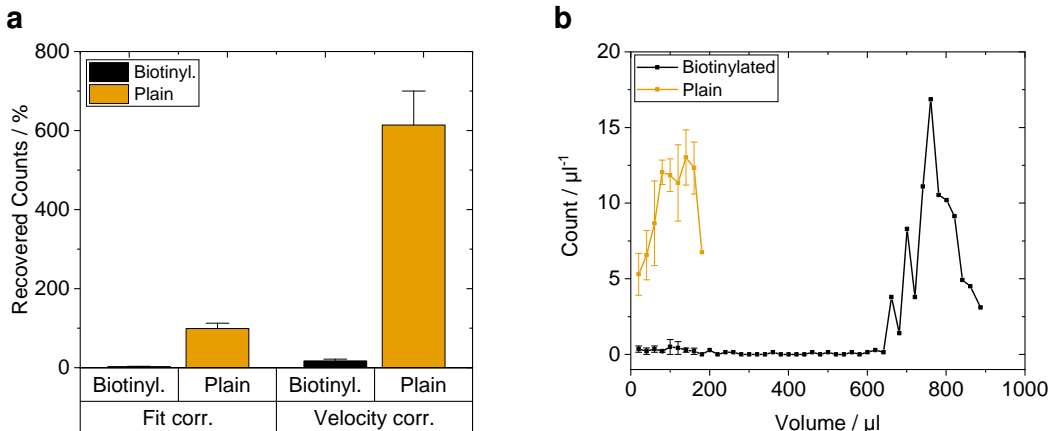
The C_{const} relates a reference count in the optical flow cytometer to the measurement in the magnetic flow cytometer.(Eq. 4.10) Equally-adjusted bead concentrations in the samples allow for a correction to the reference system. However, for an assay usage, the initial concentration of beads either has to be known precisely or has to be irrelevant, for example in regards to a standardized measurement procedure. Besides, C_{const} provides a reliable and generalizable option for correction.

$$C_{\text{const}} = \frac{c_{\text{beads, standard procedure}}}{c_{\text{beads, MRCyte}}} \quad 4.10$$

$$v_c = 2 d_{\text{gmr}} \frac{f_s}{n_3 - n_1} \quad 4.11$$

$$C_{\text{velocity}} = \frac{\bar{u}}{v_c} = \frac{Q}{A \cdot v_c} \quad 4.12$$

The C_{velocity} relates the effective particle velocity to the total fluid velocity in order to eradicate flow profile provoked effects.(Eq. 4.12) Whereas \bar{u} was determined by flow rate (Q) through a cross-sectional area (A) of the channel, v_c was analyzed from the measured signal stream. Here, the intrinsic GMR bridge distance (d_{GMR}) was divided by the time difference where the bead passed exactly over a half-bridge with known distance.(Eq. 4.11) These specific timepoints are visible as dimensionless zero-crossings n_1 and n_3 in the signal and can be converted by scaling with the sampling frequency (f_s) into the time domain.(Fig. 21)



However, if the bead velocity is not solely dependent on fluid dynamic effects - especially in the light of surface functionalizations - C_{velocity} can not be applied to experiments robustly. This is depicted in a sample experiment with a protein-covered surface in Fig. 24a. By definition, the C_{const} can not be well above 100 % whereas the count correction by C_{velocity} differs by 600 % through variations in the velocity measurement.(Fig. 23a)

An adaptation of these corrections to real measurements is depicted in Fig. 24. In a measurement where 300 μL were dispensed into the magnetic flow cytometer with a defined particle concentration, the counts were analyzed and corrected according to above. This time, the channel had a cross-section of 700 $\mu\text{m} \times 50 \mu\text{m}$ ($w \times h$) and Q was set to 30 $\mu\text{L min}^{-1}$.

Apart from a reproducible count over the dynamic range of almost two decades, both correction factors ameliorated the present data. C_{const} amounted in an optimum of 2.89 ± 0.08 while C_{velocity} centered around a mean of 2.26. Consequently, the velocity correction was misguided by 21.7 % for the advantage of requiring no *a priori* knowledge about the measurement.

Another peculiarity of C_{velocity} can be observed in Fig. 24b. While the analyzed velocity is stable for less than 10 μL^{-1} , a linear decrease is visible for higher concentrations. This is a consequence when signals of beads start overlapping if these are flowing over the sensor in close vicinity. Hence, the disturbed signal sensitizes the parameter reconstruction to errors such as false peak identification.

4.4.2. Concentration Measurement in Diluted Whole Blood

The same concentration measurements from before were now carried out in whole blood samples. Here, the reference count can be attained only below the experimentally determined critical concentration of approximately $10 \mu\text{L}^{-1}$. (Fig. 25) An insignificant discrepancy could be perceived in different volumetric blood to buffer dilutions of 1:1 and 1:20, respectively. This provides evidence for the measurement's independence from the blood concentration in a buffer.

However, a significant difference between counts was discovered between a $150 \mu\text{m}$ high channel, where C_{velocity} can be determined accurately, and a $50 \mu\text{m}$ high channel, where the correction yields a great error to the reference. This may be subjected to an increased probability of collisions from beads with blood cells and hence a decreased velocity which in turn leads to a higher correction factor. Another explanation approach could be the transition from *Newtonian* to *Non-Newtonian* fluid dynamics in smaller cross-sections, which could likewise be influenced by the Fåræus effects mentioned in Sec. 2.1.3.

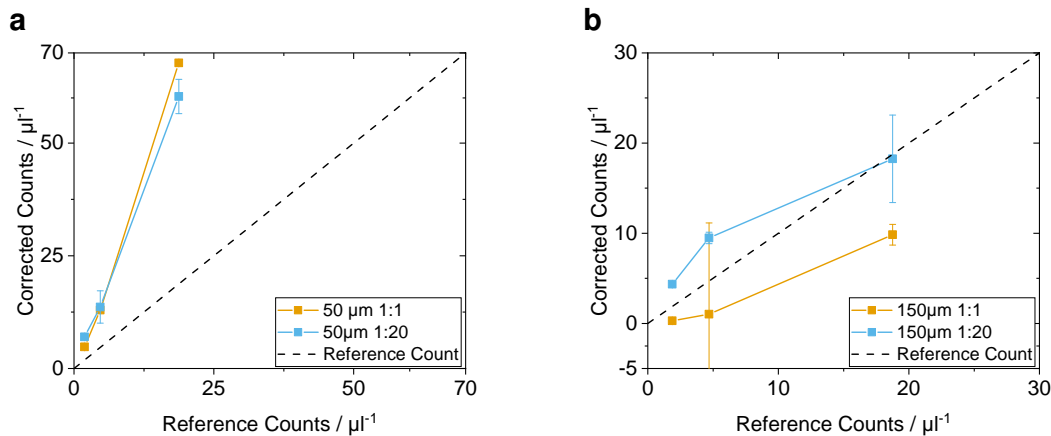


Figure 25: Absolute Concentration Measurement in Blood Samples

Velocity corrected concentration measurements for two different blood dilutions and channel heights. While C_{velocity} shows a good approximation for high channels in all tested concentrations (a), it does exaggerate the data for high concentrations at $h = 50 \mu\text{m}$. (b) This is probably a result of bead-cell collisions and the resulting path interruptions.

4.4.3. Differential Counting Setup

With regard to the necessity of correction factors, a different magnetic flow cytometer setup has been evaluated to resolve the ground truth of a concentration measurement. Here, two fully assembled sensors with PCBs were stacked on top of each other and connected in series which was expected to yield two beneficial effects.

First, one permanent magnet underneath the lower sensor chip should supply both chips with enough gradient field to pull beads to the respective channel bottom. Second, the simultaneous signal acquisition should act on the one side as a time-of-flight detector with a relatively long transport distance and on the other side, a differential concentration measurement was envisioned between both chips. Therefor, the hypothetical optimum parameter set could be reached when the relative concentration measurement yielded identity:

$$\frac{c_{\text{top sensor}}}{c_{\text{bottom sensor}}} = 1 \quad 4.13$$

The system comprises two separately assembled sensor PCBs with nylon spacers between the positional screws.(Fig. 26) A 3 mm hole was drilled into the top PCB carefully between the strip lines to minimize the tubing length from the top chip outlet to the bottom chip inlet. After the build-up of the differential counting system,⁴ the hysteresis of both sensor elements was maximized for sensitivity and the concentration was measured against a reference from the optical flow cytometer.

⁴ as described in Sec. 3.1.3

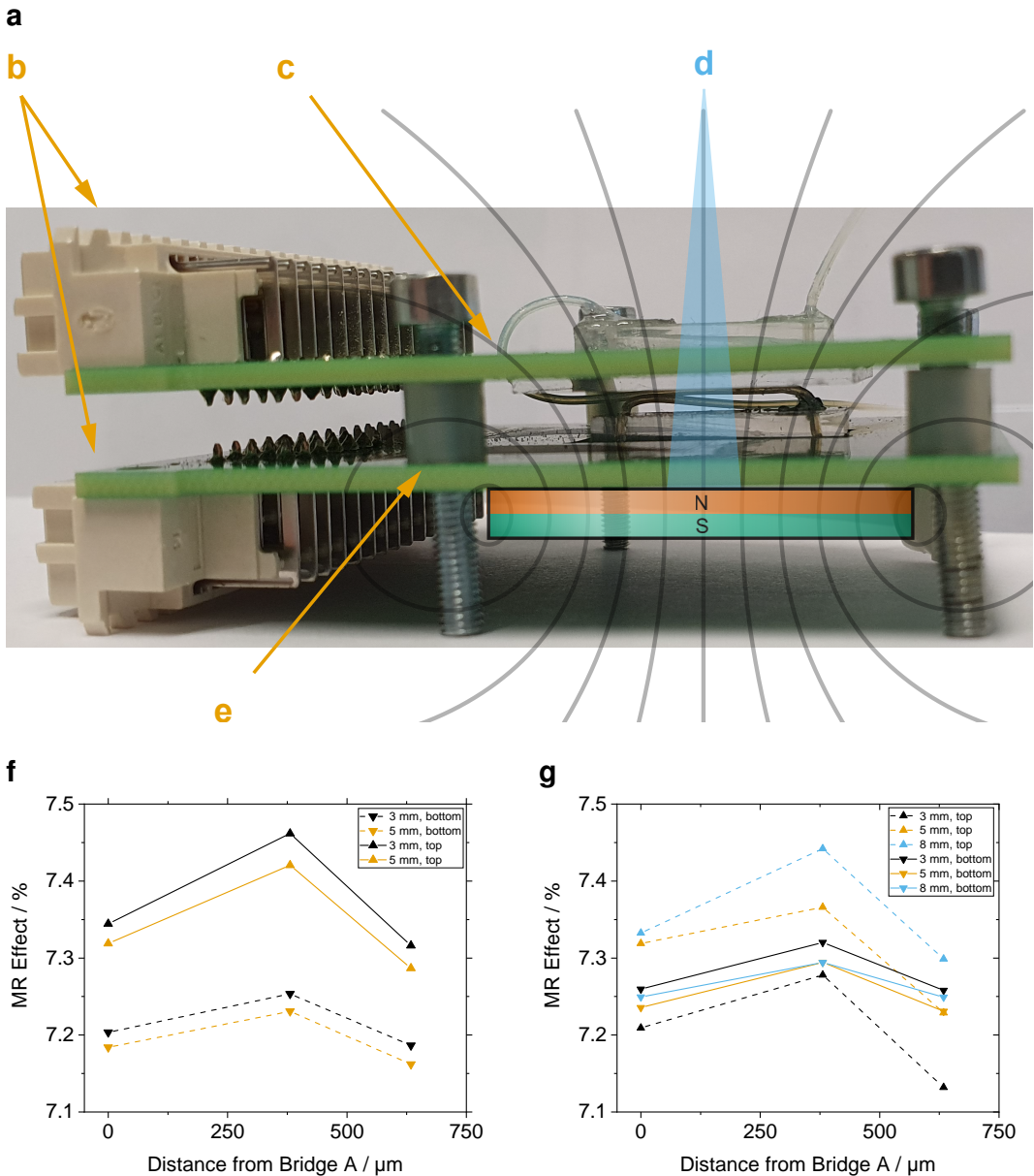


Figure 26: Hysteresis Calibration for Stacked PCB Setup

(a) Differential measurement setup: the system comprises two separately assembled sensor PCBs (**b**) with nylon spacers (**e**) between the positional screws. (**f**) A hole with a 3 mm diameter was drilled between the strip lines to connect the top chip outlet to the bottom chip inlet and minimize tubing length thereby. Schematically, a permanent magnet is placed below the bottom PCB. (**d**) The field line density respectively the area with negligibly differing field vectors are shown in the blue triangle. Because the adjustment is always carried out for a single bridge at once, this causes a systematic error.

The magneto-resistive effects of both sensors, calculated from their hystereses, are depicted for top and bottom sensors, respectively. Whereas the hysteresis was optimized for the centered sensor bridge (D or E) on the top sensor in (**f**), it was optimized for the bottom sensor in (**g**). Additionally, the height of the nylon spacers was varied from 3 mm to 8 mm but showed no statistical correlation.

Sensitivity Calibration

Initially, the permanent magnet was adjusted in three linear directions in order to maximize the magnetic sensitivity of both Wheatstone bridges. Schematically, this can be envisioned as placement of the whole top as well as the whole bottom bridge configuration into the operational range of the magnet, which is indicated by the blue triangle.

Then, the hysteresis of both outermost and one centered sensor was optimized for their full coverage and sensitivity. The recorded values for a sole optimization of the top or bottom sensor array with a height variation of the utilized nylon spacers are shown in Figs. 26b and 26c. The optimized sensor exhibits a monotonously higher MR effect than the disregarded bridge. Nevertheless, the complete sensor setup features an MR effect well above 7.2% which is acceptable both for measuring immunomagnetically labeled cells and magnetic microbeads. Furthermore, the homogeneity of the interspersing magnetic field can be monitored in the triangular shape of every acquired curve in the sensitivity plots. As the field vectors of \mathbf{B} start to disperse at the outsides of the illustrated blue area in Fig. 26c, the outer sensor regions are not located completely inside a homogeneous gradient field and get distracted by non-perpendicular field components. Helou [15]

Additionally, no influence of any spacer height could be discovered. The difference in MR effect varied insignificantly in $0.14 \pm 0.60\%$ of MR effect.

Magnetic Concentration Measurement with the Differential Sensor Setup

Due to the single utilized permanent magnet for two sensors, another field-related issue arose during concentration measurements. This requires a step back inside the general functionality of the magnetophoretic enrichment:

Any bead flowing at an arbitrary position in the microchannel experiences a negative magnetic force by the gradient of the magnetic flux density caused by the permanent magnet which pulls perpendicular to the bottom surface. Upon coming near the lower boundary, a gradient provoked by the lithographic nickel-iron structures starts to gain strength with the third power of the distance. This causes the beads to attach to the bottom firmly and enforces their rolling behavior. However, a fragile equilibrium between magnetophoresis and drag has to be maintained slightly in favor of Stoke's drag force for a continuous rolling motion.

This ideal state is a narrow space in between two boundary cases:

First, if drag force exceeds magnetophoresis, the beads will not migrate to the channel bottom in the top chip and hence result in a lower concentration measured on top. Second, if magnetophoresis outnumbers drag so that particles flow steadily in the top channel, the beads in the lower channel will stop rolling and adhere. In effect, the lower concentration measurement is compromised. This behavior is visible in Figs. 27a and 27b.

In order to find the flow rate for the optimal ratio between drag and magnetic force, measurements were performed with bead concentrations ranging from $8.5 \mu\text{L}^{-1}$ to $34 \mu\text{L}^{-1}$. The respective quotient was determined after Eq. 4.13 and plotted in Fig. 27. Below an optimal threshold of $160 \pm 10 \mu\text{L min}^{-1}$, the top sensor measures up to the 100-fold concentration of the bottom sensor. Above the threshold, the top sensor starts to miss counts which is subjected to a high drag force relative to the magnetophoresis. The quotient of both sensors shows a linearly decreasing trend towards saturation at high flow rates where no beads are measured by both sensors.

Hereby, the intersection of all measured concentrations does not reside in 1, at the optimal value of the quotient. This can on the one side be attributed to the numerical velocity correction and on the other side to the losses in the interconnection between both chips. Although the optimal quotient value would have been 1 theoretically, an ideal overlap was found for a flow rate of $150 \mu\text{L min}^{-1}$.

The determined optimal flow rate prohibits a functionalization inside the respective channel due to the high shear forces of 11.8 dyn cm^{-1} . Therefore, a bio-functionalized channel has to be designed with a greater hydrodynamic diameter to lower velocity and shear. Therefore, two channels have been designed and probed initially. First, a simple serpentine channel with a width of 1 mm has been developed to bond onto an assembled sensor.(Fig. 36a) Second, in another approach, a focusing structure with an aperture of 30 μm width for the sensor element itself has been designed.(Fig. 36b) However, the difficulties in assembly and operation of the whole setup inhibited its usage in further experiments.

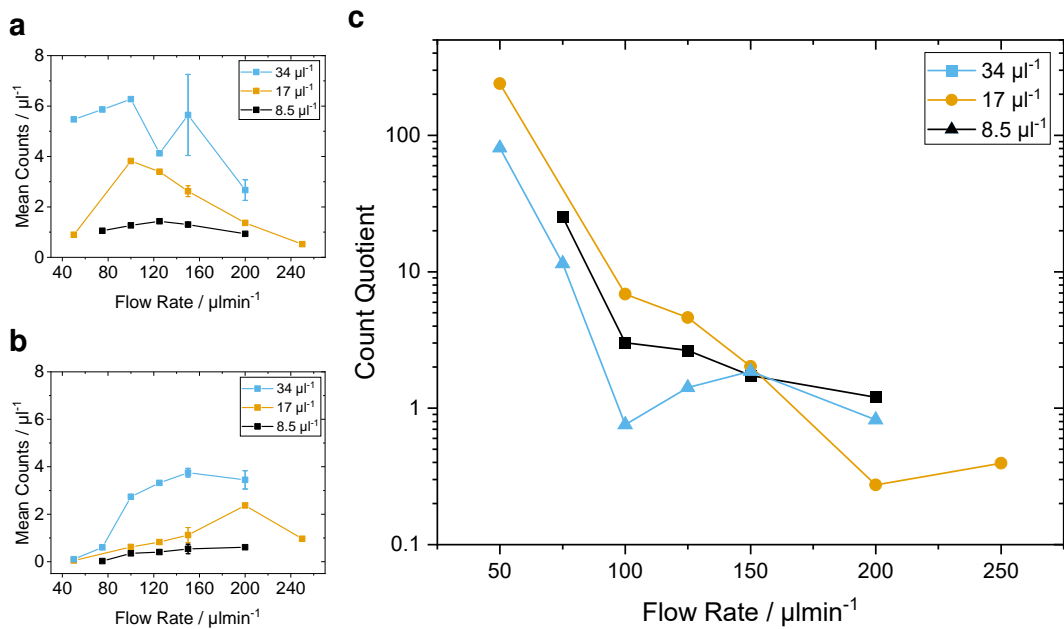


Figure 27: Optimal Differential Counting Flow Rate

The optimal flow rate for the differential setup was determined by the quotient of measured concentrations between the top (a) and bottom (b) sensor.(c) Below an optimal threshold of $150 \mu\text{L min}^{-1}$, the top sensor measures up to the 100-fold concentration of the bottom sensor. Above a threshold, the top sensor starts to miss counts which is subjected to the high drag force. (c) The quotient of both sensors $\frac{\text{top}}{\text{bottom}}$ shows a linearly decreasing trend towards a saturation at high flow rates where no beads are measured at both sensors. Hereby, the intersection of all measured concentrations does not reside in 1, at the optimal value of the quotient. This can on the one side be attributed to the velocity correction factor and on the other side to the losses in the interconnection between both chips.

4.4.4. Surface Magnetization of Biofunctionalized Beads

Here, the previously surface-modified polystyrene beads were magnetized with MNPs and counted in the magnetic flow cytometer. Originally, four different magnetic nanoparticles have been tested. Albeit, both nanomag-D-spio 100 nm (micromod Partikeltechnologie GmbH, Rostock) and dynabeads MyOne Streptavidin C1 1 µm (ThermoFisher scientific, Waltham, USA) showed inconclusive results and are omitted in the latter.

First, BNF-Dextran-redF-streptavidin 100 nm MNPs (micromod Partikeltechnologie GmbH, Rostock) were attached to the non-magnetic beads after the protocol in Sec. 3.3.4. Then, the magnetizability was examined qualitatively in a magnet stand. Particles were considered “magnetically labeled” if a pellet was visible after 10 min. Afterward, the concentrations were measured with the optical flow cytometer and adjusted to $10 \pm 1 \mu\text{L}^{-1}$ accordingly.

The subsequent measurement of 300 µL in the magnetic flow cytometer is shown in Fig. 28. In Fig. 28a the peak difference C1 (= Amp2 - Amp1, Fig. 21) is presented against the biotinylation degree. Independent experiments of 100 % and 68 % biotinylation show a certain amplitude difference. The respective fluid and particle velocities in Fig. 28b provide an explanation for this behavior. The fluid velocity had to be adapted during the course of the experiments from $80 \mu\text{L min}^{-1}$ to $10 \mu\text{L min}^{-1}$ to receive stable counts.

Keeping this in mind leads to the fact that - although only two biotinylation coverages were measured - four distinct magnetizations are represented here. Both 100 % samples show slow but plausible velocities and can therefore be correlated with differing magnetic moment. Beads with 68 % show an exceptional velocity and can hence either be considered as noisy background or very weakly magnetized particles that are not pulled to the channel bottom completely. This could also explain the decline in C1 which is also a measure for magnetic dipole moment.

Second, SV0050 50 nm streptavidin MNPs (OceanNanotech, San Diego, USA) were deposited after the equal procedure on 8 μm polystyrene beads. These experiments show the expected result of declining peak amplitude at lower biotinylation and constant velocity throughout. (Figs. 28d and 28e) At a p-value smaller than 10 %, the high populations differ significantly from each other while the log-normal fits match the histograms with a adj. R^2 of 0.94.

Two hypotheses can be drawn now from this result. On the one side, OceanNanotech MNPs could possess more magnetic moment per particle, which favors the robust measurement. On the other side, streptavidin or MNP size could influence the saturation of all available biotin sites of the particle.

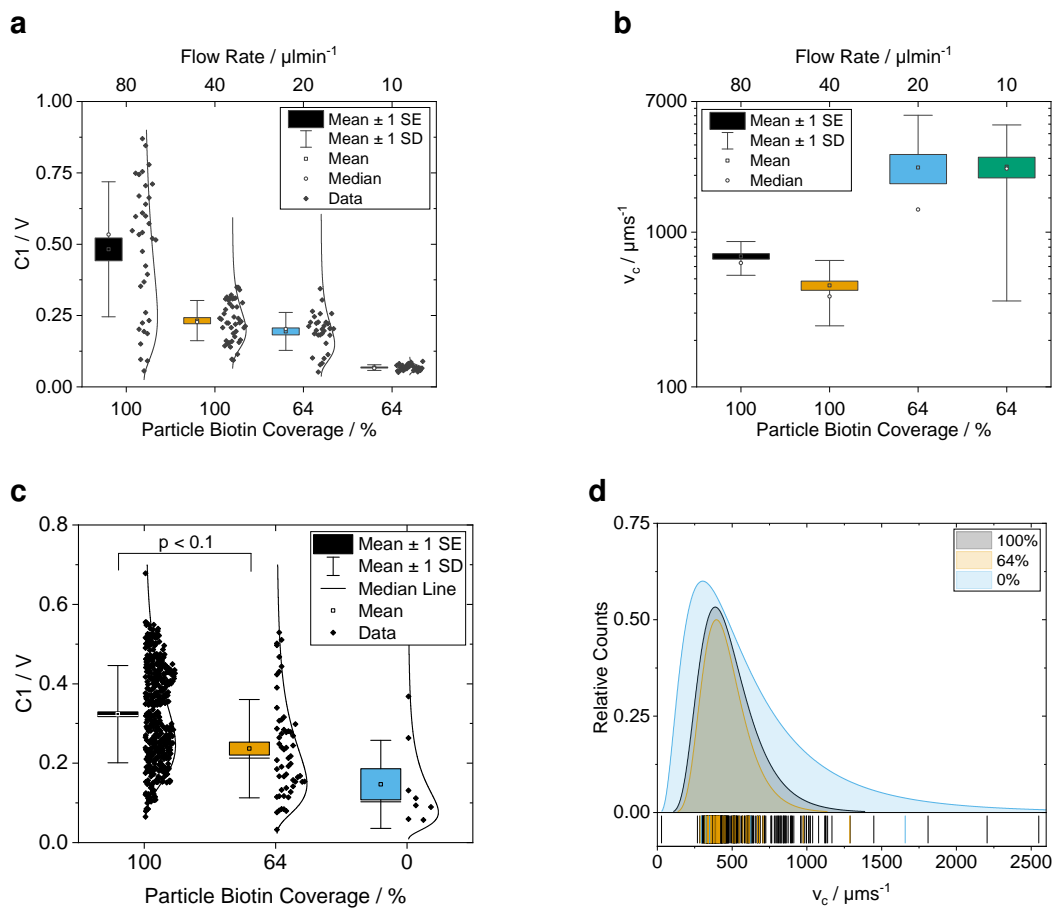


Figure 28: Bead Coverage Assay with Magnetic Streptavidin Nanoparticles

Magnetic flow cytometry data from 8 μm polystyrene sphere which were biotinylated in different degrees and subsequently coated with BNF-Dextran-redF-streptavidin 100 nm MNPs (a,b) or SV0050 50 nm streptavidin MNPs (c,d). (a) Signal amplitude of the counts with various flow rates 1. 80 $\mu\text{L min}^{-1}$ 2. 40 $\mu\text{L min}^{-1}$ 3. 20 $\mu\text{L min}^{-1}$ 4. 10 $\mu\text{L min}^{-1}$ (b) Reconstructed velocities of the respective populations. The 100 % biotinylation shows plausible velocities, whereas the 68 % sample can either be considered as noisy background or very weakly magnetized particles. (c) Signal amplitude with 80 $\mu\text{L min}^{-1}$. A correlation between biotinylation degree and magnetic moment can be assumed at a p-value $p < 0.1$ (d) Velocity distributions of the samples. As postulated, the mean velocities do not differ, moreover, are enveloped by the blank sample.

4.5. Surface Modification and Biofunctionalization of the Sensor Chip Substrate

In consideration of the problems of surface instability, analyzed in Sec. 4.4.1, and to avoid additional uncertainties in the experimental validation of the model from Sec. 4.2.2, covalent functionalizations of the sensor surface with neutravidin were carried out. First, a plate reader experiment for a qualitative statement about the shear-force stability of protein adsorption was performed. Second, different functionalization approaches with piranha and HF were tested with pure glass, PDMS, and eventually Si_3N_4 . Third, the validation of these procedures was limited to indirect measurements such as tensiometry, fluorescence microscopy, and quantitative bead capture assay, as sophisticated chemical analyses were hardly available.

4.5.1. Physisorption

In order to quantify the adsorption stability for fluorescently-labeled, physisorbed streptavidin molecules, sensor chips were cut into 10 mm^2 pieces and glued to the bottom of a 96-well plate. Subsequently, they were equilibrated with PBS and incubated with 1 mg mL^{-1} overnight. Each measurement was corrected for a blank substrate as well as the negative control with plain PBS buffer and normalized subsequently.

Every sample in the plate reader showed a significant surface decrease to a mean level of 28 % from the original fluorescence.(Fig. 29) Whereas proteins desorbed from both crystals after the first washing steps equally, Si_3N_4 outperformed Al_2O_3 as more stable in a steady state. (34.8 % vs. 27.5 %) However, no quantitative hypothesis could be formulated by these numbers due to the nature of their indirect measurement. Hence, the protein activity which is the crucial quantity for any bead rolling remains questionable. Nevertheless, a qualitative proposition is strongly confirmed that unspecifically adsorbed proteins are removed from any of both surfaces rapidly.

4.5.2. Evaluation of the Covalent Biofunctionalization with Optical Methods

Now, the results of several covalent surface modification procedures with various substrates are presented. Foremost, glass was used as the main carrier material. On glass established protocols were then brought onto PDMS and Si_3N_4 chips. As the main functionalization protocol, an activation in 7:1 piranha was carried out for 30 min.

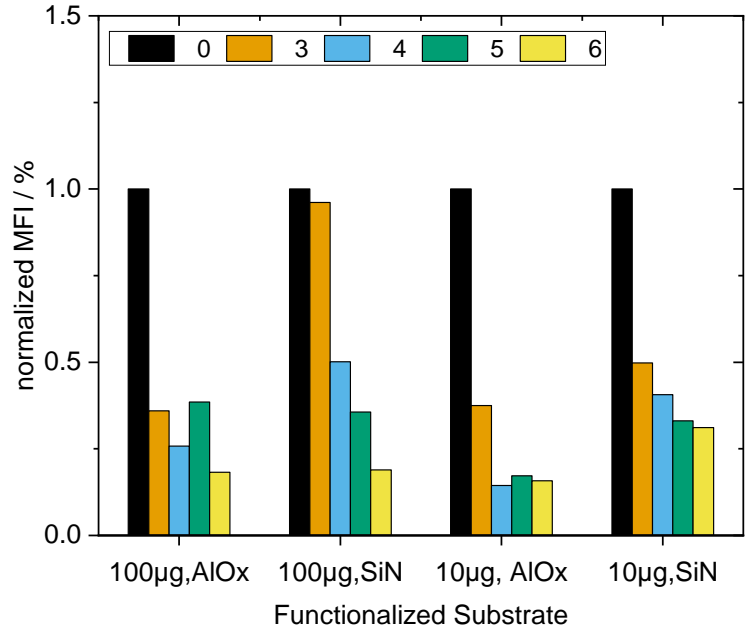


Figure 29: Surface Adsorption Stability of Neutravidin on Si_3N_4 and Aluminum oxide (Al_2O_3)

Plate reader measurement with $3 \text{ mm} \times 3 \text{ mm}$ Si_3N_4 and Al_2O_3 samples which were incubated with $100 \mu\text{g}$ and $10 \mu\text{g}$ streptavidin-atto488, respectively. The samples were subsequently washed with $200 \mu\text{L}$ PBS carefully. Fluorescence intensities were corrected with a blank substrate, the autofluorescence of PBS, and normalized eventually. Every surface reaches a mean fluorescence level of 28 % after few washing steps.

Then, the substrate was rinsed, incubated in 2% APTES solution and in PAA subsequently after the protocol described in Sec. 3.3.2. Then a $150 \mu\text{m}$ microfluidic channel was glued to the functionalized substrate and eventually filled with 1 mg mL^{-1} of neutravidin or streptavidin-atto488 if fluorescent labeling was intended. A constant flow rate of $80 \mu\text{L min}^{-1}$ was selected for the bead capture assays under the light microscope. The general process chain is depicted in Fig. 33.

As a final result, a chemical and biological functionalization could be established to a similar degree as unspecific binding. Measuring the count of beads per occupied area yields Fig. 30c. Again, two distinct states can be observed for biotinylated and plain beads at every modified surface.

The density of bound protein could also be varied through the incubation concentration and measured reliably both in an optical bead capture assay and the MFI of the channel in a fluorescence microscope.(Figs. 30d and 30e) The relative MFI indicates here the fraction supra the non-functionalized, PBS-filled microchannel.

However, a substantially different long-term stability could neither be measured nor compared to similar results accurately. Also, no proof for the covalent functionaliza-

tion could be brought with the available methods. Nevertheless, a robust and working protocol has been developed after significant literature values which encourages the position.

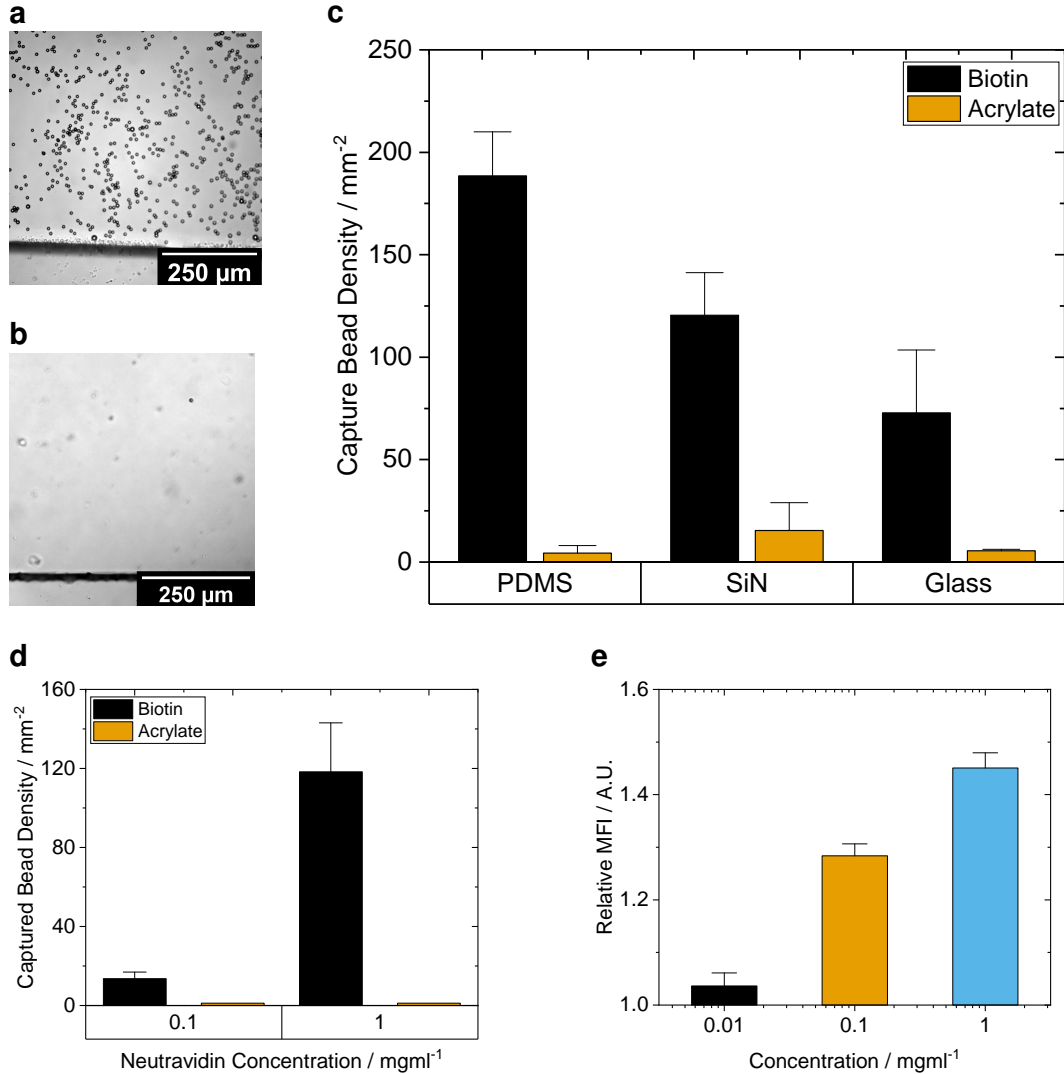


Figure 30: Optical Bead Capture Assay and Titration Fluorescence Analysis

(a, b) Microscope images from a covalently functionalized glass surface via the piranha protocol after an equal dispensed count of beads.(Sec. 3.3.1) In (a) 100 % biotinylated beads were pumped at $70 \mu\text{L min}^{-1}$, in (b) 0 % biotinylated beads were used. (c) Density measurement of captured beads on the covalently functionalized surfaces of PDMS, Si_3N_4 , and glass. PDMS shows the most promising density. (d) Titration of neutravidin on covalently functionalized glass with a subsequent analysis by a bead capture assay. (e) Titration of streptavidin-atto488 on covalently functionalized glass with subsequent fluorescence microscope imaging. The scale indicated the fraction above the fluorescence signal of a blank microchannel.

4.6. Affinity-based Concentration Measurements in the Magnetic Flow Cytometer

In this section, a sensor was unspecifically functionalized with neutravidin. Subsequently, differently biotinylated, magnetic beads were pumped over the sensor which counted the non-adhering fraction.

In order to measure the interaction properties diligently, beads were functionalized with biotin at several saturation degrees ranging from 0 % to 100 % total coverage of the available surface charges. Measurements for absolute counts as well as their time stability were carried out at $80 \mu\text{L min}^{-1}$ in a microchannel with the cross-section of $700 \mu\text{m} \times 150 \mu\text{m}$ ($w \times h$). Fig. 31a shows the absolute, linearly corrected counts determined by the magnetic flow cytometer, with a defined particle concentration of $8.9 \pm 1.1 \mu\text{L}^{-1}$.

It has been shown, that the biotinylation degree of microbeads can be measured robustly in the magnetic flow cytometer. For completely functionalized beads, the only fractions well below 1 % were counted with small SEM.(Fig. 31a, 100 %). In a result, fully-versus non-functionalized beads can be discriminated with high significance. Also, this measurement demonstrates a solid reproducibility with three different chip setups and measurement days indicated by #1, #2, and #3.

For 63.5 % biotinylated beads, a gradation of the counts can also be observed. This evidence strongly supports the possibility of an affinity-dependent, magnetic concentration measurement with the current system. However, due to the instability of the functionalization layer itself over the course of sequential measurements, additional experiments have to be conducted in order to reinforce these results.

An evaluation of the bead count distribution in the time domain shows a stable baseline for fully biotinylated beads with a recovery in the single-digit range per unit volume. In the negative control of unbiotinylated beads, also a noisy mean count of around 100 % can be observed.⁵ The unbiotinylated sample shows the previously discussed initial rise.(Sec. 4.4.1)

⁵ The shown data corresponds to the mean of three measurements from Fig. 31a

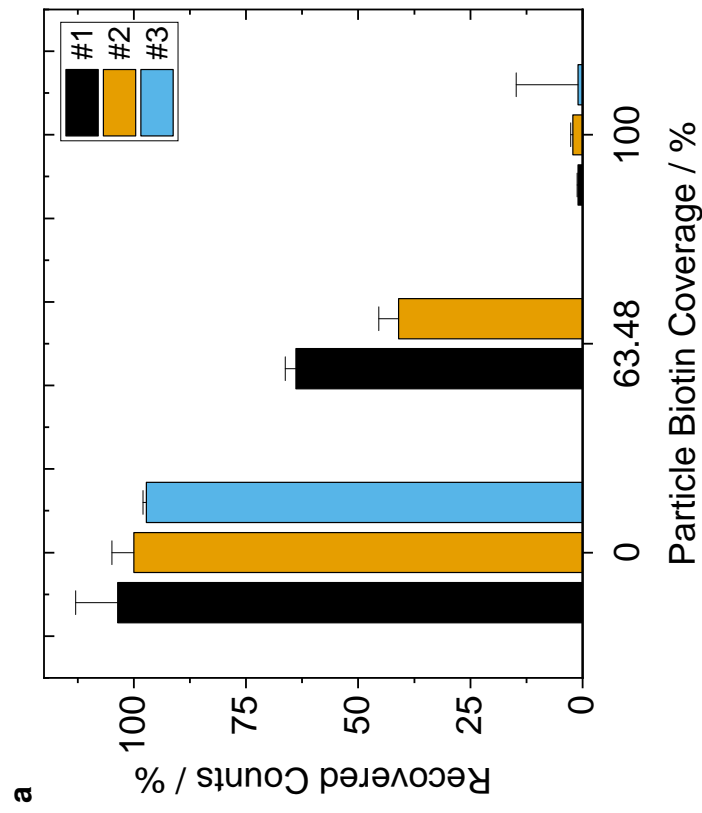


Figure 31: Concentration Measurements with Saturated Neutravidin Surfaces in the Magnetic Flow Cytometer

Biological replicates of concentration measurements with the magnetic flow cytometer. The channel surface was modified with 1 mg mL^{-1} neutravidin overnight. (a) Mean and SEM of C_{const} adjusted counts for various biotinylation degrees. (b) Time series of the mean from the three measurements on the left. Biotin-beads are captured completely, thus very few counts are detected. (—) The unbiotinylated sample shows the initial ascent due to the filling of the magnetophoretic structures. (—)

5. Conclusion

During the course of this thesis, motions of beads or cells over the GMR-sensor have been modeled from a physics and signal processing perspective. The magnetic field simulation targeted a quantitative statement about a measured cell's sensor signal for various MNP sizes. Although small particles can be deposited in great abundance on a cell surface and are expected to cause in turn a very homogeneous signal, the resulting magnetic moment is small.

In contrast, big MNPs should generate a high moment but cause field inhomogeneities at the same time. In simulations, it has been affirmed that beads generate a well-defined signal shape if the MNPs are distributed homogeneously. Thereby, the size of each MNP matters strongly. It is a severe trade-off between carrying enough magnetic moment to get a sufficient amplitude in dipole superposition and at the same time not causing inhomogeneities in the magnetic signal.

At low coverages of the cell, the signal shape differs prevalently, most for the biggest particles. Nevertheless, a broad range from 100 nm to 1000 nm diameter of the labels showed a linear magnetization behavior above 30 % of total coverage. Conclusively, the high divergence of great particles can be tolerated for cell concentration or overall detection measurements. In order to estimate morphological parameters or expression densities from the cell signal, smaller particles should be chosen predominantly.

In the force-equilibrium simulation, a model for the bead rolling motion on the bottom of a functionalized microchannel was built on basic calculus estimations. The dominant rolling forces on a microbead act in the nN range. Most dominant are magnetophoresis ($\sim 5 \text{ nN}$), Stoke's drag ($\sim 500 \text{ pN}$), and avidity ($\sim 150 \text{ pN}$, per molecule), which leads to a necessary interaction from a single to thousand proteins according to their specific release force per bond in order to cause surface adhesion. This could be subject to further refinements of the MATLAB framework with implementation of differential equations for binding kinetics [105] or the rolling motion to gain a more crisp representation of reality.

In absolute counting experiments, beads were diluted with buffer or whole blood and quantified in the magnetic setup. Empirical correction factors based on normalization and rolling velocity, to account for bead losses, were determined. To overcome these limitations, a differential counting setup was established and characterized for relative bead counting and time-of-flight applications. Optimized flow rates and magneto-resistances indicated a promising function range. However, the intrinsic bead losses and complexity of the construction faded this setup from the spotlight.

The computational findings were adopted in a method to create different surface densities of biotin or antibodies on 8 µm-beads by carbodiimide chemistry. The magnetic moment of beads could now be varied through saturation with streptavidin-MNP conjugates and measured in the magnetic flow cytometer. Due to the underlying biochemical processes in essentially all experiments, some effects remain unexplained: First, fluorescent labeling of biotinylated beads with streptavidin-atto488 yielded robust and reliable results in the bead characterization measured by an optical flow cytometer. In contrast, a similar labeling process with a recombinant secondary antibody Anti-Biotin-PE showed inexplicable, constant surface coverage and unspecific binding. This could very likely be related to a sterically blocked binding domain but remains a question to be solved.

Along with biotinylation, another effect is related to MNP coverage of bio-functionalized polystyrene microbeads. Initially, several MNPs from different suppliers (Ocean Nanotech, micromod) had shown a highly unspecific binding to the beads so that no biotinylation dependent effect was distinguishable from the background. This was confirmed by fluorescence microscopy and optical flow cytometry (Fortessa, BD Biosciences).¹ Even so, an additional measurement with newly blended PBST buffer instead of previously used PBS with biotin-free bovine serum albumin or MACS yielded compelling data. Nevertheless, the buffer exchange may not be responsible for this behavior but rather bead “age” or the optimized functionalization protocol.

¹ data not shown

For a more robust force measurement in future experiments, methods for the covalent surface modification of glass, PDMS, and Si₃N₄ have been established. These modifications were based on different wet-chemistry oxidation techniques, with subsequent silane and carbodiimide chemistry. After bio-functionalization, they were then analyzed by fluorescence microscopy or an optical bead capture assay and showed a comparable surface quality to physisorption.

In contrast, a true covalent or more precisely non-physisorbed surface modification, as well as its projected advantages in stability and definedness, could not be demonstrated during this thesis. Also, the bead rolling assay on each chemically-treated substrate has only been evaluated optically but not magnetically due to the lack of sensors on the respective substrates.

Furthermore, the desired convenience of covalent bio-functionalization could not outperform simple, unspecific physisorption. In both cases, tedious handling with low shear inside a completely bubble-free microchannel together with the watertight exchange of microtubing is necessary. For covalently modified chips, in addition, 12 h of laboratory work was required as auxiliary overhead while its superior stability was never confirmed. Therefore, it remains a supplemental procedure until an exhaustive characterization and further protocol optimization took place.

Besides, bio-functionalized surfaces have never been brought into contact with any physiological substance, such as blood or immune cells, which are very likely to disturb the system's operation.

Additionally, the existing magnetic flow cytometry platform has been extended and characterized for the use of affinity-based assays. With the help of a newly established model system for defined molecule densities on beads, their functional interaction in a microchannel led to the presented bead capture assays. For these, beads were immobilized in a laminar flow according to their respective biomolecular bond strength. To mediate their bonding to the channel bed, the microchannel was modified by physisorption of neutravidin. With these biologically augmented microfluidic systems, magnetic measurements showed a clear separation from fully- to sparsely-coated beads. Thereover, a dependency on the biotinylation-degree of microbeads has been measured with strong statistical support.

6. Outlook

The validated protocols in this thesis for bead and surface bio-functionalization present a comprehensive groundwork for further experiments regarding affinity measurements, magnetic bead or cell trapping, and exosome assays. Also, a computational and practical model for the cell receptor density has been characterized extensively and could be used for a further study of the magnetic flow cytometer or even as an internal standard in assay development.

The whole magnetic flow cytometer, nevertheless, offers some elements for potential improvements:

First, the chip design could be tailored more to the respective sensor application in order to achieve beneficial flow patterns, fewer bead losses, or the filtering of bubbles.

Second, the photo-lithographic sensor design could be improved by its sensitivity for each beads and cells. The distance between GMR-bridges could be increased for an enhanced resolution of time-of-flight and peak overlap with the compromise of a further limited, measurable concentration. Also, whereas cells require high sensitivity and low noise along with magnetic focusing, magnetic beads could be measured with a channel spanning GMR-setup to avoid the additional complexity of the magnetophoretic nickel-iron structures. Especially in the light of highly sensitive single-molecule or affinity measurements, the magneto-resistive effect could be leveraged by exploiting the tunnel-magneto-resistance instead of the giant-magneto-resistance in a new sensor layout.[106]

Third, from a time- and work-efficiency perspective, it could be profitable to develop a (real-time, automatized) data analysis software by a model-based wavelet correlation or compressive sensing. Several algorithms have already been developed [14], however, experimental verification and overall back-end integration is required.

Lastly, the bio-functionalization could be benchmarked for its attachment mechanism from chemistry and physical standpoints by field-typical methods such as dynamic-light scattering, activity assays, electron/atomic-force microscopy, or spectroscopy. This would provide deeper insights into the surface composition and hence the covalent to physisorption efficacy or model parameters for the bead rolling.

Experimentally, several pathways can now be explored. The bead rolling and its subsequent motion inside a plain channel could be related to its electrostatic surface interaction by testing for example carboxyl, amine, and biotinylated particles, as well as their intermediates. Also, a more precise velocity correction factor could be formulated.

Also, the differential counting setup should not be omitted prematurely. By removing the tubing interconnection, for instance by a through silicon via combined with a micrometer thin PDMS sheet, many losses could be lowered. Further sequential interrogation of affinity measurements can be explored over a single permanent magnet as excitation field. Moreover, the utilized high bead concentrations did probably not reflect the ultimate capabilities during a time-of-flight measurement. However, the current cost-benefit ratio for the complex technological and time-related efforts needed to create this setup constitutes to strong opposition to further development. An in-plane integration of the workflow seems to be more reasonable.

Despite the elaborated improvement options, the magnetic flow cytometry system starts to open a new field in clinical diagnostics and point-of-care testing, where a measurement is completely independent of the optical background of blood samples. With the proper integration level, tests for immune cell counts or inflammation intensities¹ could be performed bedside in minutes and effectively start saving lives shortly.

¹ measured by the cell marker density and the subsequent adhesiveness to an antibody-functionalized surface

7. Appendix

7.1. Mathematical Notation

For simplicity, any physical unit will be abstracted here by the arbitrary function $f(\xi)$.

The notation for this thesis has been defined as follows:

7.1.1. Vectorial and Scalar Units

Vector or tensor symbols are written in bold font, while normal font is used for scalar units. Forces - independently of magnitude or direction - are shown with a bold, capital \mathbf{F} . The imaginary unit is connoted as i .

Normal acting properties are multiplied with the unit outward normal (\vec{n}). The normal vector to a plane spanned by two independent vectors is calculated by the cross-product $f \otimes f$, while the scalar product is denoted by the centered dot $f \cdot f$.

7.1.2. Differential Operators

In the derivations, following after Eqs. 1.2 and 1.3, the gradient operator is symbolized by ∇f . The divergence operator of an arbitrary function f is utilized as $\nabla \cdot f$. The Laplace operator, in scalar context known as the second order derivative, is generalized here as $\nabla^2 f$ and equals $(\nabla \cdot \nabla) f$ respectively. It should be not confused with the capital delta Δ , which indicates the difference of a unit, such as $\Delta f = f_2 - f_1$. The identity matrix \mathbf{I} is indexed by its size, for example \mathbf{I}_{3x3} .

$$\sum_i f(\xi = i) = \sum_{i=0}^{\infty} f(\xi = i) \quad 1.1$$

$$\int_a^b f(\xi) d\xi = F(b) - F(a) \quad 1.2$$

$$\int f(\xi) d\xi = F(\xi) + c \quad 1.3$$

7.1.3. Integration and Summation Operators

The index of an infinite sum is shown in Eq. 1.1 and starts at 0 unless specified otherwise. If the boundaries of an integral are not shown at the top and bottom (Eq. 1.2), it is considered as indefinite integral (Eq. 1.3) with the integration constant c . However, c denotes during the course of this work - due to a lack of explicitly solved integrals - concentrations. For surfaces and volumes, the integral is repeated according to the respective dimension. In the indefinite case, the unit surface is denoted by dA , and in the volumetric case by dV .

A special focus lies on Gauss' divergence theorem which in our case converts a surface into a volume integral by the following identity:

$$\int \int \int \nabla \cdot f dV = \int \int f dA \quad 1.4$$

7.1.4. Equations and Inequalities

Approximated or estimated units are expressed by an equal sign with the assumption in overset or two tildes above each other. For sufficiency conditions, mostly inequalities were used. In these, double angular brackets, \ll or \gg , imply an value difference of at least one order of magnitude. Postulated conditions are indicated by an exclamation mark above the equal sign: $\stackrel{!}{=}$.

For non-linear graph fitting, two distinct functions have been used: The Hill-function (Eq. 1.5) and the exponential decay (Eq. 1.6).

$$y = V_{\max} \frac{x^n}{k^n + x^n} \quad 1.5$$

$$y = A e^{\frac{-x}{\tau_{\text{decay}}}} + y_0 \quad 1.6$$

7.2. Additional Figures

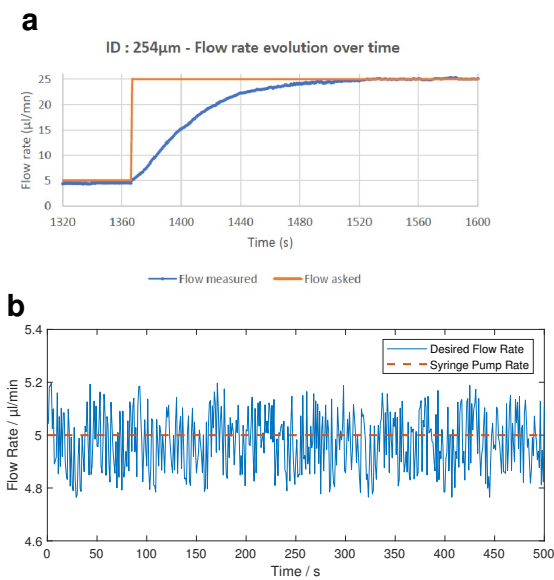


Figure 32: Syringe Pump error sources

Set flow rate: , Real Flow Rate: . The transient term of the NSE (Eq. 1.7) was neglected in all simulations. However, a connected syringe pump retains a finite rise time (**a**) and a remaining “pulsation error” in steady state (**b**). In effect, an error adds to simulation and experiment. Therefore, any measurement can only be valid several ten seconds after the last flow rate change. (**a**) Exemplary, transient step answer of a syringe pump through a microtube with 254 μm inner diameter. (**b**) Steady state flow rate error around the desired 5 $\mu\text{L min}^{-1}$ dispensing rate. A sinusoidal behavior caused by the microstepping can be observed. [107]

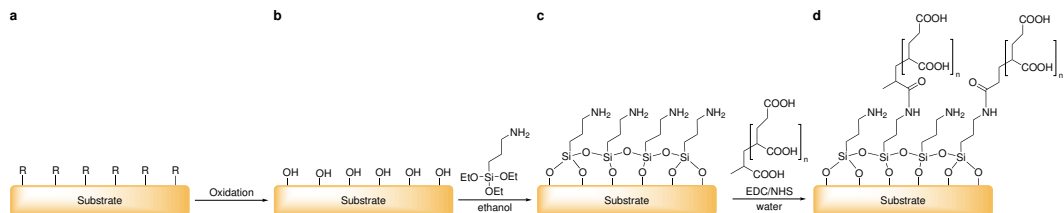


Figure 33: General process chain of chemical surface modification

Any substrate with various surface groups R (**a**) is oxidized to exhibit hydroxyl groups. (**b**). Then a silane SAM is attached (**c**) and subsequently modified by carbodiimide chemistry with PAA. (**d**)

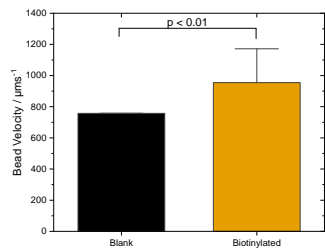


Figure 34: Measured Bead Velocity

Bead velocity (v_c) from the affinity-based concentration measurements in Sec. 4.6. The p-Value is $< 10 \times 10^{-2}$

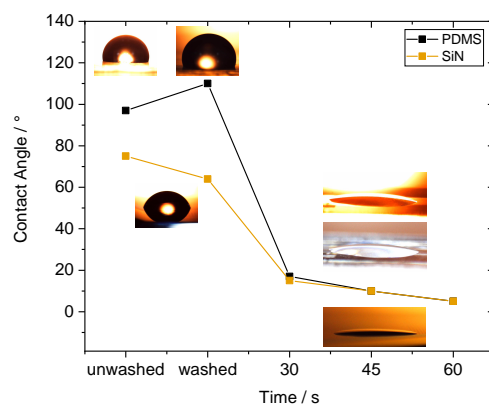


Figure 35: Hydrophobicity Analysis of PDMS under Plasma Exposure

For an optimal plasma bond to glass, Si_3N_4 and PDMS, the contact angle was measured after treatment. The initial decrease until 45 s declares the optimum around this time. Longer times should be avoided consequently to prohibit further surface damages by reactive ions.

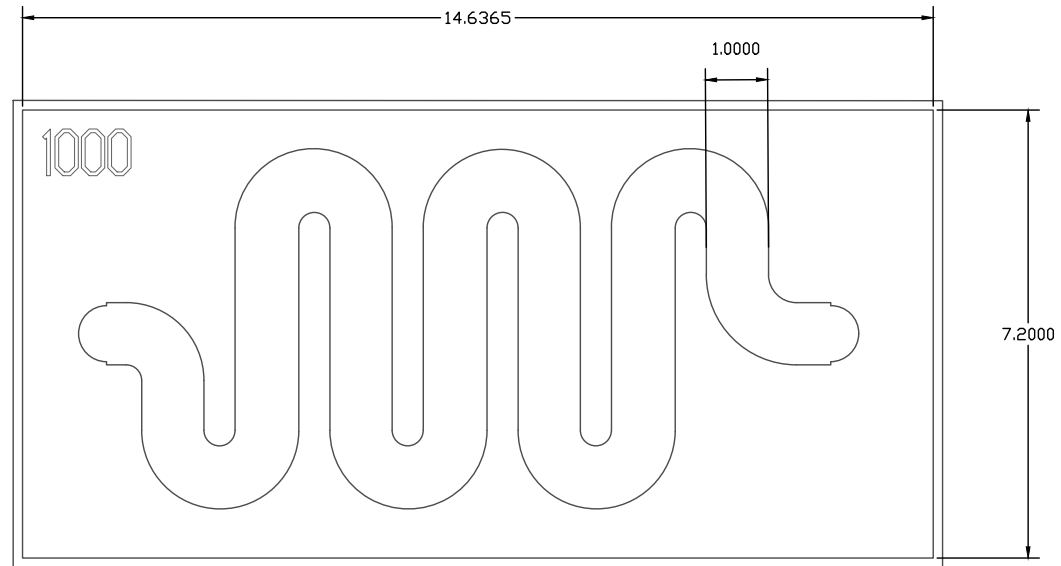
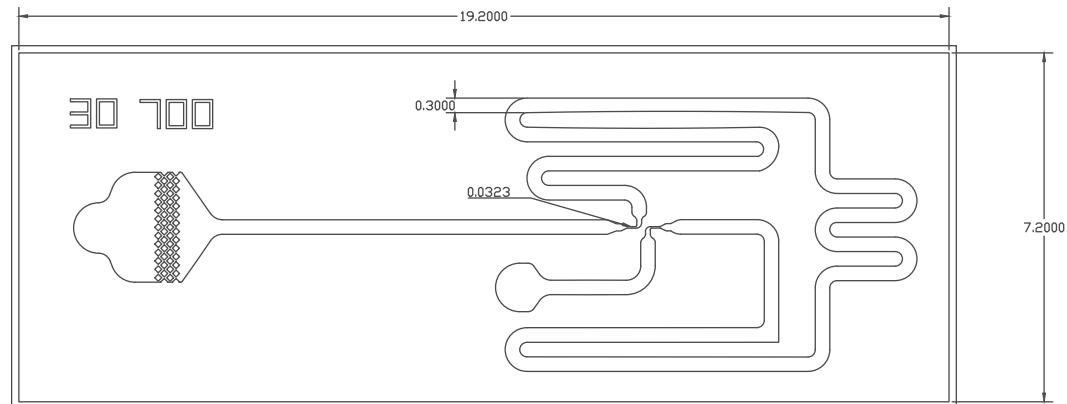
a**b**

Figure 36: AutoCAD Drawings of Microfluidic Channels
Scale: 20 mm:1 paper unit, Dimensions: mm

List of Figures

Figure 1 Schematic Force Balance on a Rolling Particle with Bio-Functionalization

The rolling motion of a microbead over the biofunctionalized surface of a microchannel is a mixture of continuum and classical mechanics. In order to identify the dominant actors and predict experiments qualitatively, an overview of all forces will be given in the theoretical background. The during the course of this thesis consistently used coordinate system was defined by e_x along the rolling direction. e_z indicates the height, whereas e_y specifies a width or depth..... 3

Figure 2 Particle Drag and Lift Behavior

(a) Bulk Drag: Force acts on a particle caused by the displacement of fluid stream lines. (b) Wall-lift Drag Force: In a special case of drag, where streamlines cannot be displaced further, a pressure gradient forms in front of the sphere. This forces a motion directed perpendicularly from the wall. (c) Shear-induced force: The curvature of the flow profile exhibits a translation and rotation due to inhomogeneously distributed shear on the surface.[30]..... 9

Figure 3 Particle Rotation Behavior

(a) Direction of rotation of a sphere settling in eccentric position between parallel walls. (b) Direction of rotation of a sphere settling in the presence of a single plane wall far from the other side.[23]..... 9

Figure 4 Magnus Effect on a Particle in Laminar Flow

The intrinsic rotation of a particle inside a laminar flow field causes a pressure gradient to the side whose tangential rotation vector is parallel to the stream lines. 12

Figure 5 Rolling Mechanics of a Sphere

Penetration model of a sphere with radius r adapted from Azad and Featherstone [41] and Waters and Guduru [42]. The top body moves into the elastic bottom body for an approach (z) and a contact area πa^2 . 15

Figure 6 Membrane Adhesion and Detachment Models	
(a) Adhesion Model after Dembo et al. [46]: Every interaction is viewed as spring-damper-model in superposition. (b) Surface Coverage Assay Model: In a stochastic approach, analyte molecules and their interactions are modeled between a planar and a spherical surface. Adapted from Wu and Voldman [22]	16
Figure 7 Different Substrate Surfaces: Glass and PDMS	
Surface groups and internal structure of quartz glass (a) and PDMS (b). After an oxidation step, surface impurities and the methyl groups are converted to hydroxyl.	19
Figure 8 Surface Oxidation and Modification by APTES	
(a) Structure of a typical trialkoxysilane, X: hydrolyzable group, R: non-hydrolyzable organic radical, n: methylene chain-length. (b) Before a condensation reaction, the oxidized surface has formed hydrogen bonds with water molecules while the silane molecules are in the bulk solution. The hydrolyzed silanol group adsorbs onto the surface and forms hydrogen bridges with the silicon-bound oxygen atom. In a condensation reaction, under the loss of water, a covalent bond to the surface forms. After the SAM assembly, the surface is saturated with a covalent-bound, crosslinked silane film.[77] (c) Proposed oxidation of Si_3N_4 with HF: Due to similar activation energies water can competitively displace HF above an effective temperature of 70 °C.....	22
Figure 9 Carboxyl bead modification with EDC/NHS	
The carboxy groups on the bead bead are activated with EDC to an active O-acylisourea intermediate. This can then either be nucleophilic attacked by a primary amine of the amine-PEG ₂ -biotin reactant or - due to its instability - hydrolyzed back to a regenerated carboxyl surface. A present NHS-ester can also displace the O-acylisourea to form a considerably more stable intermediate which then itself reacts with any primary amine.	22

Figure 10 Functional Structures of Biotin and Streptavidin

- (a) Two- and three-dimensional chemical structure of the biotin molecule.
(b) Homotetrameric streptavidin with four subunits and four bound biotin-ligands. The molecule is attached with the anchor point at one terminus to a surface.[93]..... 25

Figure 11 Overview over the MRCyte Sensor Setup

- (a) Microfluidic outlet connection to waste reservoir. (b) Imprinted channel width. (c) Microfluidic inlet connection to a syringe pump. (d) Magnetophoretic focusing region, not visible in this picture. (e) GMR-sensor region, the supply and bridge balancing traces are visible. (f) Gold bond pad: In order to connect the silicon sensor chip with the breakout PCB, wedge bonds from the chip pads to the PCB pads are forged. (g) Through-hole plating for the connection to the lock-in via jumper cables or a soldered connector plug. (h) Typical signal processing flow of a lock-in: The reference signal $V_r(t)$ is split and mixed with the input signal with a phase difference of 0° and 90° . Then, both signals are low-pass filtered and sampled by an analog-to-digital converter (ADC). (i) Accordingly, in a digital signal processing (DSP) device the input signal is digitally converted beforehand, which in turn requires a highly sensitive and fast ADC. In contrast, DSP is more accurate and allows for software-controllable technical opportunities. (j) GMR-sensor bridge circuit inside the microfluidic channel. On the left side, magnetophoretic focusing structures are visible. On the right side, four Wheatstone bridges on a compliant ground plane can be observed. 27

Figure 12 Hysteresis Calibration of the GMR-Sensor

Sensitivity Optimization of the GMR sensor via alternating hysteresis measurements and permanent magnet adjustment. (a) Optimal sensitivity is reached when the zero-crossing is centered around the zero-field and the linear section has the maximum steepness.(- - -) Upon dislocating the free layer in one direction, the magnetic field strength increases linearly towards saturation.(—) Afterward, the magnetization moves on the hysteresis loop. The total MR effect is calculated from the vertical distance between the saturation points. (—) (—) (b) In order to determine the steepness in the linear section, the hysteresis from the left side is differentiated. Actual sensitivity (- - -) is measured by the mean of all curves in the zero field. The initial magnetization curve is omitted from this measurement.(—) 34

Figure 13 Gating Strategy for Biotinylated Beads

(a), In the forward-side-scatter plot, the general bead population with high side scatter was selected from the background. (b), Single beads were differentiated by their sphericity; their ratio of height:area in the side scatter. Points on the line through the origin are spherical. (c), The stained subset in the respective color was now selected and the MFI, as well as the CV, were computed. 45

Figure 14 Particle Coverage Simulation

(a) Dimensions of the GMR Wheatstone bridge sensor: Distance d between both variable bridges (green), width w of a GMR-sensor, length L of a sensor. (b) Scheme of single-cell simulation: The ideal magnetic dipole in the geometric center of a sphere (●) causes a signal deviation from the real cell signal with magnetic moment distributed on the cell surface. (●) (c) Signal shapes of different angles of two-particle aggregates lead to differing signal shapes. 48

Figure 15 Coverage Dependent Signal Correlation

MNP coverage of a sphere with 4 μm (**a**, **b**) and 8 μm diameter (**c**, **d**) covered by magnetic particles ranging from 20 nm to 2000 nm. A cross-correlation increase which is inversely proportional to the MNP size can be observed..... 49

Figure 16 Signal Correlation between Two-Cell Aggregates At Shifting Angles

Two-Sphere aggregates are covered with 200 nm MNPs and simulated flowing over the sensor at differing respective angles. The SEM indicates a difference in the cross-correlation of three truly random MNP distributions. For low yaw angles and high coverages, the aggregate's signal reflects rather two single dipoles in superposition than one quite homogeneous dipole. This causes a high signal deviation from the reference and thus a low degree of correlation..... 53

Figure 17 Maximal Cross-Correlation Differences

(**a**) Mean coverage at 99 % for 4 μm and 8 μm spheres. A negative dependency on the MNP size can be explained by the ratio of magnetic moment per unit surface and its homogeneous distribution across the whole surface. (**b**) Relative correlation error between 4 μm and 8 μm spheres with a quadratic fit. The quadratic behavior could be related to the relative surface area which can be occupied by magnetic moment.
(Adj. $R^2 = 0.992\,09$) 53

Figure 18 Flow Field and Shear Stress Simulation of the utilized Microchannel

Flow (**a**) and vertical shear (**c**) field inside the microchannel with dimensions ($w \times h \times l$) $700\text{ }\mu\text{m} \times 150\text{ }\mu\text{m} \times 15\,800\text{ }\mu\text{m}$ for a flow rate of $80\text{ }\mu\text{L min}^{-1}$ and with neglected tubing effects. The subplots on the right and top sides show the mean horizontal and vertical profile in $0\text{ }\mu\text{m}$ width and $75\text{ }\mu\text{m}$ height, respectively. (vertical: —, horizontal: —) Due to the no-slip condition, the velocity at the walls equals zero and the shear is maximal. The maximum of the Hagen-Poiseuille profile is located in the channel center. Over the cross-section the mean flow velocity \bar{u} equals $12\,670.83\text{ }\mu\text{m s}^{-1}$. Resultingly, the net horizontal viscous shear $\tau_{viscous} = \frac{\partial u}{\partial z}$ cancels out over the whole channel cross-section. Flow (**d**) and vertical shear (**d**) field acting on an $8\text{ }\mu\text{m}$ diameter bead on the channel bottom. The mean fluid velocity trapped by the bead profile results in $\bar{u}_p = 2241.59\text{ }\mu\text{m s}^{-1}$, whereas the viscous shear strains with $\tau_{viscous} = 4.93\text{ dyn cm}^{-2}$ 55

Figure 19 Amine Bead Modification with Sulfo-NHS-Biotin

An amine-terminated bead is brought into reaction with sulfo-NHS-biotin. Both form an amide linkage and bind biotin covalently to the surface. As a byproduct the sulfo-NHS-ester splits off..... 58

Figure 20 Titration of Biofunctional Molecules on $8\text{ }\mu\text{m}$ Particles

Titration curves of NHS-biotin (**a**), Amin-PEG₂-Biotin (**b**), and Anti-IgG1 (**c**) with their respective Hill fits. The corresponding fit parameters, as well as the goodness factor, are shown in Table 4a. (**d**) Stability analysis of functionalized carboxyl and amine beads over 12 days. The carboxylate particles show an exponential decrease with a half-life of 1.43 days as determined by the exponential fit. The respective parameters are shown in Table 4b..... 59

Figure 21 Example Signal of Magnetic Measurement

Signals generated from the Wheatstone bridge sensor setup feature a certain shape which allows for several measures. In case the overall signal stream carries a constant or linear offset, it is scaled to the means before and after the detected peak pattern. ([Mean1](#), [Mean2](#)) The x- and y-positions of each peak are denominated by [B1-4](#) and [Amp1-4](#), respectively. The crossings of the signal through the linear connection of both means are denominated by [n1-3](#) (in the figure by ●). Further, the difference between the equally oriented peaks [B3-B1](#) and [B4-B2](#) gives a measure for the homogeneous movement of the measured object and are called [A1](#) and [A2](#) each. From these values, the overall velocity v can be approximated because the d_{GMR} and f_s are fixed precisely. Analogously, the magnetic diameter of a dipole is computed by the mean of the differences [B2-B1](#) and [B4-B3](#). 62

Figure 22 Bead Loss Evaluation in Connectors

Bead concentrations measured in equal volumes in the flow cytometer after being pumped through a syringe or a syringe with connected tubing. The blank sample was measured directly from the stock solution. Additionally, electrostatic and surface-tension related effects were resolved by the usage of different buffers and bead surfaces. 62

Figure 23 Error Sources in Concentration Measurements

(a) Robustness evaluation of both correction factors C_{const} and C_{velocity} for protein-coated surfaces. The mean and SEM of plain and biotinylated measurements show a high deviation from physically reasonable expectations when corrected for the velocity (right). In contrast, C_{const} can intrinsically correct only well below 100 %. (b) Mean and SEM of a fit-corrected bead capture experiment with several error sources. Initially, the magnetophoretic structures have to be filled and thus decrease the plain count for the first 100 μL . (—) Additionally, the high deviation offsets the correction factor so that the stable measurement from 100 μL to 200 μL lies now above the ideal reference. In contrast, the biotinylated beads are captured by the surface functionalization and hence a very low concentration is measured. However, a steep rise with pulsations can be observed when the surface is saturated with beads and the particles begin to flow over the sensor in bursts. (—) The abrupt decline to the end of the measured volume is most probably related to sedimentation effects inside the emptying syringe..... 64

Figure 24 Absolute Concentration Measurements

(a) Mean and standard deviation of the concentration measurement from three independent measurements. The uncorrected measurement shows a highly reproducible and linear count over the dynamic range of almost two decades. (■) The ideal reference from the flow cytometer is depicted in (—). Correction with C_{velocity} (—) yields at a factor of 2.261 09 which is 21.7 % more imprecise than C_{const} at 2.888 33 \pm 0.080 75. (b) Mean and SEM of the v_c estimation from the signal. For higher concentrations, the measured velocity becomes inaccurate thus distorts the correction factor..... 64

Figure 25 Absolute Concentration Measurement in Blood Samples

Velocity corrected concentration measurements for two different blood dilutions and channel heights. While $C_{velocity}$ shows a good approximation for high channels in all tested concentrations (a), it does exaggerate the data for high concentrations at $h = 50 \mu\text{m}$. (b) This is probably a result of bead-cell collisions and the resulting path interruptions. 66

Figure 26 Hysteresis Calibration for Stacked PCB Setup

(a) Differential measurement setup: the system comprises two separately assembled sensor PCBs (b) with nylon spacers (e) between the positional screws. (f) A hole with a 3 mm diameter was drilled between the strip lines to connect the top chip outlet to the bottom chip inlet and minimize tubing length thereby. Schematically, a permanent magnet is placed below the bottom PCB. (d) The field line density respectively the area with negligibly differing field vectors are shown in the blue triangle. Because the adjustment is always carried out for a single bridge at once, this causes a systematic error. The magneto-resistive effects of both sensors, calculated from their hystereses, are depicted for top and bottom sensors, respectively. Whereas the hysteresis was optimized for the centered sensor bridge (D or E) on the top sensor in (f), it was optimized for the bottom sensor in (g). Additionally, the height of the nylon spacers was varied from 3 mm to 8 mm but showed no statistical correlation..... 68

Figure 27 Optimal Differential Counting Flow Rate

The optimal flow rate for the differential setup was determined by the quotient of measured concentrations between the top (**a**) and bottom (**b**) sensor. (**c**) Below an optimal threshold of $150 \mu\text{L min}^{-1}$, the top sensor measures up to the 100-fold concentration of the bottom sensor. Above a threshold, the top sensor starts to miss counts which is subjected to the high drag force. (**c**) The quotient of both sensors $\frac{\text{top}}{\text{bottom}}$ shows a linearly decreasing trend towards a saturation at high flow rates where no beads are measured at both sensors. Hereby, the intersection of all measured concentrations does not reside in 1, at the optimal value of the quotient. This can on the one side be attributed to the velocity correction factor and on the other side to the losses in the interconnection between both chips..... 71

Figure 28 Bead Coverage Assay with Magnetic Streptavidin Nanoparticles

Magnetic flow cytometry data from $8 \mu\text{m}$ polystyrene sphere which were biotinylated in different degrees and subsequently coated with BNF-Dextran-redF-streptavidin 100 nm MNPs(**a,b**) or SV0050 50 nm streptavidin MNPs (**c,d**). (**a**) Signal amplitude of the counts with various flow rates 1. $80 \mu\text{L min}^{-1}$ 2. $40 \mu\text{L min}^{-1}$ 3. $20 \mu\text{L min}^{-1}$ 4. $10 \mu\text{L min}^{-1}$ (**b**) Reconstructed velocities of the respective populations. The 100 % biotinylation shows plausible velocities, whereas the 68 % sample can either be considered as noisy background or very weakly magnetized particles. (**c**) Signal amplitude with $80 \mu\text{L min}^{-1}$. A correlation between biotinylation degree and magnetic moment can be assumed at a p-value $p < 0.1$ (**d**) Velocity distributions of the samples. As postulated, the mean velocities do not differ, moreover, are enveloped by the blank sample. 73

Figure 29 Surface Adsorption Stability of Neutravidin on Si₃N₄ and Al₂O₃

Plate reader measurement with 3 mm × 3 mm Si₃N₄ and Al₂O₃ samples which were incubated with 100 µg and 10 µg streptavidin-atto488, respectively. The samples were subsequently washed with 200 µL PBS carefully. Fluorescence intensities were corrected with a blank substrate, the autofluorescence of PBS, and normalized eventually. Every surface reaches a mean fluorescence level of 28 % after few washing steps..... 75

Figure 30 Optical Bead Capture Assay and Titration Fluorescence Analysis

(a, b) Microscope images from a covalently functionalized glass surface via the piranha protocol after an equal dispensed count of beads.(Sec. 3.3.1) In (a) 100 % biotinylated beads were pumped at 70 µL min⁻¹, in (b) 0 % biotinylated beads were used. (c) Density measurement of captured beads on the covalently functionalized surfaces of PDMS, Si₃N₄, and glass. PDMS shows the most promising density. (d) Titration of neutravidin on covalently functionalized glass with a subsequent analysis by a bead capture assay. (e) Titration of streptavidin-atto488 on covalently functionalized glass with subsequent fluorescence microscope imaging. The scale indicated the fraction above the fluorescence signal of a blank microchannel..... 76

Figure 31 Concentration Measurements with Saturated Neutravidin Surfaces in the Magnetic Flow Cytometer

Biological replicates of concentration measurements with the magnetic flow cytometer. The channel surface was modified with 1 mg mL⁻¹ neutravidin overnight. (a) Mean and SEM of C_{const} adjusted counts for various biotinylation degrees. (b) Time series of the mean from the three measurements on the left. Biotin-beads are captured completely, thus very few counts are detected.(—) The unbiotinylated sample shows the initial ascent due to the in Sec. 4.4.1 discussed error which is related to the filling of the magnetophoretic structures.(—) 78

Figure 32 Syringe Pump error sources

Set flow rate: , Real Flow Rate: . The transient term of the NSE (Eq. 1.7) was neglected in all simulations. However, a connected syringe pump retains a finite rise time (**a**) and a remaining “pulsation error” in steady state (**b**). In effect, an error adds to simulation and experiment. Therefore, any measurement can only be valid several ten seconds after the last flow rate change. (**a**) Exemplary, transient step answer of a syringe pump through a microtube with 254 μm inner diameter. (**b**) Steady state flow rate error around the desired 5 $\mu\text{L min}^{-1}$ dispensing rate. A sinusoidal behavior caused by the microstepping can be observed. [107]..... 87

Figure 33 General process chain of chemical surface modification

Any substrate with various surface groups R (**a**) is oxidized to exhibit hydroxyl groups. (**b**). Then a silane SAM is attached (**c**) and subsequently modified by carbodiimide chemistry with PAA. (**d**) 87

Figure 34 Measured Bead Velocity

Bead velocity (v_c) from the affinity-based concentration measurements in Sec. 4.6. The p-Value is $< 10 \times 10^{-2}$ 88

Figure 35 Hydrophobicity Analysis of PDMS under Plasma Exposure

For an optimal plasma bond to glass, Si_3N_4 and PDMS, the contact angle was measured after treatment. The initial decrease until 45 s declares the optimum around this time. Longer times should be avoided consequently to prohibit further surface damages by reactive ions. 88

Figure 36 AutoCAD Drawings of Microfluidic Channels

Scale: 20 mm:1 paper unit, Dimensions: mm 89

List of Tables

Table 1 Wirebonding Parameters.....	29
Table 2 Properties of the used microbeads and MNPs.	43
Table 3 Magnetic Simulation Parameters	
Constants used inside the framework for the simulation of the magnetic field inside the GMR Wheatstone half-bridge. The volume magnetization was adapted according to the simulated particle size.	51
Table 4 Fit Parameters of Biotinylation	
(a) Coefficients for the Hill fits in Figs. 20a to 20c (b) Exponential fit coefficients for the stability analysis in Fig. 20d	59

Bibliography

- [1] *Bioconjugate Techniques*. Elsevier, 2013. DOI: 10.1016/c2009-0-64240-9.
- [2] Kai-Chien Chang and Daniel A. Hammer. “The Forward Rate of Binding of Surface-Tethered Reactants: Effect of Relative Motion between Two Surfaces”. In: *Bio-physical Journal* 76.3 (1999), pp. 1280–1292. ISSN: 0006-3495. DOI: 10.1016/s0006-3495(99)77291-7.
- [3] Mathias Reisbeck. “Integration und quantitative Analyse in der magnetischen Durchflusszytometrie”. Thesis. 2019.
- [4] Mathias Reisbeck et al. “Magnetic fingerprints of rolling cells for quantitative flow cytometry in whole blood”. In: *Scientific Reports* 6.1 (2016). ISSN: 2045-2322. DOI: 10.1038/srep32838.
- [5] Julian Schütt et al. “Nanocytometer for smart analysis of peripheral blood and acute myeloid leukemia: a pilot study”. In: *Nano Letters* (2020). ISSN: 1530-6984 1530-6992. DOI: 10.1021/acs.nanolett.0c02300.
- [6] Howard M Shapiro. *Practical flow cytometry*. John Wiley & Sons, 2005.
- [7] Yushan Zhang et al. “An automated bacterial concentration and recovery system for pre-enrichment required in rapid Escherichia coli detection”. In: *Scientific Reports* 8.1 (Dec. 2018). DOI: 10.1038/s41598-018-35970-8.
- [8] T. Ghonge et al. “Smartphone-imaged microfluidic biochip for measuring CD64 expression from whole blood”. In: *Analyst* 144.13 (2019), pp. 3925–3935. ISSN: 1364-5528 (Electronic) 0003-2654 (Linking). DOI: 10.1039/c9an00532c.
- [9] J. Loureiro et al. “Magnetoresistive Detection of Magnetic Beads Flowing at High Speed in Microfluidic Channels”. In: *IEEE Transactions on Magnetics* 45.10 (2009), pp. 4873–4876. ISSN: 0018-9464. DOI: 10.1109/tmag.2009.2026287.
- [10] A. E. Urusov et al. “Rapid immunoenzyme assay of aflatoxin B1 using magnetic nanoparticles”. In: *Sensors (Basel)* 14.11 (2014), pp. 21843–57. ISSN: 1424-8220 (Electronic) 1424-8220 (Linking). DOI: 10.3390/s141121843.
- [11] U. Hassan et al. “A point-of-care microfluidic biochip for quantification of CD64 expression from whole blood for sepsis stratification”. In: *Nat Commun* 8 (2017), p. 15949. ISSN: 2041-1723 (Electronic) 2041-1723 (Linking). DOI: 10.1038/ncomms15949.

- [12] Georgios Kokkinis et al. "Microfluidic platform with integrated GMR sensors for quantification of cancer cells". In: *Sensors and Actuators B: Chemical* 241 (2017), pp. 438–445. ISSN: 09254005. DOI: 10.1016/j.snb.2016.09.189.
- [13] Michael Helou et al. "Time-of-flight magnetic flow cytometry in whole blood with integrated sample preparation". In: *Lab on a Chip* 13.6 (2013), p. 1035. DOI: 10.1039/c3lc41310a.
- [14] Michael Baur. "Joint Detection and Analysis of Cells Based On Machine Learning and Compressive Sensing". Technical University Munich, 2020.
- [15] Michael Helou. "Magnetic Flow Cytometry". PhD Thesis. 2014.
- [16] Esther Räth. "Affinity-based Cell Rolling Assays in Magnetic Flow Cytometry". Thesis. 2020.
- [17] Johann Brenner. "Superparamagnetic Nanoparticles in Picoliter Droplets for Measurements with Spin Valves". Bachelor Thesis. 2018.
- [18] Brian Kirby. *Micro- and Nanoscale Fluid Mechanics*. 2010. ISBN: 9780511760723. DOI: 10.1017/cbo9780511760723.
- [19] Henrik Bruus. *Theoretical Microfluidics*. Technical University of Denmark: Oxford University Press, 2008. ISBN: 978-0-19-923508-7.
- [20] Hyungoo Lee and S. Balachandar. "Drag and lift forces on a spherical particle moving on a wall in a shear flow at finite Re". In: *Journal of Fluid Mechanics* 657 (2010), pp. 89–125. ISSN: 0022-1120. DOI: 10.1017/s0022112010001382.
- [21] Cheng Dong and Xiao X. Lei. "Biomechanics of cell rolling: shear flow, cell-surface adhesion, and cell deformability". In: *Journal of Biomechanics* 33.1 (2000), pp. 35–43. ISSN: 00219290. DOI: 10.1016/s0021-9290(99)00174-8.
- [22] Dan Wu and Joel Voldman. "An integrated model for bead-based immunoassays". In: *Biosensors and Bioelectronics* 154 (2020). ISSN: 09565663. DOI: 10.1016/j.bios.2020.112070.
- [23] D. Di Carlo et al. "Continuous inertial focusing, ordering, and separation of particles in microchannels". In: *Proceedings of the National Academy of Sciences* 104.48 (2007), pp. 18892–18897. ISSN: 0027-8424. DOI: 10.1073/pnas.0704958104.
- [24] Howard Brenner. "The slow motion of a sphere through a viscous fluid towards a plane surface". In: *Chemical Engineering Science* 16.3-4 (Dec. 1961), pp. 242–251. DOI: 10.1016/0009-2509(61)80035-3.

- [25] John Happel and Howard Brenner. *Low Reynolds number hydrodynamics*. Mechanics of fluids and transport processes. 1981. ISBN: 978-94-009-8352-6. DOI: 10.1007/978-94-009-8352-6.
- [26] Rune Barnkob et al. "Acoustic radiation- and streaming-induced microparticle velocities determined by microparticle image velocimetry in an ultrasound symmetry plane". In: *Physical Review E* 86.5 (2012). ISSN: 1539-3755. DOI: 10.1103/physreve.86.056307.
- [27] Lanying Zeng et al. "Forces on a finite-sized particle located close to a wall in a linear shear flow". In: *Physics of Fluids* 21.3 (2009), p. 033302. ISSN: 1070-6631. DOI: 10.1063/1.3082232.
- [28] Sangtae Kim and Seppo J Karrila. *Microhydrodynamics: principles and selected applications*. Courier Corporation, 2013.
- [29] Albert J. Mach and Dino Di Carlo. "Continuous scalable blood filtration device using inertial microfluidics". In: *Biotechnology and Bioengineering* 107.2 (June 2010), pp. 302–311. DOI: 10.1002/bit.22833.
- [30] Joseph M. Martel and Mehmet Toner. "Inertial Focusing in Microfluidics". In: *Annual Review of Biomedical Engineering* 16.1 (2014). PMID: 24905880, pp. 371–396. DOI: 10.1146/annurev-bioeng-121813-120704.
- [31] H. Cumhur Tekin, Matteo Cornaglia, and Martin A. M. Gijs. "Attomolar protein detection using a magnetic bead surface coverage assay". In: *Lab on a Chip* 13.6 (2013), p. 1053. ISSN: 1473-0197. DOI: 10.1039/c3lc41285g.
- [32] Jun Zhang et al. "Fundamentals and applications of inertial microfluidics: a review". In: *Lab on a Chip* 16.1 (2016), pp. 10–34. ISSN: 1473-0197. DOI: 10.1039/c5lc01159k.
- [33] Ewa Guzniczak et al. "Deformability-induced lift force in spiral microchannels for cell separation". In: *Lab on a Chip* 20.3 (2020), pp. 614–625. ISSN: 1473-0197. DOI: 10.1039/c9lc01000a.
- [34] Robin Fåhræus. "THE SUSPENSION STABILITY OF THE BLOOD". In: *Physiological Reviews* 9.2 (Apr. 1929), pp. 241–274. DOI: 10.1152/physrev.1929.9.2.241.
- [35] Robin Fåhræus and Torsten Lindqvist. "THE VISCOSITY OF THE BLOOD IN NARROW CAPILLARY TUBES". In: *American Journal of Physiology-Legacy Content* 96.3 (Mar. 1931), pp. 562–568. DOI: 10.1152/ajplegacy.1931.96.3.562.

- [36] G. Segré and A. Silberberg. “Radial Particle Displacements in Poiseuille Flow of Suspensions”. In: *Nature* 189.4760 (Jan. 1961), pp. 209–210. DOI: 10 . 1038 / 189209a0.
- [37] Rachid Chebbi. “Dynamics of blood flow: modeling of the Fåhræus–Lindqvist effect”. In: *Journal of Biological Physics* 41.3 (Feb. 2015), pp. 313–326. DOI: 10 . 1007/s10867-015-9376-1.
- [38] LANYING ZENG, S. BALACHANDAR, and PAUL FISCHER. “Wall-induced forces on a rigid sphere at finite Reynolds number”. In: *Journal of Fluid Mechanics* 536 (July 2005), pp. 1–25. DOI: 10 . 1017/s0022112005004738.
- [39] Koffi Espoir Koumi, Thibaut Chaise, and Daniel Nelias. “Rolling contact of a rigid sphere/sliding of a spherical indenter upon a viscoelastic half-space containing an ellipsoidal inhomogeneity”. In: *Journal of the Mechanics and Physics of Solids* 80 (July 2015), pp. 1–25. DOI: 10 . 1016/j.jmps.2015.04.001.
- [40] Bo Jacobson and Joost J. Kalker, eds. *Rolling Contact Phenomena*. Springer Vienna, 2000. DOI: 10 . 1007/978-3-7091-2782-7.
- [41] M. Azad and R. Featherstone. “Modeling the contact between a rolling sphere and a compliant ground plane”. In: 2010.
- [42] Julie F. Waters and Pradeep R. Guduru. “Mode-mixity-dependent adhesive contact of a sphere on a plane surface”. In: *Proceedings of the Royal Society A: Mathematical, Physical and Engineering Sciences* 466.2117 (Dec. 2009), pp. 1303–1325. DOI: 10 . 1098/rspa.2009.0461.
- [43] Gokul P. Krishnan and David T. Leighton. “Inertial lift on a moving sphere in contact with a plane wall in a shear flow”. In: *Physics of Fluids* 7.11 (1995), pp. 2538–2545. ISSN: 1070-6631. DOI: 10 . 1063/1 . 868755.
- [44] R. P. McEver and C. Zhu. “Rolling cell adhesion”. In: *Annu Rev Cell Dev Biol* 26 (2010), pp. 363–96. ISSN: 1530-8995 (Electronic) 1081-0706 (Linking). DOI: 10 . 1146/annurev.cellbio.042308.113238.
- [45] A. Coclite et al. “Predicting different adhesive regimens of circulating particles at blood capillary walls”. In: *Microfluidics and Nanofluidics* 21.11 (2017). ISSN: 1613-4982. DOI: 10 . 1007/s10404-017-2003-7.
- [46] M. Dembo et al. “The reaction-limited kinetics of membrane-to-surface adhesion and detachment”. In: *Proceedings of the Royal Society of London. Series B. Biological Sciences* 234.1274 (1997), pp. 55–83. ISSN: 0080-4649 2053-9193. DOI: 10 . 1098/rspb.1988.0038.

- [47] Pavel I. Kitov and David R. Bundle. "On the Nature of the Multivalency Effect: A Thermodynamic Model". In: *Journal of the American Chemical Society* 125.52 (2003), pp. 16271–16284. ISSN: 0002-7863. DOI: 10.1021/ja038223n.
- [48] Krishna K. Sarangapani et al. "Low Force Decelerates L-selectin Dissociation from P-selectin Glycoprotein Ligand-1 and Endoglycan*". In: *Journal of Biological Chemistry* 279.3 (2004), pp. 2291–2298. ISSN: 0021-9258. DOI: <https://doi.org/10.1074/jbc.M310396200>.
- [49] Bryan T. Marshall et al. "Direct observation of catch bonds involving cell-adhesion molecules". In: *Nature* 423.6936 (2003), pp. 190–193. ISSN: 0028-0836. DOI: 10.1038/nature01605.
- [50] Li-Chong Xu, James W. Bauer, and Christopher A. Siedlecki. "Proteins, platelets, and blood coagulation at biomaterial interfaces". In: *Colloids and Surfaces B: Biointerfaces* 124 (2014), pp. 49–68. ISSN: 0927-7765. DOI: 10.1016/j.colsurfb.2014.09.040.
- [51] S. Prentner et al. "Effects of channel surface finish on blood flow in microfluidic devices". In: *Microsystem Technologies* 16.7 (2010), pp. 1091–1096. ISSN: 0946-7076. DOI: 10.1007/s00542-009-1004-1.
- [52] Sushanta K. Mitra and Auro Ashish Saha. "Surface Modification, Methods". In: *Encyclopedia of Microfluidics and Nanofluidics*. Springer US, 2014, pp. 1–9. DOI: 10.1007/978-3-642-27758-0_1503-2.
- [53] R.A. Williams and H.W. Blanch. "Covalent immobilization of protein monolayers for biosensor applications". In: *Biosensors and Bioelectronics* 9.2 (1994), pp. 159–167. ISSN: 0956-5663. DOI: 10.1016/0956-5663(94)80108-8.
- [54] William Putzbach and Niina Ronkainen. "Immobilization Techniques in the Fabrication of Nanomaterial-Based Electrochemical Biosensors: A Review". In: *Sensors* 13.4 (2013), pp. 4811–4840. ISSN: 1424-8220. DOI: 10.3390/s130404811.
- [55] R. Funari et al. "Single Molecule Characterization of UV-Activated Antibodies on Gold by Atomic Force Microscopy". In: *Langmuir* 32.32 (2016), pp. 8084–8091. ISSN: 0743-7463. DOI: 10.1021/acs.langmuir.6b02218.
- [56] A. Ymeti et al. "Integration of microfluidics with a four-channel integrated optical Young interferometer immunosensor". In: *Biosensors and Bioelectronics* 20.7 (2005), pp. 1417–1421. ISSN: 0956-5663. DOI: <https://doi.org/10.1016/j.bios.2004.04.015>.

- [57] María-José Bañuls, Rosa Puchades, and Ángel Maquieira. “Chemical surface modifications for the development of silicon-based label-free integrated optical (IO) biosensors: A review”. In: *Analytica Chimica Acta* 777 (2013), pp. 1–16. ISSN: 0003-2670. DOI: 10.1016/j.aca.2013.01.025.
- [58] N. Lange. “Selective Chemical Modification of Silicon Nitride Surfaces for Novel Biosensor Application”. Thesis. 2017. DOI: <http://dx.doi.org/10.17169/refubium-11275>.
- [59] Marine Brunet et al. “Etching and Chemical Control of the Silicon Nitride Surface”. In: *ACS Applied Materials & Interfaces* 9.3 (2017), pp. 3075–3084. ISSN: 1944-8244. DOI: 10.1021/acsami.6b12880.
- [60] Marco E. Marques, Alexandra A. P. Mansur, and Herman S. Mansur. “Chemical functionalization of surfaces for building three-dimensional engineered biosensors”. In: *Applied Surface Science* 275 (2013), pp. 347–360. ISSN: 01694332. DOI: 10.1016/j.apsusc.2012.12.099.
- [61] M. J. Banuls et al. “Selective chemical modification of silicon nitride/silicon oxide nanostructures to develop label-free biosensors”. In: *Biosens Bioelectron* 25.6 (2010), pp. 1460–6. ISSN: 1873-4235 (Electronic) 0956-5663 (Linking). DOI: 10.1016/j.bios.2009.10.048.
- [62] Thien Dien To et al. “Modification of silicon nitride surfaces with GOPES and APTES for antibody immobilization: computational and experimental studies”. In: *Advances in Natural Sciences: Nanoscience and Nanotechnology* 6.4 (2015). ISSN: 2043-6262. DOI: 10.1088/2043-6262/6/4/045006.
- [63] K. Sekine et al. “Highly robust ultrathin silicon nitride films grown at low-temperature by microwave-excitation high-density plasma for giga scale integration”. In: *IEEE Transactions on Electron Devices* 47.7 (2000), pp. 1370–1374. ISSN: 0018-9383. DOI: 10.1109/16.848279.
- [64] M. K. Chaudhury and G. M. Whitesides. “Correlation Between Surface Free Energy and Surface Constitution”. In: *Science* 255.5049 (1992), pp. 1230–1232. ISSN: 0036-8075. DOI: 10.1126/science.255.5049.1230.
- [65] H. Hillborg et al. “Crosslinked polydimethylsiloxane exposed to oxygen plasma studied by neutron reflectometry and other surface specific techniques”. In: *Polymer* 41.18 (2000), pp. 6851–6863. ISSN: 0032-3861. DOI: [https://doi.org/10.1016/S0032-3861\(00\)00039-2](https://doi.org/10.1016/S0032-3861(00)00039-2).

- [66] A. N. Ermakov et al. "The thermodynamic characteristics of hydrogen peroxide in H₂SO₄-H₂O solutions". In: *Russian Journal of Physical Chemistry A* 80.12 (2006), pp. 1895–1901. ISSN: 0036-0244. DOI: 10.1134/s0036024406120041.
- [67] Masatomo Yashima, Yoshiaki Ando, and Yasunori Tabira. "Crystal Structure and Electron Density of α -Silicon Nitride: Experimental and Theoretical Evidence for the Covalent Bonding and Charge Transfer". In: *The Journal of Physical Chemistry B* 111.14 (2007), pp. 3609–3613. ISSN: 1520-6106. DOI: 10.1021/jp0678507.
- [68] Marine Brunet et al. "Etching and Chemical Control of the Silicon Nitride Surface". In: *ACS Applied Materials & Interfaces* 9.3 (2017), pp. 3075–3084. ISSN: 1944-8244. DOI: 10.1021/acsmami.6b12880.
- [69] Ahmed Arafat et al. "Covalent Biofunctionalization of Silicon Nitride Surfaces". In: *Langmuir* 23.11 (2007), pp. 6233–6244. ISSN: 0743-7463 1520-5827. DOI: 10.1021/la7007045.
- [70] Michel Rosso. *Modification of Silicon Nitride and Silicon Carbide Surfaces for Food and Biosensor Applications*. 2009. ISBN: 978-90-8585-379-4.
- [71] David J. Michalak et al. "Nanopatterning Si(111) surfaces as a selective surface-chemistry route". In: *Nature Materials* 9.3 (2010), pp. 266–271. ISSN: 1476-1122. DOI: 10.1038/nmat2611.
- [72] L. H. Liu et al. "Surface etching, chemical modification and characterization of silicon nitride and silicon oxide—selective functionalization of Si₃N₄ and SiO₂". In: *J Phys Condens Matter* 28.9 (2016), p. 094014. ISSN: 1361-648X (Electronic) 0953-8984 (Linking). DOI: 10.1088/0953-8984/28/9/094014.
- [73] Johan Gustavsson et al. "Surface modifications of silicon nitride for cellular biosensor applications". In: *Journal of Materials Science: Materials in Medicine* 19.4 (2008), pp. 1839–1850. ISSN: 0957-4530. DOI: 10.1007/s10856-008-3384-7.
- [74] A. Pizzi and K.L. Mittal. *Handbook of Adhesive Technology, Revised and Expanded*. Taylor and Francis, 2003. ISBN: 9780203912225.
- [75] Brian Seed. "Silanizing Glassware". In: *Current Protocols in Cell Biology* 8.1 (2000), A.3E.1–A.3E.2. ISSN: 1934-2500. DOI: 10.1002/0471143030.cba03es08.
- [76] GELEST. *Silane Coupling Agents*. Catalog. 2014.
- [77] Hossein Khanjanzadeh et al. "Application of surface chemical functionalized cellulose nanocrystals to improve the performance of UF adhesives used in wood based composites - MDF type". In: *Carbohydrate Polymers* 206 (2019), pp. 11–

20. ISSN: 0144-8617. DOI: <https://doi.org/10.1016/j.carbpol.2018.10.115>.
- [78] Walter J. Dressick et al. "Covalent Binding of Pd Catalysts to Ligating Self-Assembled Monolayer Films for Selective Electroless Metal Deposition". In: *Journal of the Electrochemical Society* 141.1 (1994), pp. 210–220. ISSN: 0013-4651. DOI: 10.1149/1.2054686.
- [79] Solange Magalhães et al. "Brief Overview on Bio-Based Adhesives and Sealants". In: *Polymers* 11.10 (2019), p. 1685. ISSN: 2073-4360. DOI: 10.3390/polym11101685.
- [80] K. C. Andree et al. "Capture of Tumor Cells on Anti-EpCAM-Functionalized Poly(acrylic acid)-Coated Surfaces". In: *ACS Appl Mater Interfaces* 8.23 (2016), pp. 14349–56. ISSN: 1944-8252 (Electronic) 1944-8244 (Linking). DOI: 10.1021/acsami.6b01241.
- [81] Robert M. Pasternack, Sandrine Rivillon Amy, and Yves J. Chabal. "Attachment of 3-(Aminopropyl)triethoxysilane on Silicon Oxide Surfaces: Dependence on Solution Temperature". In: *Langmuir* 24.22 (2008), pp. 12963–12971. ISSN: 0743-7463. DOI: 10.1021/la8024827.
- [82] Nina Bjørk Arnfinnsdottir et al. "Impact of Silanization Parameters and Antibody Immobilization Strategy on Binding Capacity of Photonic Ring Resonators". In: *Sensors* 20.11 (2020). ISSN: 1424-8220. DOI: 10.3390/s20113163.
- [83] Dean W. Sindorf and Gary E. Maciel. "Solid-state NMR studies of the reactions of silica surfaces with polyfunctional chloromethylsilanes and ethoxymethylsilanes". In: *Journal of the American Chemical Society* 105.12 (1983), pp. 3767–3776. ISSN: 0002-7863. DOI: 10.1021/ja00350a003.
- [84] D.G. Hoare and D.E. Koshland. "A Method for the Quantitative Modification and Estimation of Carboxylic Acid Groups in Proteins". In: *Journal of Biological Chemistry* 242.10 (May 1967), pp. 2447–2453. DOI: 10.1016/s0021-9258(18)95981-8.
- [85] ThermoFisher Scientific. *User Guide: NHS and Sulfo-NHS*. 2021.
- [86] D. W. Woolley and L. G. Longsworth. "Isolation of an antibiotic factor from egg white." In: *Journal of Biological Chemistry* 142 (1942), pp. 285–290.
- [87] T. Sano and C. R. Cantor. "Expression of a cloned tavidin gene in Escherichia coli." In: *Proceedings of the National Academy of Sciences* 87.1 (1990), pp. 142–146. ISSN: 0027-8424. DOI: 10.1073/pnas.87.1.142.

- [88] Claire E Chivers et al. “A streptavidin variant with slower biotin dissociation and increased mechanostability”. In: *Nature Methods* 7.5 (2010), pp. 391–393. ISSN: 1548-7091. DOI: 10.1038/nmeth.1450.
- [89] P. Weber et al. “Structural origins of high-affinity biotin binding to streptavidin”. In: *Science* 243.4887 (1989), pp. 85–88. ISSN: 0036-8075. DOI: 10.1126/science.2911722.
- [90] Bruno Miroux and John E. Walker. “Over-production of Proteins in Escherichia coli: Mutant Hosts that Allow Synthesis of some Membrane Proteins and Globular Proteins at High Levels”. In: *Journal of Molecular Biology* 260.3 (1996), pp. 289–298. ISSN: 0022-2836. DOI: 10.1006/jmbi.1996.0399.
- [91] Shuichi Miyamoto and Peter A. Kollman. “Absolute and relative binding free energy calculations of the interaction of biotin and its analogs with streptavidin using molecular dynamics/free energy perturbation approaches”. In: *Proteins: Structure, Function, and Bioinformatics* 16.3 (1993), pp. 226–245. ISSN: 0887-3585. DOI: 10.1002/prot.340160303.
- [92] H., B. Heymann, and P. Tavan. “Ligand Binding: Molecular Mechanics Calculation of the Streptavidin-Biotin Rupture Force”. In: *Science* 271.5251 (1996), pp. 997–999. ISSN: 0036-8075. DOI: 10.1126/science.271.5251.997.
- [93] Steffen M. Sedlak et al. “Streptavidin/biotin: Tethering geometry defines unbinding mechanics”. In: *Science Advances* 6.13 (2020). DOI: 10.1126/sciadv.aay5999.
- [94] Carmen-Gabriela Stefanita. *Magnetism*. Springer Berlin Heidelberg, 2012. DOI: 10.1007/978-3-642-22977-0.
- [95] Alberto P. Guimarães. *Principles of Nanomagnetism*. Springer International Publishing, 2017. DOI: 10.1007/978-3-319-59409-5.
- [96] K. H. J. Buschow and F. R. de Boer. *Physics of Magnetism and Magnetic Materials*. Springer US, 2003. DOI: 10.1007/b100503.
- [97] Hugo Dr. van den Berg. “Magnetoresistance sensor using multi-layer system - has intermediate layer between measuring layer and bias layer with perpendicular magnetisation”. DE4232244A1. May 14, 1998.
- [98] Mathias Reisbeck et al. “Magnetic fingerprints of rolling cells for quantitative flow cytometry in whole blood”. In: *Scientific Reports* 6.1 (Sept. 2016). DOI: 10.1038/srep32838.

- [99] *Principles of lock-in detection and the state of the art*. 2016. URL: <https://www.zhinst.com/others/en/resources/principles-of-lock-in-detection>.
- [100] Rojda Hicsanmaz. “Setup and Assessment of Laser Lithography for the Fabrication and Integration of Biosensor and Microfluidic Devices”. Technical University Munich, 2020.
- [101] Johannes Schindelin et al. “Fiji: an open-source platform for biological-image analysis”. In: *Nature Methods* 9.7 (2012), pp. 676–682. ISSN: 1548-7091. DOI: 10.1038/nmeth.2019.
- [102] Jean-Yves Tinevez et al. “TrackMate: An open and extensible platform for single-particle tracking”. In: *Methods* 115 (2017), pp. 80–90.
- [103] A.F. Stalder et al. “A Snake-Based Approach to Accurate Determination of Both Contact Points and Contact Angles”. In: *Colloids And Surfaces A: Physicochemical And Engineering Aspects* 286.1-3 (Sept. 2006), pp. 92–103.
- [104] Bruce Alberts et al. *Molecular Biology of the Cell*. ISBN: 0815345240.
- [105] Jan Walther Perthold and Chris Oostenbrink. “Simulation of Reversible Protein–Protein Binding and Calculation of Binding Free Energies Using Perturbed Distance Restraints”. In: *Journal of Chemical Theory and Computation* 13.11 (2017), pp. 5697–5708. ISSN: 1549-9618 1549-9626. DOI: 10.1021/acs.jctc.7b00706.
- [106] W Schepper et al. “Analysing a magnetic molecule detection system—computer simulation”. In: *Journal of Biotechnology* 112.1-2 (Aug. 2004), pp. 35–46. DOI: 10.1016/j.jbiotec.2004.04.032.
- [107] *Syringe pumps*. 2021. URL: <https://www.fluigent.com/resources/microfluidic-expertise/what-is-microfluidic/system-comparison-for-microfluidic-applications/>.

Statement

I declare that I have authored this thesis independently, that I have not used other than the declared sources / resources, and that I have explicitly marked all material which has been quoted either literally or by content from the used sources.

Munich, March 30th, 2021, Johann Alexander Brenner